1-4-2017

Design and Validation of Novel Potential High Entropy Alloys

Boliang Zhang
Louisiana State University and Agricultural and Mechanical College, bzhan13@lsu.edu

DESIGN AND VALIDATION OF NOVEL POTENTIAL HIGH ENTROPY ALLOYS

A Dissertation

Submitted to the Graduate Faculty of the
Louisiana State University and
Agricultural and Mechanical College
in partial fulfillment of the
requirements for the degree of
Doctor of Philosophy

in

The Department of Mechanical and Industrial Engineering

by
Boliang Zhang
B.S., Xi'an Jiaotong University, 2009
M.S., University of Florida, 2013
May 2018

To my loving parents

ACKNOWLEDGEMENTS

The most important person I must thank first is my major advisor, Dr. Shengmin Guo, my committee chair, major adviser and mentor, for his wisdom, caring, and support during this endeavor. He always has student's best interest in heart and help us to growth and success. The encouragement and freedoms he awarded me allowed me to build confidence in myself and independently thinking skill on research problems. His sharp mind usually helps me through obstacles and hard times. It is not possible to finish this dissertation without his guidance and endless time spending with me.

I greatly appreciate the remaining members of my committee, Dr. Guoqiang Li, Dr. Muhammad A. Wahab, and Dr. Frank T Tsai for the time and valuable advices they provided generously.

Thanks to Dr. Wenjing Meng for the countless time assisting of the TEM study, without which this work would be lacking and for which I am deeply thankful. Thanks to Dr. Gao for the AIMD simulation studies and valuable insights on the alloy design strategy.

Special thanks to Kelin Wang, for all the precious advices and encouragement during the hard times. Without those, these days could be much more tough.

Acknowledgements are also given to my colleagues, Dr. Li Wang, Dr. Jonathan Raush, Dr. Jianqing Zhao, Dr. Jiandong Liang, Dr. Zhou Wang, Dr. Yinghu Dong, Dr. Yang Mu, Dr Yi Zhang, Xiaodan Cui, Hong Yao, Congyuan Zeng, Hao Wen, and Ali Hemmasian for their assistance.

This dissertation is dedicated to my greatest parents in China for their unconditional love and unbelievable support.

TABLE OF CONTENTS

ABSTRACT

The design approach and validation of single phase senary refractory high entropy alloys (HEAs) MoNbTaTiVW and HfNbTaTiVZr were presented in first part of this dissertation. The design approach was to combine phase diagram inspection of available binary and ternary systems and Calculation of Phase Diagrams (CALPHAD) prediction. Experiments using X-ray diffraction and scanning electron microscopy techniques verified single phase microstructure in body centered cubic lattice for both alloys. The observed elemental segregation agrees well with the solidification prediction using Scheil model. The lattice constant, density and microhardness were measured to be 0.3216 nm, 4.954 GPa and 11.70 g/cm^3 for MoNbTaTiVW and 0.334 nm, 5.5 GPa and 9.36 g/cm^3 for HfNbTaTiVZr.

To elaborate the single-phase stability of HEAs, Cr_xMoNbTaVW was examined over a certain range of Cr content in the second part of this dissertation. The change in composition led to different BCC structures with different microstructures and physical properties. Microstructure characterizations were performed using X-ray diffraction and scanning electron microscopy. Chemical micro-segregation during solidification predicted using the Scheil model generally agrees with the experimental results. The lattice constant, density, and Vickers' micro-hardness of the high-entropy alloy samples in the as-cast state are measured and discussed. For CrxMoNbTaVW, x=2.0 case appears exceeding the upper limit of maintaining a single BCC phase HEA, determined by the XRD patterns. The elemental dependence of the mixing thermodynamic properties (entropy, enthalpy and Gibbs energy) in BCC phase in the senary system is analyzed. The calculated entropy of mixing and enthalpy of mixing for CrMoNbTaVW are 14.7 J/K/mol and −662.5 J/mol respectively.

Phase predictions and characterizations on as-solidified septenary refractory high-entropy alloy, CrMoNbReTaVW, are presented in the third part of the dissertation. The simulated solidification process predicts a single body-centered-cubic (BCC) crystal structure with the tendency of compositional segregation. X-ray diffraction results confirm the "single-phase-like" BCC structure, while further experimental characterizations reveal the existence of multiple grains with significantly different compositions yet the same crystal structure and similar lattice.

For better understanding of corrosion properties of high entropy alloys, the CALPHAD method was further used to simulate the Pourbaix diagram and the corrosion layer evolutions under equilibrium conditions for CoCrFeNi based HEAs in the last part of the dissertation. The oxidation layer pitting and forming potential were calculated and compared favorably with published experimental results on CoCrFeNi, CoCrFeNiCu and $CoCrFeNiAl_{0.5}$ HEAs.

CHAPTER 1. INTRODUCTION

1.1. High-entropy alloys

High-entropy alloys (HEAs) consist of five or more principal metallic elements, with atomic percentage of each element varying between 5% and 35%. In contrast, conventional alloys consist of one or two major elements, together with other minor alloying components. The properties of multi-principal metallic element HEAs are much different from conventional alloys, in which intermetallic compounds are commonly found. HEAs may have a simple body-centered cubic (BCC) crystal structure, a face-centered cubic (FCC) crystal structure, a hexagonal close packed (HCP) crystal structure, or a mixture of those crystal structures. HEAs are also different from multi-principal element metallic glasses, where only random and non-crystal structures are available due to their low mixing entropy. Although HEAs are a relatively new group of alloys, HEAs continue to stimulate fundamental studies due to their unique compositional complexities and associated great potential for new scientific discoveries and for a wide range of functional and structural applications, owing to their excellent low temperature ductility [1], machinability, hardness flexibility, wear resistance, high temperature strength and shock resistance, and corrosion and oxidation resistance. An increasing amount of research on HEA has been conducted in recent years [2-7]. The major benefits of HEAs include that: (1) Lowering the Gibbs free energy of the solid solution phase reduces the chemical driving force towards degradation in harsh environment; (2) Reducing the atomic diffusivities slows down the reaction rate towards diffusion-controlled phase transformations; (3) Materials strength can be tailored by using solid solution strengthening mechanism. Therefore, developing novel and high-performance HEAs is a great basic academic research topic, with industrial application importance.

1.2. Searching strategy

Since the birth of the new alloying concept of high-entropy alloys (HEAs) [8, 9], there has been one noticeable challenge in the HEA community: there has been very limited number of single-phase HEAs reported as summarized in [10], and there are even fewer compositions with more than 5 principal elements [11]. In a recent article by AFRL researchers, Dr. Miracle *et al*.[12] estimated that there are 500,000 equimolar HEAs when the compound-forming elements Al and Si were added for medium (<450 ºC) and high (> 1100 ºC) temperature applications.

Because of the large number of HEA possibilities, a computational approach is needed to speed up the process of identifying single-phase HEAs to meet unique requirements. Most commonly, the CALPHAD (CALculation of PHAse Diagrams) is used to calculate the equilibrium phases at high temperature for HEA design and selection. Olson *et al*. has demonstrated how to use CALPHAD database and associated software system for alloy designs [13-19]. CALPHAD is a framework providing fundamental phase-level thermochemical and physical properties spanning solution thermodynamics, molar volumes, atomic mobility, and elastic constants. Recently, Gao and Alman have proposed an efficient methodology in identifying new HEA compositions, namely combining first-principles calculations, CALPHAD modeling, and experimentation [10]. In particular it is mentioned [10] that formation of isomorphous solid solution in edge binary and ternary systems will likely lead to HEA formation in higher-order systems. In the CALPHAD framework for HEAs, self-consistent Gibbs free energy for descriptions of all binary and ternaries are critically needed, while higher-order interaction parameters could be ignored due to the lack of experimental data and because their impact is substantially smaller than those for lower-order ones. In other words, thermodynamic description for a HEA system can be extrapolated from the available binary and ternary descriptions. The thermodynamic calculations can be performed to

understand the effects of each element on the phase stability, the microstructure variation with the composition change in regard to the stable phases, the amount of each phase, phase compositions, and so on. Such calculations could therefore be used to identify HEA compositions with desired properties. Following this approach, I examined the formation mechanisms of three senary refractory HEAs in the body-centered cubic (BCC) structure and one quaternary HEAs of hexagonal close-packed (HCP) structure. I demonstrated the good agreement in micro-segregation between CALPHAD modeling and experiments [11].

1.3. Objective and scope of dissertation

The objective of this dissertation is to develop new high entropy alloys by using numerical prediction and experimental validation method. Also, it is intended to explore the potential properties of the HEAs in mechanical behavior, corrosion resistance and electromagnetic shielding effect.

In this dissertation, the HEA design method and the validation experimental procedures are introduced in Chapter 2. In Chapter 3, the modeling and experimental validation results on a senary HEA, MoNbTaTiVW, are presented. The composition is identified via the procedure described in my early publication [10], and the microstructure and the mechanical properties are characterized to confirm the design. Chapter 4 continues the prior work [11] in searching for new BCC HEAs with more than 5 principal components. The HfNbTaTiVZr alloy was designed by inspecting the experimental binary and ternary phase diagrams and using CALPHAD method. V, Nb and Ta have only one stable structure in the BCC lattice, while Ti, Zr and Hf have a hexagonal-close-packed (HCP) structure at lower temperature and a BCC structure at high temperatures [20]. Formation of single-phase BCC HfNbTaTiZr HEA was reported by Senkov et al. [21], but addition of V to it appears to be counterintuitive since C15 Laves phase is very stable in Hf-V, Ta-V and V-Zr

binaries [20]. In addition, very recent theoretical study by Widom using first-principles density functional theory (DFT) methods predicted that the C15 NbV_2 Lave phase was stable at lower temperatures in the Nb-V system [20]. In Chapter 5, I demonstrated that senary refractory high-entropy alloys $Cr_xMoNbTaVW$ (x = 0.5, 1, and 2 in molar ratio) can be tailored over a certain range of Cr contents to form BCC phase HEAs with different microstructures and physical properties. The phase stability of $Cr_xMoNbTaVW$ HEAs was first evaluated using the CALPHAD method. Then experimental effort was applied to validate the phase structures, the microstructures, and the influence of Cr content. Formation of single BCC phase MoNbTaVW HEA has been reported by Senkov et al. [22] who identified all peaks on the X-ray diffraction (XRD) patterns of MoNbTaVW in the as-cast condition to be a single BCC phase, despite the presence of elemental segregation associated with the dendritic microstructure. However, proper homogenization and subsequent annealing (or thermo-mechanical processing) are required to achieve chemical homogeneity and thus to further improve mechanical and other properties. The objective of Chapter 5 is to examine the single phase high entropy alloy formation range with different Cr content and the corresponding elemental segregation and phase separation behavior. In Chapter 6, the single phase concept in refractory high entropy alloy system, especially the systems in which the elemental segregation exist, was further evaluated. By using both XRD and SAD/TEM, the segregation regions were confirmed to be different types of grains. Although the crystalline structures are both belong to BCC structure, and the lattice constant is extremely close, the constitutions of both lattice are totally different, and the mechanical properties of these two types of grains have discernable difference. Chapter 7 aimed at development of aqueous corrosion model of high entropy alloy system by using CALPHAD method, in order to predict and study the complex oxidation passivation film behavior of the HEAs during corrosion. By comparing with

the experimental potentioldynamic polarization test results, the passive region as well as the pitting potentials were identified.

CHAPTER 2. HEA DESIGN AND EXPERIMENTAL VALIDATION METHODS

2.1. CALPHAD method

2.1.1. Basics of CALPHAD theory

CALPHAD stands for CALculation of PHAse Diagrams, which aimed at coupling phase diagrams with thermochemistry by computational techniques. This method is based on the theory of deriving the thermodynamic functions of a system from previous experimental databases. The parametric thermodynamic models of Gibbs free energy functions are expressed as polynomials of temperature and chemical composition. The parameter values of the polynomial are obtained by optimizing the available experimental data.

The Gibbs energy of a phase is described by a model that includes experimentally optimized variable coefficients, e.g. melting and transformation temperatures, solubility, as well as thermodynamic properties such as heat capacities, enthalpies of formation, and chemical potentials.

The following model is most commonly used to estimate the Gibbs energy at a specific temperature:

$$G_o(T) - \sum x_i H_i^{SER}(T_0) = a + bT + CT\ln T + \sum_n d_n T^n \quad (2.1)$$

where $G_o(T)$ is the Gibbs energy relative to a standard element reference state (SER), H_i^{SER} is the enthalpy of the element *i* in its stable state at the temperature reference temperature and pressure, and a,b,c and d_n are the model parameters. For multi-component solution phases, the following expression for the Gibbs energy is used:

$$G = G_o + G_{mix}^{ideal} + \Delta G \tag{2.2}$$

where G_o is the Gibbs free energy relative to a standard element reference state, G_{mix}^{ideal} is the ideal mixing contribution, and ΔG is the excess Gibbs energy of mixing (the non-ideal mixing contribution).

For a binary single sub-lattice model, the Gibbs free energy can be calculated by using the following equation:

$$\Delta G_{AB} = x_A x_B \sum_{i=0}^{j} L_{AB,i}(x_A - x_B)^i \tag{2.3}$$

where $L_{AB,i}$ is a *i*th order binary interaction parameter between species A and B, and x_A, x_B is the mole fraction of species A and B. By using this model, the Gibbs free energy tenary system can be also extrapolated as equation:

$$\Delta G_{ABC} = x_A x_B \sum_{i=0}^{j} L_{AB,i}(x_A - x_B)^i + x_B x_C \sum_{i=0}^{j} L_{BC,i}(x_B - x_C)^i + x_C x_A \sum_{i=0}^{j} L_{CA,i}(x_C - x_A)^i \tag{2.4}$$

while if the experimental data is available for the tenary system, the "true tenary's" Gibbs free energy can be calculated only by the 0^{th} and 1^{st} order of the interaction:

$$\Delta G_{ABC} = x_A x_B x_C \begin{bmatrix} L_{ABC,0} + \frac{1}{3}(1 + 2x_A - x_B - x_C)L_{ABC,1} \\ + \frac{1}{3}(1 + 2x_B - x_C - x_A)L_{BCA,1} \\ + \frac{1}{3}(1 + 2x_C - x_A - x_B)L_{CAB,1} \end{bmatrix} \tag{2.5}$$

By similar method, a higher alloy system can be also calculated if all the edge binary interactions are available. That gives us the basic tools to do the HEA prediction which usually

contains more than 5 elements. It should be noted more experimental data of "true tenary" system will give us a more reliable assumption.

2.1.2. Using CALPHAD on alloy design

Alloy design calculations were performed using the ThermoCalc software with the TCNI-8 thermodynamic database which covers all the edge binaries and all the available ternaries of the common metal elements to predict the phase structure during the casting process. In CALPHAD calculation, the equilibrium state is predicted in every single point. So, by doing equilibrium calculation with varying temperature, the possible stable phase amount could be obtained, which represents the equilibrium solidification process. The dominate phase at a broad temperature imply the possibility of showing up after solidification. In real casting process, since the cooling rate is considerably large thus the equilibrium state can't be always reached. So, by adopting the Scheil-Gulliver's assumption[23], 1) the diffusion rate in solid phase is neglected 2) the diffusion rate in the liquid phase at all temperature is assumed to be infinite 3) the equilibrium could be also established at the solid-liquid interface. Under these conditions, the CALPHAD method could be used to model the solidification process during a rapid cooling effect. The equilibrium calculation is still performed at every thermodynamic state. However, the newly formed solid phase is excluded at every iteration step to get rid of the diffusion caused by solid phase. Those two solidification models simulate the solidification process in two extreme conditions: the annealing-like equilibrium solicitation and quenching-like rapid solicitation.

2.1.3. Using CALPHAD on corrosion prediction

Thermodynamic investigation of corrosion behaviors under various environments is a valuable tool for efficient design and optimization of corrosion resistant materials. Pourbaix diagram has been prevalently used to provide a basic thermodynamic guidance for the study of metal corrosion behaviors by mapping out all possible stable phases of an aqueous electrochemical system [24, 25]. However, the available Pourbaix in handbook are all about pure elements. In the application of alloy system, a simple superposition method is usually adopted [26]. While, this will inevitably neglect the interaction between the metal elements in the matrix and the oxide films evolution, e.g. the hydrated oxide phases and spinel phases won't be considered, especially for a HEA with multi-principle elements. Furthermore, the standard Pourbaix diagram is usually given in standard temperature and pressure. For an elevated temperature application, the use of the standard Pourbaix diagram is questionable. In this study, the CALculation of PHAse Diagrams (CALPHAD) method is used to examine the corrosion behavior of high entropy alloys. By substituting the axes of compositions and temperature of ordinary phase diagram into the potential (standard hydrogen electronic potential) and pH value (acidity), the Pourbaix diagram could be set up over a wide pH range under equilibrium conditions. The immunity, corrosion and passivity regions are indicated in the Pourbaix diagram to guide the selection of a suitable alloy for specific working conditions. The oxidation layer pitting and forming potential were calculated and compared favorably with published experimental results on CoCrFeNi, CoCrFeNiCu and $CoCrFeNiAl_{0.5}$ HEAs.

2.2. Experimental method

2.2.1. Alloy casting

To validate the computational design of HEAs, HEA specimens were prepared using an arc-melting furnace (model Edmund Bühler /MAM-1). Equimolar mixtures of the metal elements were placed in a water-cooled copper crucible under an argon environment. The purities of all raw elemental metal powders are higher than 99.5%. Before melting, metal powders were first mixed uniformly in a polystyrene ball mill jar for around 15 minutes and then pressed in a uniaxial die (0.5 inch inner diameter) at 350 MPa pressure to obtain the compressed green bodies, which were then melted in the water cooled copper hearth of the arc melter. To ensure homogeneity, the samples were inverted and re-melted 3-4 times in the arc-melter. The suction cast copper hearth with the cylinder shape casting dies in diameter of 2mm, 3mm, 4mm and 5mm are also available. For using suction cast, a vacuum chamber was connected on the bottom of the copper hearth. Experimental characterization

2.2.2. Alloy characterization

To prepare samples for characterization, a low-speed saw was used to cut through the HEA sample to expose a flat surface of cross-section. The exposed surface was subsequently ground by # 240, #400, #600, and #800 SiC sandpapers in sequence, before wet-polished with 1, 0.3 and 0.05 μm Al_2O_3 suspensions. The crystalline phase of the specimen was identified using X-ray diffraction with Cu Kα. The microstructure and the chemical compositions of the alloy were examined using field-emission scanning electron microscope FE-SEM (FEI, Quanta 3DFEG) equipped with BSE and EDS detector.

The density of the specimen was determined by measuring the samples weight and the volume. An analytical digital balance (Scientech, SA210) with a precision of 0.1 mg was used to measure the weight. Archimedes' principle was used to determine the sample volume. The hardness of the specimen was measured using a Vickers micro hardness tester under a load of 1kgf for 15 seconds.

To assess the fidelity of the CALPHAD simulations to the physical situation, experimental characterizations were performed on as-solidified MoNbTaTiVW, HfNbTaTiVZr, Cr_xMoNbTaVW and CrMoNbReTaVW HEA specimens to observe phase status. All HEA specimens were prepared in an arc-melter (Edmund Bühler /MAM-1). The overall specimen compositions were nominally equi-molar, based on starting powder proportions. An PANalytical Empyrean X-ray diffraction system with Cu Kα radiation was used to perform XRD measurements. Additional morphological and compositional characterizations were carried out on an FEI Quanta3D FEG dual-beam instrument, which houses a 30kV field-emission electron column, a 30kV high current Ga^+ ion column, secondary and backscatter electron (SE/BSE) detectors, an EBSD system, an EDS system, and an OmniProbe for specimen lift-out. TEM specimens were prepared following standard site-selective Ga^+ milling and lift-out procedures, and final thinned/cleaned in a Gatan PIPS II ion mill using 100eV Ar^+. Bright-field (BF) and phase-contrast electron imaging as well as selected area electron diffraction (SAD) were carried out on a JEOL JEM2011 microscope operated at 200KV.

CHAPTER 3. SENARY HIGH ENTROPY ALLOY MoNbTaTiVW

3.1. Design strategy and CALPHAD modeling

Following the strategy illustrated by Gao and Alman [10], alloy design started with inspection of available binary and ternary phase diagrams followed by CALPHAD modeling. For the Mo-Nb-Ta-Ti-V-W senary system, formation of isomorphous solid solution in BCC-A2 crystal structure was observed in all 15 edge binary systems [27]. Most of the solid solutions cover extremely wide temperatures, except the Ta-V system where TaV_2 Laves phases were reported, and the Ti-containing systems, since pure Ti undergoes polymorphous phase transition at 882^{o}C [27]. Phase separation was reported in the Ti-W system at 10-65 at% W and temperature of 750-1220^{o}C [27]. For the Ti-Nb system at temperatures roughly below 550^{o}C, little solubility was observed between BCC Nb and HCP Ti [27]. Furthermore, formation of BCC solid solution over wide ranges of composition and temperature was reported in 18 constituent ternary systems that were experimentally studied, however, there are no reports on Mo-Ta-W and Nb-V-W ternaries. In addition, there were no ternary compounds reported for these 18 ternaries [27]. Based on the binary and ternary experimental information summarized above, it is concluded that formation of BCC solid solution at the MoNbTaTiVW composition is highly likely considering: (1) formation of isomorphous solid solution in all 15 binaries; (2) formation of extended solid solution in 18 ternaries; (3) lack of formation of stable compounds in all systems except Ta-V; (4) chemical similarity among Mo, Nb, Ta, V and W; (5) formation of BCC solid solution was already confirmed in MoNbTaW and MoNbTaVW compositions.

CALPHAD calculations were performed using the ThermoCalc software with the TCNI-7 thermodynamic database [28] which covers all the edge binaries and some ternaries of the Mo-Nb-Ta-Ti-V-W system. Figure 3.1 (a) shows the calculated mole fraction of stable phases during

equilibrium solidification. The predicted equilibrium liquidus temperature is 2533^{o}C, and the equilibrium solidus temperature is 2246^{o}C. The temperature window for a stable single BCC phase is extremely wide: this suggests an extreme thermal stability for MoNbTaTiVW HEA. The HCP phase is predicted to from at a low temperature of 572^{o}C, with a very minor mole fraction of about 0.12 at 400^{o}C. Due to the extreme slow diffusion in refractory metals that contain Mo, Nb, Ta and W, it is anticipated that HCP will not form in this alloy.

The MoNbTaTiVW HEA samples were fabricated in a vacuum arc-melting process. As the cooling rate during the arc-melting process is usually high, the equilibrium solidification path cannot be maintained. To estimate the effect of non-equilibrium solidification on the phase fraction and the composition, the Scheil simulation was performed for the extreme case: no diffusion in the solid while equilibrium was assumed for the liquid. The results can be interpreted as the worst segregation scenario, since in reality diffusion does occur more or less in the solid phase at high temperatures depending on alloy compositions. As expected, only BCC was formed due to lack of competition of other crystalline phases at high temperatures (see Figure 3.1 (b)) and large configurational entropy of mixing. Scheil modeling predicts a solidus temperature of 1661^{o}C. The composition evolution in liquid and BCC during Scheil solidification is shown in Figure 3.1 (c) and Figure 3.1 (d) respectively. As the temperature decreases, it is predicted that elements are depleted in the descending order W > Ta > Mo > Nb in liquid while more Ti is enriched than V (Figure 3.1 (c)). The composition in the liquid follows the exact order of their melting points during Scheil solidification. As for BCC phase, the simulation predicts that the composition of initial solid phase at the very beginning of solidification is enriched in W followed by Ta but is depleted of V and Ti, while Mo and Nb seem to be at the nominal composition. At a low temperature, W content in the solid phase decreases more rapidly than Ta, while V and Ti contents increase rapidly at a

roughly similar rate. In contrast, Mo and Nb contents only increase very marginally until 2200°C. Due to the continuous cooling in a non-equilibrium path, compositional fluctuation in wide range is anticipated.

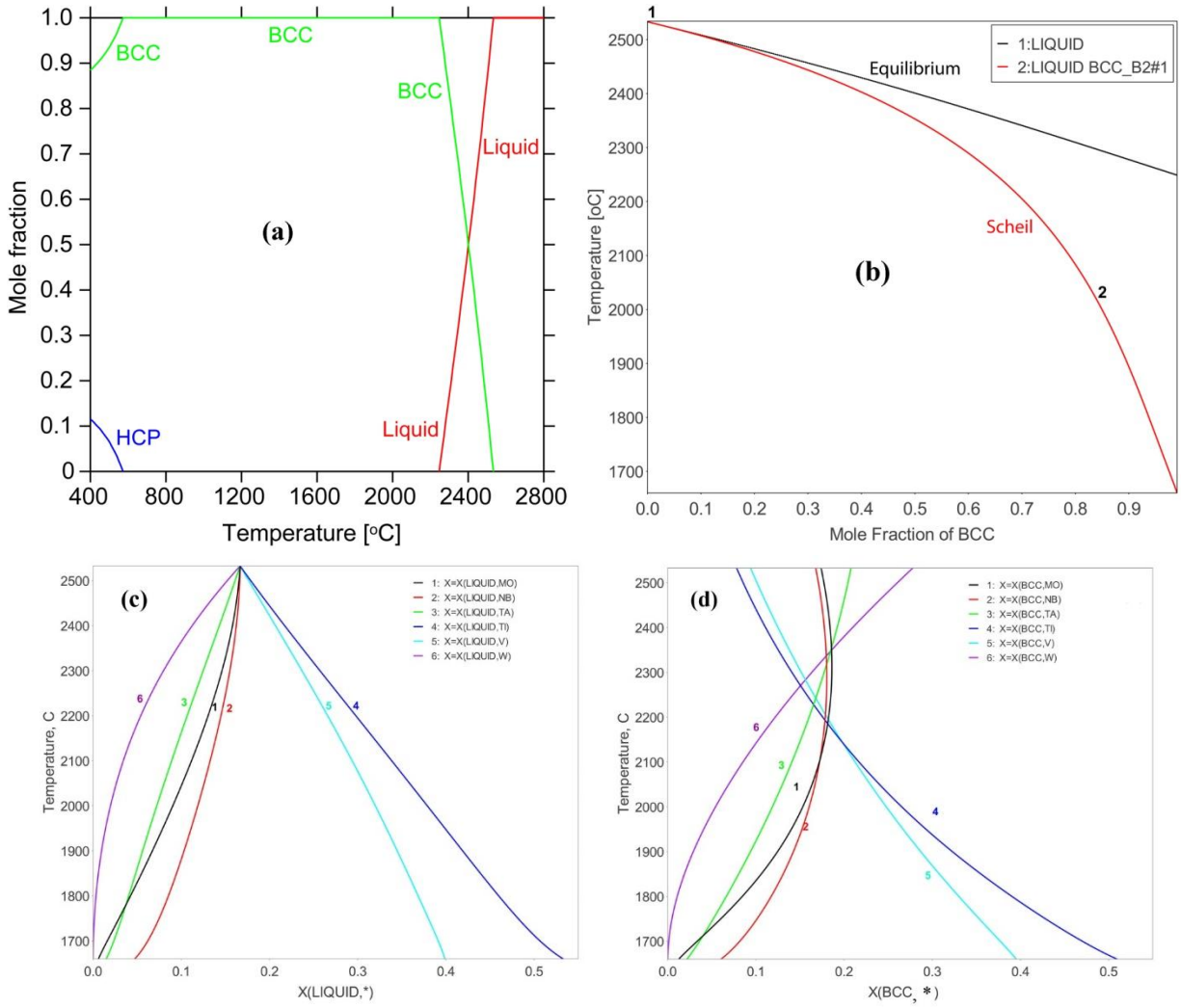

Figure 3.1 Equilibrium solidification using the Scheil model; (b-d) non-equilibrium solidification using the Scheil model: (b) mole fraction of solid phase, (c) composition of liquid, (d) composition of BCC.

3.2. X-ray diffraction validation

X-ray diffraction (XRD) patterns of the powder mixture and the as-solidified MoNbTaTiVW HEA sample are shown in Figure 3.2 (a) and Figure 3.2 (b), respectively. The peaks in the powder mixture can be traced back to the pure metals of Mo, Nb, Ta, Ti, V, and W. After the arc-melting process, all the XRD peaks are congruent with the single BCC phase, see the appropriate indices identified in Figure 3.2 (b). This result confirms the computational prediction shown in Figure 3.1 (b), which says that after solidification, MoNbTaTiVW HEA is a dominate BCC structure. The lattice constant of MoNbTaTiVW HEA can also be determined as 0.3216 nm (see Table 3.1) by the bragg's law [29]. The average lattice, calculated from the mixture rule, is found to be 0.3150 nm, which is 1.4% smaller than the measured XRD result. It's likely that solid solution ordering occurred in the alloy. The nearly absence of the peak (222), which should be detected in a BCC structure, also implies the possible solid solution ordering in the alloy.

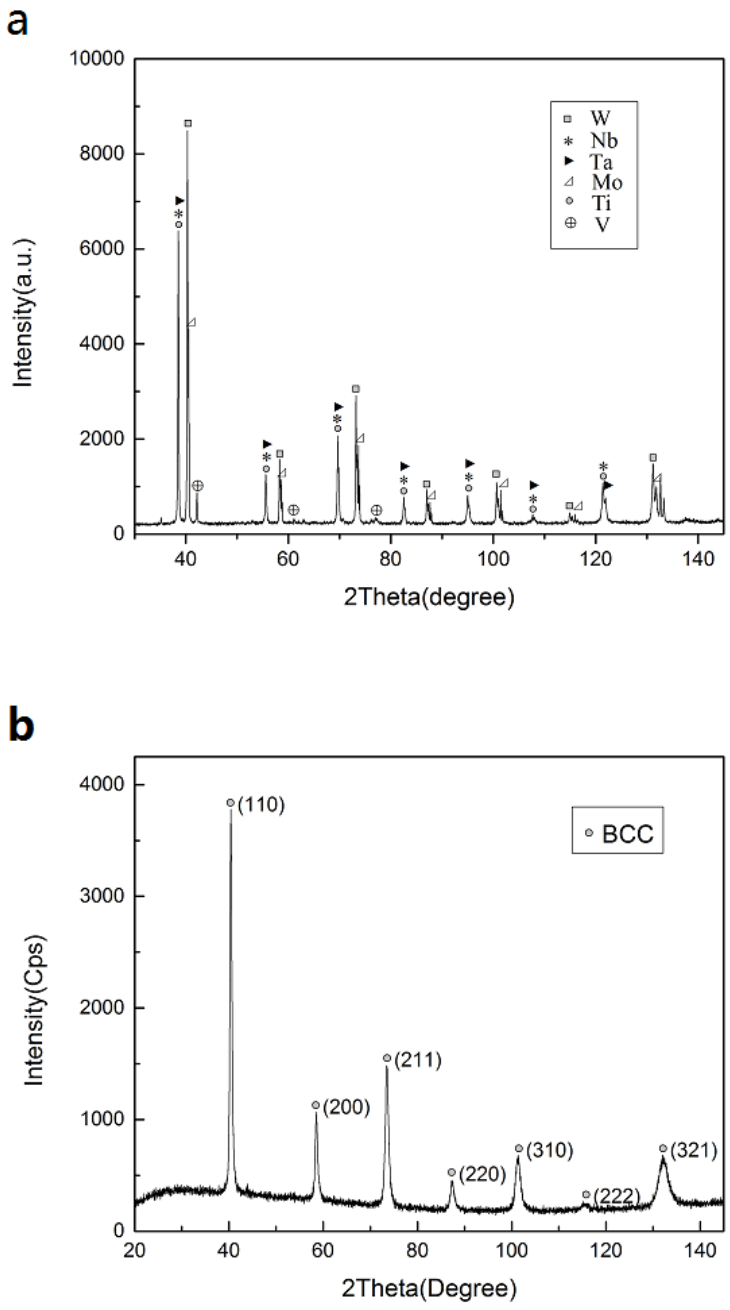

Figure 3.2 XRD pattern of (a) powder mixture and (b) as-solidified MoNbTaTiVW alloy

3.3. Density and hardness

The density of the MoNbTaTiVW alloy was determined to be 11.7 g/cm^3 (see Table 3.1). The theoretical density of a disordered solid solution can be calculated from the equation:

$$\rho_{theor} = \frac{\sum c_i A_i}{\sum \frac{c_i A_i}{\rho_i}} \quad (3\text{-}1)$$

where c_i is the atomic percentage of an element; A_i is the atomic weight; and ρ_i is the density of the pure element *i*. The calculated theoretical density is 10.85 (Table 3.1), which is around 7% smaller than that of the experimentally measured value. This indicates the existence of solid solution ordering induced volume change.

Table 3.1 The lattice constant *a*, Vickers hardness H_v , density ρ, the melting temperature T_m [28] Atomic diameter *d* [27], and the Pauling Electronegativity[30] of the HEA alloy and the pure metal feedstock.

Metal	W	Nb	Mo	Ta	V	Ti	Alloy Calc	Alloy Exp
a, nm	0.3158	0.3301	0.3147	0.3303	0.3039	0.2950	0.3150	0.3216
H_v, MPa	3430	1320	1530	873	628	970	1459	4954
ρ, g/cm^3	19.25	8.57	10.28	16.65	6.11	4.51	10.85	11.70
T_m, K	3422	2477	2623	3017	1910	1668	2806	-
d, Å	4.04	4.16	4.02	4.18	3.84	4.0	-	4.04
Pauling Electronegativity	2.36	1.6	2.16	1.5	1.63	1.54	-	-

The Vickers micro-hardness H_v was tested at five randomly selected sites on the HEA sample. The averaged value was found to be 4954 +/- 198 MPa. The experimental micro-hardness value is higher than both the average hardness of the mixture and the hardest metal element in the system. The solid solution hardening mechanism is believed playing an important role here. In comparison, the micro-hardness for a 5-element MoNbTaVW refractory high entropy alloy reported by Senkov et al. is 5250 MPa, just slightly larger than the measured senary MoNbTaTiVW alloy hardness. Both MoNbTaTiVW and MoNbTaVW samples have a similar grain sizes of around 20-40 μm. However, due to the high W content, the simple average hardness of the 5-

element MoNbTaVW is slightly larger. The tensile strength can be estimate by approximate relationship $\sigma=H_v/3$ [31], which gives a value of 1651 MPa.

3.4. Microstructure and segregation validation

SEM backscatter electron images of the MoNbTaTiVW HEA alloy were taken on the fine polished sample surface. Most of the grains sizes in the MoNbTaTiVW HEA were found to be around 20 μm to 40 μm. The different brightness between the inter-granular regions and the intra-granular regions indicates the existence of elemental segregation during the solidification process. In a backscatter image, the lighter Z direction contrast inside the granular regions was most likely formed with heaver metal elements, which in this case, W and Ta. And the darker inter-granular regions should be filled with lighter elements. This is also proved by the EDS mapping results,

Figure 3.3 (b) to (h) and Table 3.2. The W and Ta are mostly seen inside the granular structures as shown in Figure 3.3 (c) and (d), while Mo, V, Nb, and Ta can be clearly seen with enrichments in the inter-granular regions, Figure 3.3 (e)-(h). The atomic percentages of the entire scanned area, together with point measurements in both the dentrite region (point 1) and inter-dendrite region (point 2), are listed in Table 3.2. The averaged elemental ratios of a MoNbTaTiVW HEA sample prepared by arc-melting were determined by EDS area scan. The results show that arc-melting samples deviate from the ideal equality of equiatomic design point, because of the different evaporation losses in the arc-melting process. Following Leo *et al*. [32], the partition cofficient $K = C_d/C_{id}$, was used to evaluated the micro-segregation quantitatively. Micro-segregation is caused by the different solidification temperatures associated with each element in the alloy system. The elements with the high melting point in the system will solidify first and form the granular structures, forcing those lower melting point elements into the inter-granular regions. The microsegration on account of non-equlibrium solidification is also prediceted in the CALPHAD

simulations. Figure 3.1 (c) shows the element contents in the HEA liquid at different temperatures. The solubility of W drops most rapidly and thus is concentrated into those dentrite cores. The experimentally measured partition cofficient of W is larger than that of Ta, which is consistant to the observed sharper decreasing of W's concentration gradient in Figure 3.1 (c). For elements Mo and Nb, the partition cofficients are found to be colse to unity. That means barely any segregations would happen for Mo and Nb during the solidification process. In agreement with the experimental results, Figure 3.1 (c) simulation shows that the Mo and Nb compositions keep nearly constant values at a temperature above 2200 ^{o}C, making Mo and Nb uniformly distributed in the HEA. Further examination of Figure 3.1 (c) shows Nb has a higher simulated concentration near the solidus point than that of Mo, which explains the slightly lower partition coefficient value of Nb found in the experimental measurements. The enrichments of elements V and Ti in the inter-dendrite regions are conformed by both simulations and the measurements.

Table 3.2 EDS Composition analys is results for MoNbTaTiVW HEA, Fig 3a, (at.%).

Metal	W	Nb	Mo	Ta	V	Ti
Area(C_{aver})	17.78	20.45	14.75	16.78	16.87	13.37
1 (C_d)	27.10	19.26	14.51	20.11	10.80	8.33
2 (C_{id})	6.70	20.34	12.84	11.21	26.50	22.41
$K = C_d/C_{id}$	4.04	0.95	1.13	1.80	0.41	0.37

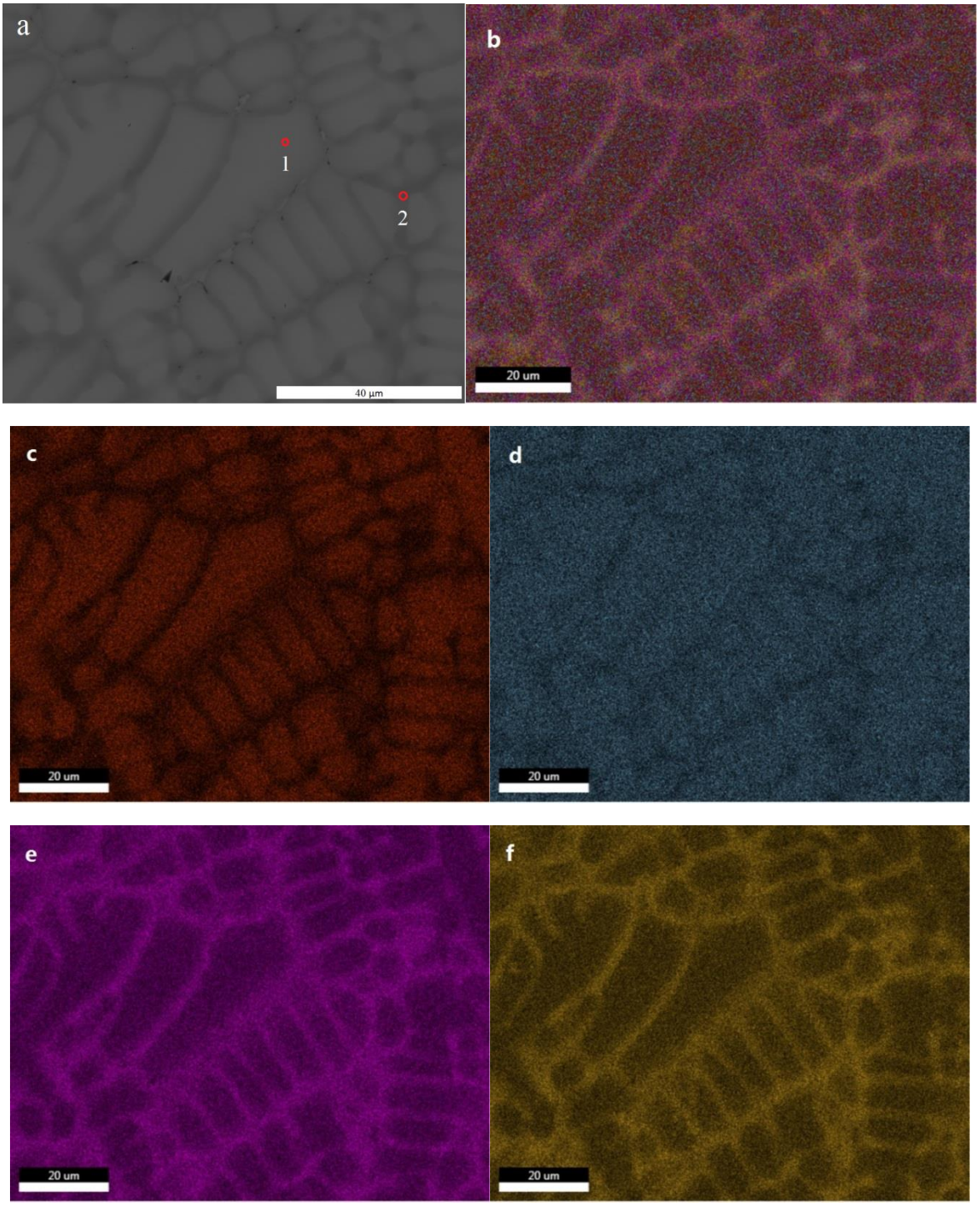

Figure 3.3 (a) SEM backscatter electron image (polished cross-section of the HEA, EDS point measurement locations— 1 and 2 in Table 3.2— are marked), EDS mapping of (b) Total, (c) W, (d) Ta, (e) Nb, (f) Mo, (g) V, (h) Ti.

(Figure 3.3 cont'd)

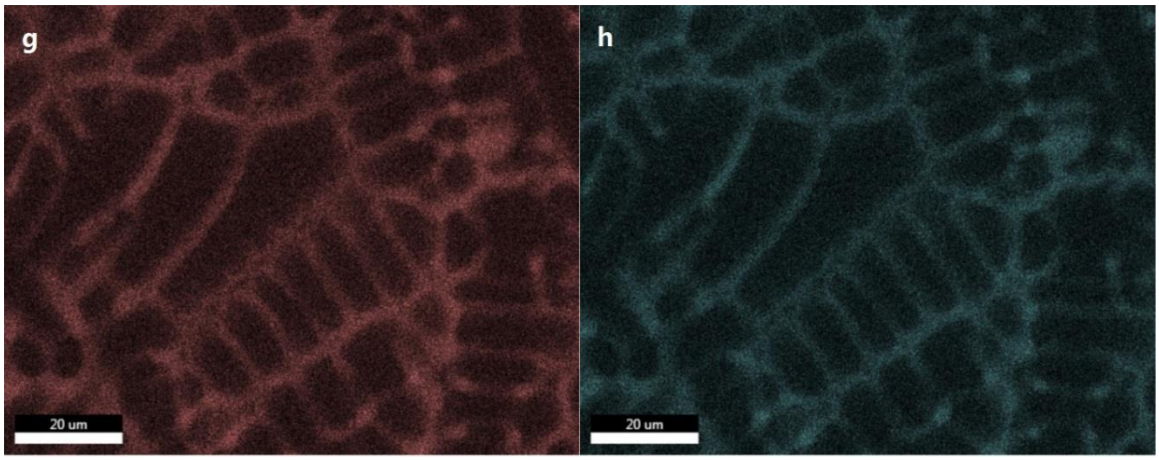

The composition inhomogeneity between the dendrite and inter-dendrite regions is direct reflected by the EDS line scan results. As shown in Figure 3.4 (a), atomic compositions were determined along 3 lines, with a point scan separation of 0.1 μm. The elemental percentages were plot in Figure 3.4 (b), (c) and (d), respectively. Based on the EDS line scan results, Mo and Nb contents were found to be nearly constant in both inter-dendrite region and dendrite region; Ta and W were enriched in the dendrite region; and Ti, V were enriched in inter-dendrite region, as discussed above.

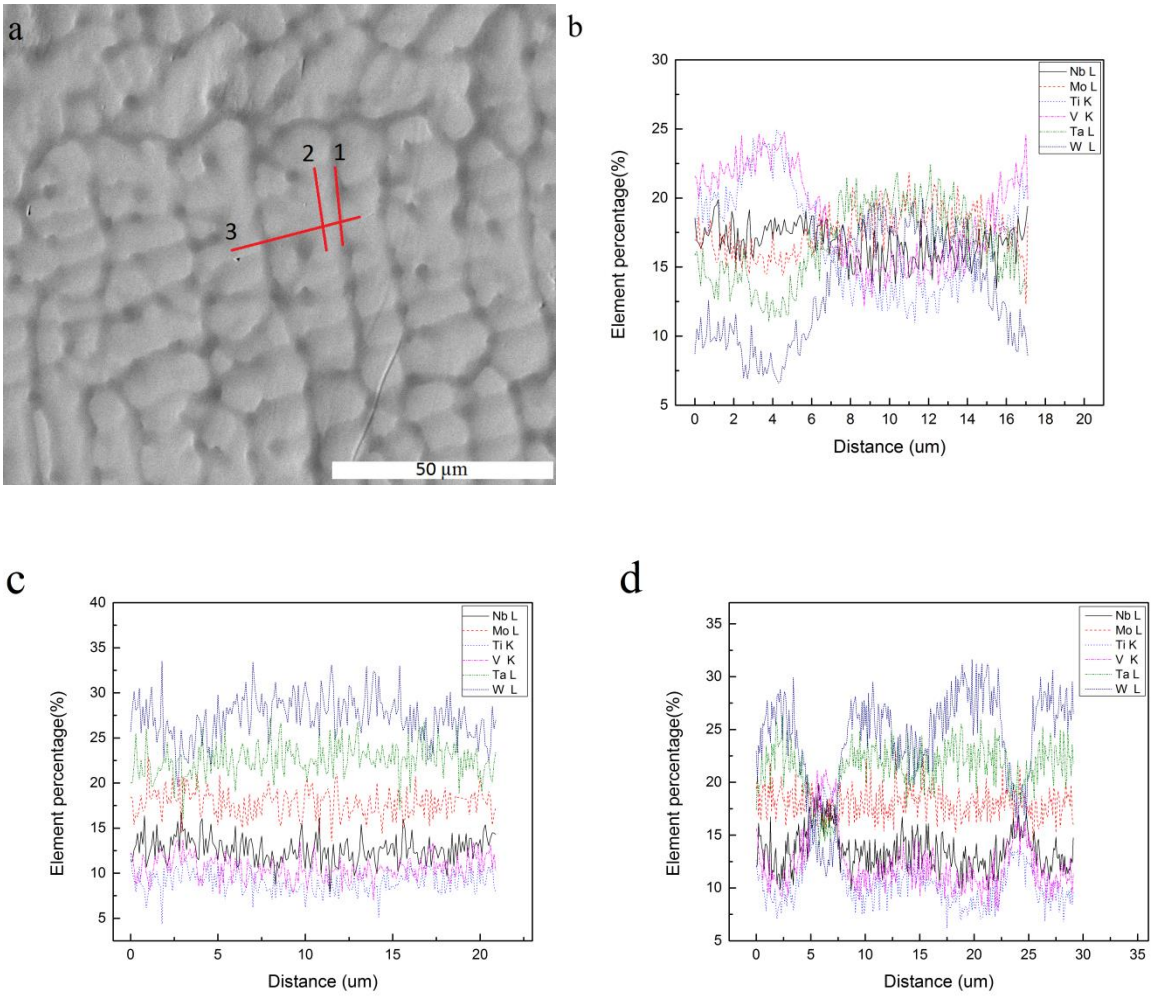

Figure 3.4 (a) SEM image (polished cross-section of the HEA, EDS line measurement locations 1, 2 and 3 are marked), atom percentage of (b) Line 1, (c) Line 2, (d) Line 3

3.5. Conclusion and outlook

A single-phase senary refractory high-entropy alloy, MoNbTaTiVW, was designed based on CALPHAD simulations and inspecting available binary and ternary phase diagrams, and was successfully validated experimentally. The alloy has a body-centered cubic structure as predicted in the CALPHAD simulations. According to the classical Hume-Rothery rule, in order to form HEA solid solution, the atomic size differences should be less than 15%. According to Table 3.1, the largest atomic size difference is around 8% in the MoNbTaTiVW system. Zhang *et al.* [33]

also proposed a rule after surveying a large compositions of alloys, which basically request the liquid enthalpy value range between -15 and +5 kJ/mol.

The lattice constant and density of the alloy were determined to be 0.3216 nm and 11.7 g/cm^3 respectively. The lattice constant and the density are slightly larger than the theoretically averaged values, predicted using the simple mixture rule without considering the influence of possible solution ordering. The alloy samples prepared by arc-melting method have a dendritic grain structure with a grain size in the order of 20 to 40 μm. The Vickers micro-hardness of the as prepared HEA samples is about 5.0 GPa, which is much higher than both the hardest element in the system and the averaged value predicted by the mixture rule. This enhanced hardness value is caused by the solid-solution hardening mechanism as predicted by the basic HEA theory. The compositions of BCC phase in the HEA at different temperatures were calculated using the Scheil model in CALPHAD to assist the understanding to HEA micro-segregation. The micro-segregation of HEA samples, prepared by arc-melting process, was experimentally measured, which confirmed the CALPHAD predictions. Both simulation and measurements showed that in the MoNbTaTiVW system, W and Ta would have enrichment inside the dendrite regions that were formed at higher temperatures, while having depletion in the inter-dendritic regions. Elements V and Ti were mostly existence in the inter-dendritic regions. Mo and Nb segregation were much less severe. According to both the simulations and experimental results, the micro-segregation of MoNbTaTiVW HEA is caused by the different solidification rates for different constitutional elements. The CALPHAD based HEA selection/design methodology clearly demonstrated the capability for selection and design of senary high-entropy alloys.

Although HEA was discovered about a decade ago, only in recent few years it's excellent properties were caught materials scientists' wide intensive attentions. More intensive studies are

currently supported by basic science and industry funding agencies and academic institutes. Brand new research areas may emerge soon in the near future. The following areas would be important for extending the present understanding of this amazing and novel alloy—to name a few fast emerging ones— new integrated methods applied in efficient searching/design the optimized single phase HEA with higher mixing entropy and more stable structure; dislocation dynamics in-situ study; high temperature structure and strength/toughness stability study; light weight high strength HEA development; 3D additive manufacturing defect free HEA development; dopant effects on inter- and intra-grain boundary study; and reliable oxidation and corrosion resistance HEAs.

CHAPTER 4. SENARY REFRACTORY HIGH-ENTROPY ALLOY $Cr_xMoNbTaVW$

4.1. Introduction

Refractory alloys are used in many industry sectors—chemical processing, aerospace, and microelectronics. To design a refractory alloy, the conventional design approach is to use single principal metal refractory elements, such as W, Mo, Nb, and Ta. Using single-element based alloy design imposes limitations, not only in terms of compositional availabilities, but also the range of achievable properties. Poor low-temperature ductility and low oxidation resistance are common shortfalls for conventional refractory alloys [34].

A new alloy development strategy, namely multi-principal-element alloys or high-entropy alloys (HEAs), has been proposed by Yeh et al. [9] and developed by many researchers in recent years. The HEA approach employs five or more principal metallic elements at near equal molar ratios in a solid solution, with atomic percentage of each element varying between 5% and 35%. The high configurational entropy of mixing can stabilize solid-solution phases than intermetallic phases. As reported in literature, HEAs can be tailored to possess excellent wear and oxidation resistance [35], high temperature strength [36] and low temperature ductility [37]. Recently, a new branch of refractory alloys—refractory HEAs—has been proposed and characterized by Senkov et al. [22, 38, 39] by extending the HEA design concept to refractory alloys. It has been shown that the high temperature strength of refractory HEAs MoNbTaW and MoNbTaVW with the body-centered cubic (BCC) structure at high temperatures are even higher than that of conventional super-alloys [22]. Other HEA compositions, such as MoNbTaTiVW [40], HfMoTaTiZr [39], HfNbTaTiVZr [41] and HfMoNbTaTiZr [42], were also experimentally studied. However, to date the progresses in the design and validation of refractory HEAs are slow, mainly due to the lack of

effective design guidance. For a typical HEA composition of more than five principal elements, the combinatorial possibilities follow factorial growth. Recently an efficient strategy was proposed by Gao and Alman [10, 43] to accelerate single-phase HEA design by integrating experimental phase diagram inspection, CALPHAD (CALculation of PHAse Diagrams) modeling and first-principle density functional theoretical calculations.

The goal of this chapter is to demonstrate that senary refractory high-entropy alloys $Cr_xMoNbTaVW$ (x = 0.5, 1, and 2 in molar ratio) can be tailored over a certain range of Cr contents to form BCC phase HEAs with different microstructures and physical properties. The phase stability of $Cr_xMoNbTaVW$ HEAs was first evaluated using the CALPHAD method. Then experimental effort was applied to validate the phase structures, the microstructures, and the influence of Cr content.

4.2. CALPHAD modeling

4.2.1. Phase diagrams

All the CALPHAD modeling were carried out using the TCNI7 thermodynamic database via ThermoCalc^{TM} software [15]. Although TCNI7 database is primarily optimized for Ni-based super-alloys, it does cover all the edge binaries of the Cr-Mo-Nb-Ta-V-W system. To show the influence of Cr addition to the MoNbTaVW system, the pseudo-binary phase diagram of Cr_x MoNbTaVW is shown in Figure 4.1. For $x \leqslant 5$, the BCC phase is the primary crystallization phase. With increasing Cr molar ratio, both the liquidus and solidus temperatures decrease while the solvus temperature increases. As a result, the single BCC phase field shrinks with the increasing of Cr ratio, due to the formation of competing BCC#2 phase that is rich in Cr and V, μ phase, and C15 phase. Predicted equilibrium compositions of BCC#1 and BCC#2 are listed in

Table 4.1. The pseudo-binary phase diagram with a wider Cr content can be found in Figure 4.1. These results have been published [44].

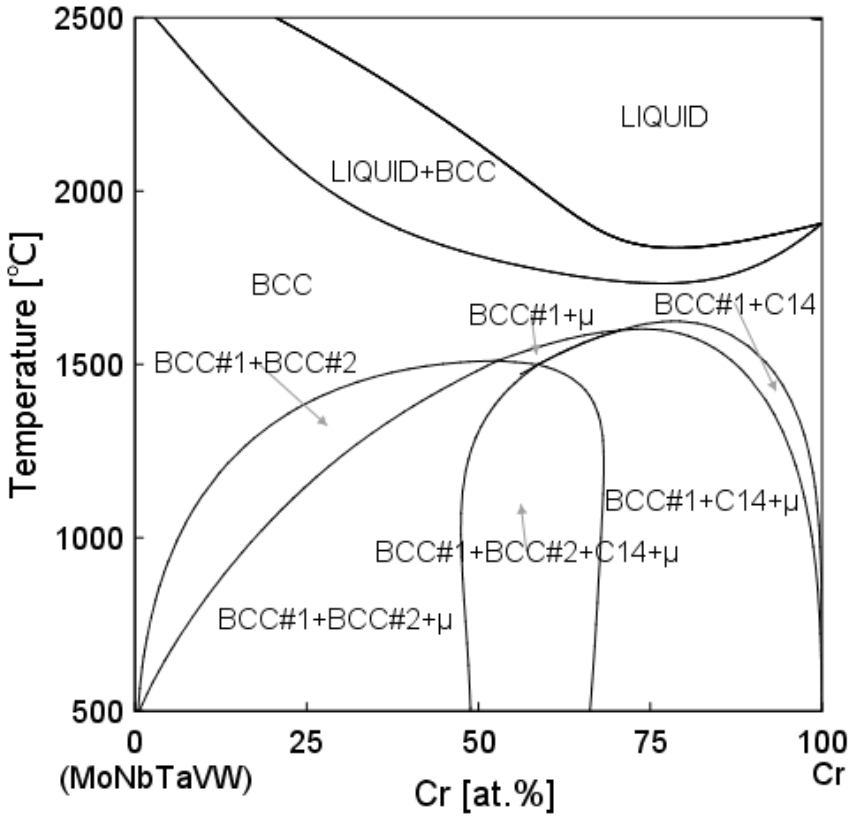

Figure 4.1 Predicted pseudo-binary section of $Cr_xMoNbTaVW$

Table 4.1 Predidcted equilibrum phase compositions at (at.%).

Condition	Phase	Cr	Mo	Nb	Ta	V	W
x=0.5	BCC#1	6.1	19.2	19.2	19.3	17.0	19.2
T=1000 °C	BCC#2	54.8	3.0	1.9	1.0	36.0	3.3
x=1	BCC#1	5.7	20.2	20.4	20.6	13.0	20.1
T=1000 °C	BCC#2	61.0	2.6	1.5	0.8	31.4	2.7
x=2	BCC#1	16.8	17.6	17.9	18.5	11.4	17.8
T=1300 °C	BCC#2	60.6	5.4	4.4	2.9	22.0	4.7

4.2.2. Solidification of Cr-Mo-Nb-Ta-V-W

Predicted equilibrium and non-equilibrium solidification (Figure 4.2(b)-(d), (f), (h)) behaviors of $Cr_xMoNbTaVW$ are shown in Figure 4.2. The predicted equilibrium phase mole fraction plots (Figure 4.2(a), (e), (g)) show formation of a single BCC phase at higher temperatures. The BCC phase starts to form at 2540 °C in CrMoNbTaVW, 2616 °C for x = 0.5, and 2683 °C for x = 2. The BCC#2 phase starts to form at T ≤ 1276 °C for CrMoNbTaVW, T ≤ 1100 °C for x = 0.5, and at T ≤ 1421 °C for x = 2.

The actual cooling rate of the HEA sample preparation process, in a lab arc melting furnace, is way higher than the equilibrium assumption, thus it is expected that the observed microstructures may deviate from the predicted equilibrium solidification. The non-equilibrium solidification was simulated using the Scheil-Gulliver models [23, 45], which assumed equilibrium in the liquid but no diffusions in the solid phase(s). Only disordered BCC phase (BCC#1) was observed at T ⩾ 1607 °C for CrMoNbTaVW (Figure 4.2 (b)), T ⩾ 1705 °C for x = 0.5 (Figure 4.2 (e)), and T ⩾ 1604 °C for x = 2 (Figure 4.2 (g)). The BCC phase is found to be the disordered type [44]. The elemental composition evolutions in the liquid and BCC phases during the Scheil solidification are shown in Figure 4.2 (c) and (d) respectively to evaluate the possible micro-segregation in CrMoNbTaVW. At the beginning of solidification, it is predicted that W, Ta and Mo are depleted in the liquid while Cr and V are enriched. The solid BCC phase in the form of dendrites observed in the experiments is predicted to be enriched in W, Ta and Mo but depleted in Cr and V. At the later stages of the solidification where the inter-dendrites form, it predicts that inter-dendrites will be enriched in Cr and V but depleted in W and Ta. The Scheil-Gulliver solidification for $Cr_2MoNbTaVW$ predicates the formation of C14 laves phase and C15 laves phase at the last stage of the solidification. However, the predicted contents of C14 and C15 phases are extremely low

(0.23% and 0.81%), and they were not detected by the XRD measurements. In short, the non-equilibrium solidification simulations suggest that micro-segregation is very likely to occur in alloy CrMoNbTaVW.

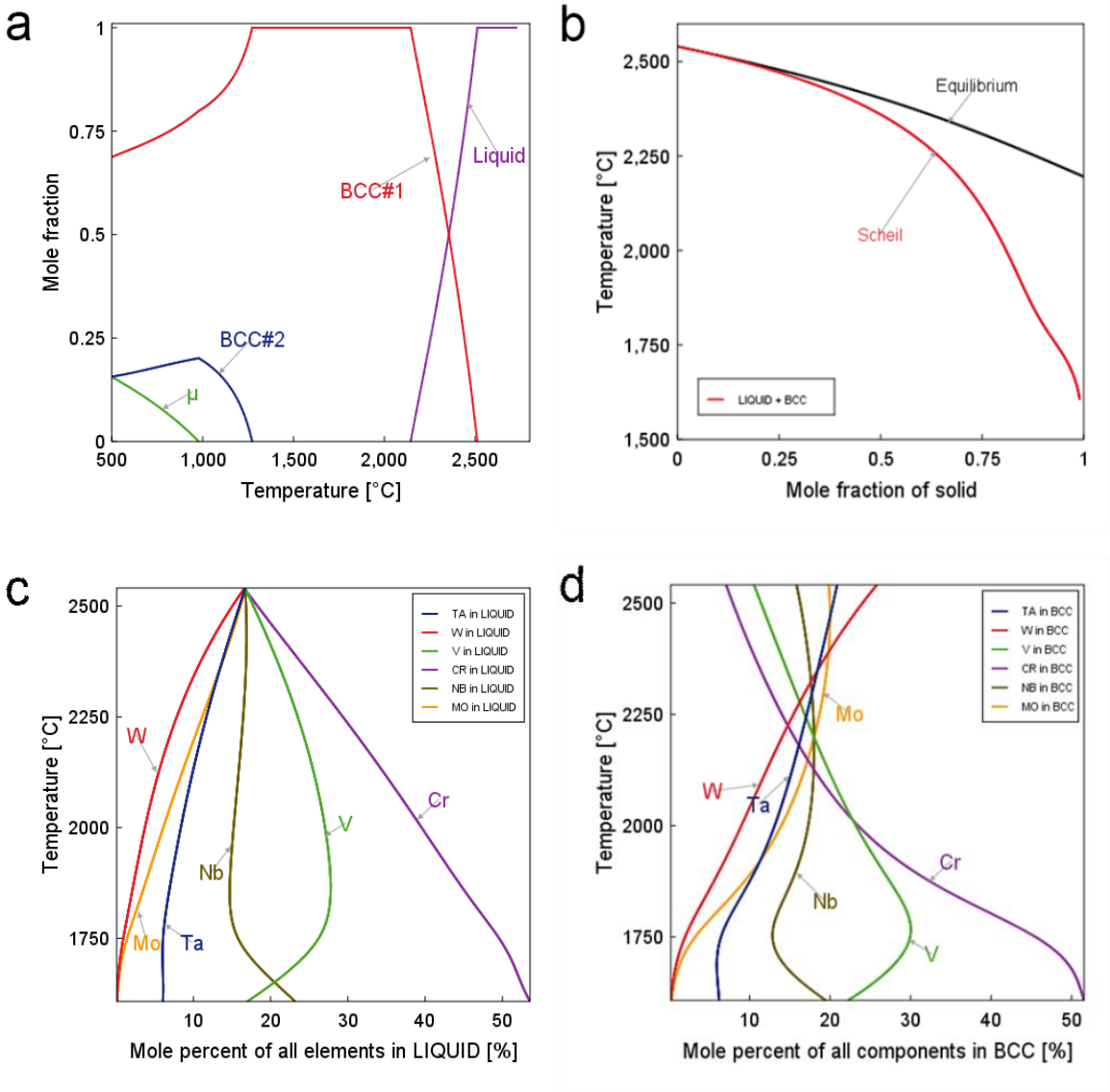

Figure 4.2 Predicted equilibrium phase mole fraction: (a) $Cr_1MoNbTaVW$, (e) $Cr_{0.5}MoNbTaVW$ and (g) $Cr_{2.0}MoNbTaVW$; Scheil solidification: sold phase mole fraction (b) $Cr_1MoNbTaVW$, (f) $Cr_{0.5}MoNbTaVW$ (h) $Cr_{2.0}MoNbTaVW$; the composition of (c) the liquid phase and (d) BCC phase in $Cr_1MoNbTaVW$.

(Figure 4.2 cont'd)

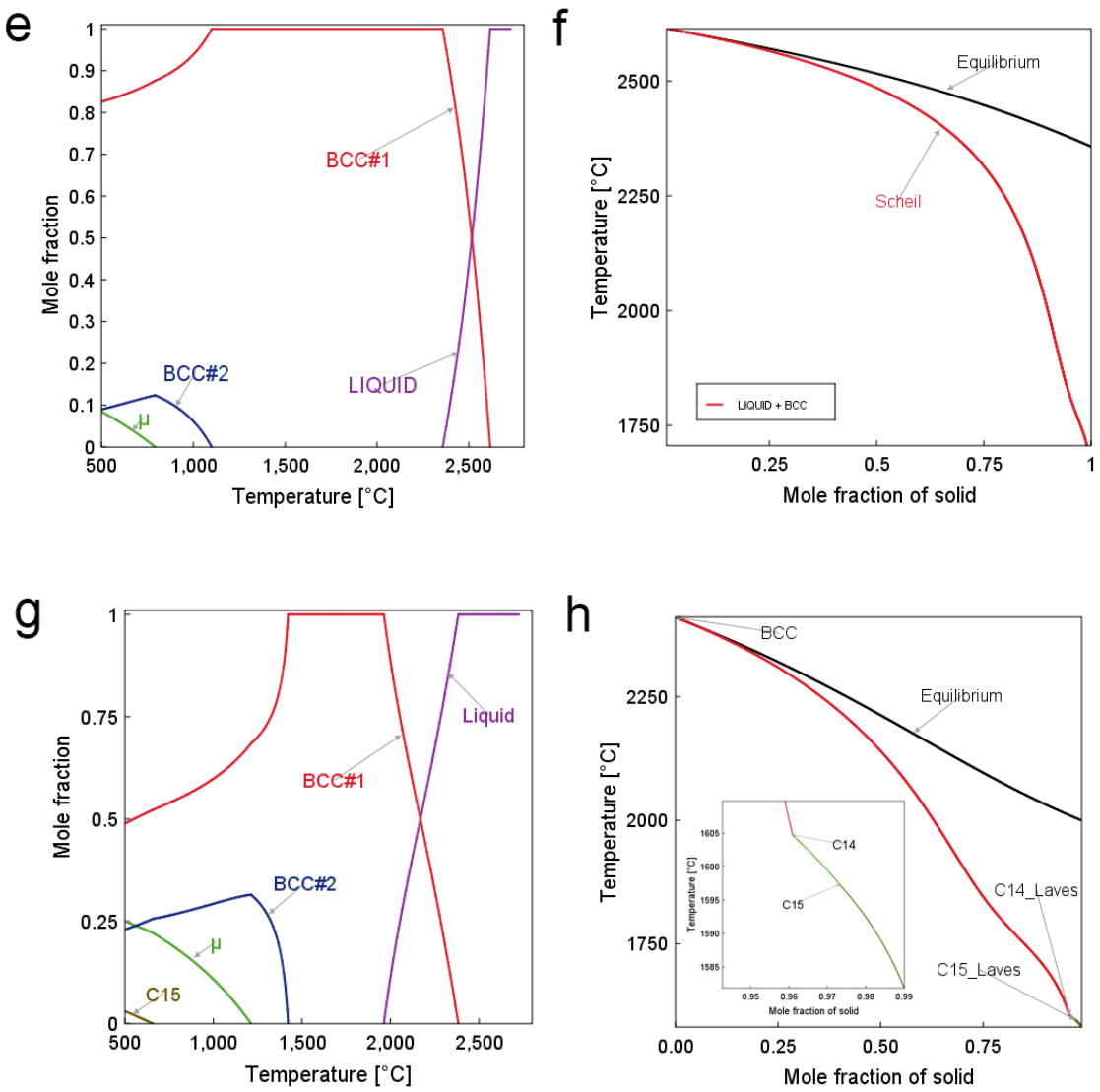

The composition data for two sub-lattices of BCC are calculated. The BCC lattice contains two interpenetrating simple cubic sub-lattices, one sub-lattice consisting of the cube corners, and the other sub-lattice consisting of the cube centers. In an ordered state, since the certain atom will appear at the certain spatial position, the hypothesis divided sub-lattice 1 and 2 will occupied by two different combinations of elements. That caused the elemental site occupancy of sub-lattice 1 and sub-lattice 2 different to each other. However, in a completely disordered state, each sites can be occupied by any element, thus the probability for a given site containing an atom of a given

type is equal to the probability for the other site. [46] So during the ThermoCalc calculation, when the site occupancy of the first and second sub-lattice (sub-lattice 1 and sub-lattice 2 in Figure 4.3.) are equal the phase is disordered [47]. Figure 4.3 shows the site occupancy fractions are identical for both the sub-lattices #1 and the sub-lattice #2.

The site fractions of sub-lattice 1 and sub-lattice 2 of each BCC structure were plotted based on Thermo-Calc^{TM} simulations. After employing the TCNI7 database, all six elements of Cr, Mo, Nb, Ta, V and W were defined and all the relevant phases were restored. Then the POLY3 module of the Thermo-Calc^{TM} was activated for the property diagram calculations. For the initial conditions, the ambient temperature and pressure were set and the mole fractions of all the elements were set to be 16.67%. The equilibrium single point calculation was initiated to determine a starting point for the step loop. The temperature range and increment were then set for the rest of step calculations. After the completion of step calculations, the site fractions of BCC#1 and BCC#2 phases were plotted in the POST module (Figure 4.3(a) and (b)).

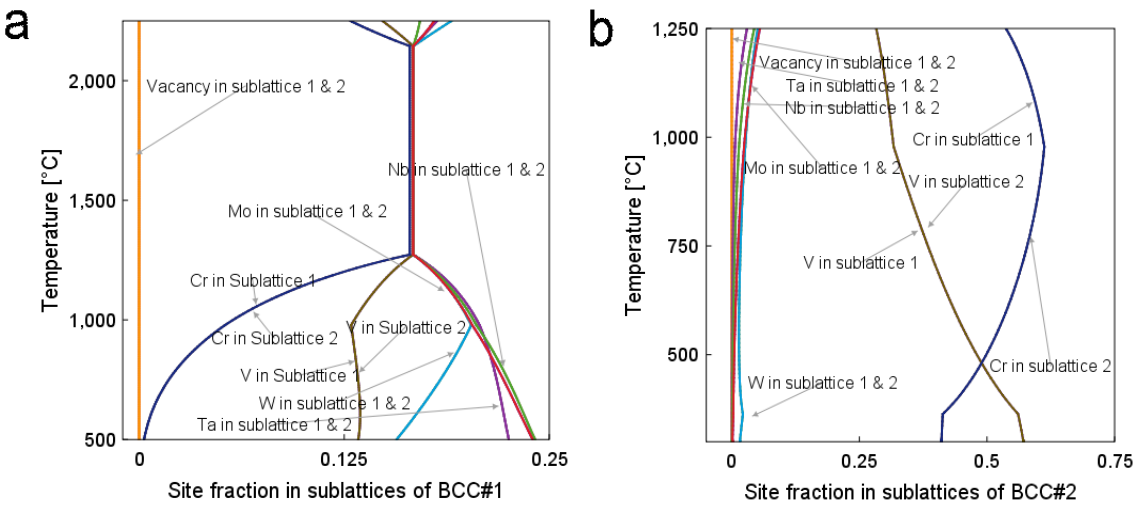

Figure 4.3 Sub-lattice 1 and sub-lattice 2 compositions of (a) BCC#1 and (b) BCC#2 in $Cr_1MoNbTaVW$

4.3. Experimental results and discussions

4.3.1. Material synthesis and characterization methods

The refractory HEA $Cr_xMoNbTaVW$ system with different chromium contents (x= 0.5, 1, and 2) was prepared by arc melting (model Edmund Bühler /MAM-1) the constituent elements in a water-cooled copper hearth to validate the CALPHAD modeling. Around 2 gram of commercial chromium, molybdenum, niobium, tantalum, vanadium and tungsten powders in total, with purity higher than 99.5%, were mixed inside a polystyrene ball mill jar before melting. During the melting process, the ingots were inverted and re-melted for 4 times to ensure homogeneity. The cooled ingots were then mounted into epoxy resin (SamplKwick fast cure acrylic resin, produced by Buehler) for easy handing and retention. The mounted specimens were cut through the ingot using a low-speed saw in order to expose a flat surface of the sample cross-section. The exposed surface was subsequently ground by #240, #400, #600, and #800 SiC sandpapers in sequence, before wet-polished with 1, 0.3 and 0.05 μm Al_2O_3 suspensions. An X-ray diffractometer (Empyrean, PANalytical) equipped with Cu Kα radiation (λ = 0.15406 nm) was used for the identification of the structure, with the 2θ scan ranging from 5 to 145 degrees at a rate of 10 degree per min at 45 kV and 40 mA. Field-emission scanning electron microscope FE-SEM (FEI, Quanta 3DFEG) equipped with backscatter electron (BSE) and energy dispersive spectroscopy (EDS) detectors was used to characterize the microstructure and the chemical compositions of the samples along the cross-sections.

The bulk compositions of the alloys were estimated by EDS area scan, as listed in Table 4.2. The different evaporation losses during the arc-melting process caused a small deviation from the design point. The elemental proportions of Table 4.2 are used as the bulk concentrations to estimate the theoretical average properties of density, hardness and lattice constant. The measured

compositions were also used to rerun the CALPHAD simulations for $Cr_xMoNbTaVW$ ($x \approx 0.5, 1, 2$) and the results/features were found to be very similar to the results presented in Figure 4.2 [44].

Table 4.2 EDS bulk composition analysis results for $Cr_xMoNbTaVW$ HEA, (at.%).

	Cr	Mo	Nb	Ta	V	W
x≈0.5	8.43	16.95	19.65	15.91	23.10	15.95
x≈1.0	17.89	16.31	18.15	13.94	19.59	14.12
x≈2.0	27.05	13.68	13.63	13.64	15.18	16.81

The density of the specimen was determined by measuring the samples' weight and volume. An analytical digital balance (Scientech, SA210) with a precision of 0.1 mg was used to measure the weight. Archimedes' principle was used to determine the sample volume. The hardness of the specimen was measured using a Vickers micro hardness tester under a load of 1 kgf for 15 seconds.

4.3.2. X-ray diffraction of $Cr_xMoNbTaVW$

XRD patterns of the premixed metal powders and the as-solidified CrxMoNbTaVW HEA samples are shown in Figure 4.4. The XRD peaks of Cr, Mo, Nb, Ta, V and W can be traced in the ball-mixed powders. However, after the arc-melting process, all the crystalline structures of the alloys are confirmed to be BCC phases, with a minor difference of the lattice constants. With increasing the Cr content from x = 0.5, 1, to 2, lattice constant of the BCC phase decreases from 0.31899 ± 0.00013 nm, 0.31826 ± 0.00049 nm to 0.31583 ± 0.00035 nm respectively. Despite the presence of elemental micro-segregation in these samples presented in section 3.3, these values agree well with the ones estimated from the mixture rule, as shown in Table 4.3. As expected, the increase of Cr content leads to the decrease of the lattice constant, which agrees with the experimental results.

Table 4.3 The experimental lattice constant *a*, Vickers hardness *HV*, density ρ of the HEA alloy and the estimated average (experimental/ estimated [48]).

	Vickers hardness, HV	ρ*, g/cm^3	*a*, nm
TiMoNbTaVW[11]	505.1 (4954 MPa)	11.7/11.19	0.3216/0.3174
MoNbTaVW [22]	535.3±28.6 (5250 MPa)	12.36/12.36	0.31832/0.31827
$Cr_{0.5}$MoNbTaVW	675.5±27.5 (6624.7±269.2 MPa)	11.5/11.4	0.31899/0.31586
$Cr_{1.0}$MoNbTaVW	704.6±17.4 (6910.3±170.5MPa)	11.4/11.1	0.31826/0.31290
$Cr_{2.0}$MoNbTaVW	754.9± 43.1 (7403.4±422.5MPa)	11.2/11.4	0.31583/0.31103

* Estimated data were calculated using equation (1).

In the XRD pattern of x=2.0, apparent secondary BCC peaks appear beside the main BCC peaks with a smaller lattice constant. This observation is supported by phase diagram calculations, Figure 4.1 and Figure 4.2. With x increasing from 0.5 to 2, the formation temperature for the secondary BCC increases. Thus, it's more likely for the secondary BCC structure to form during the arc melting process.

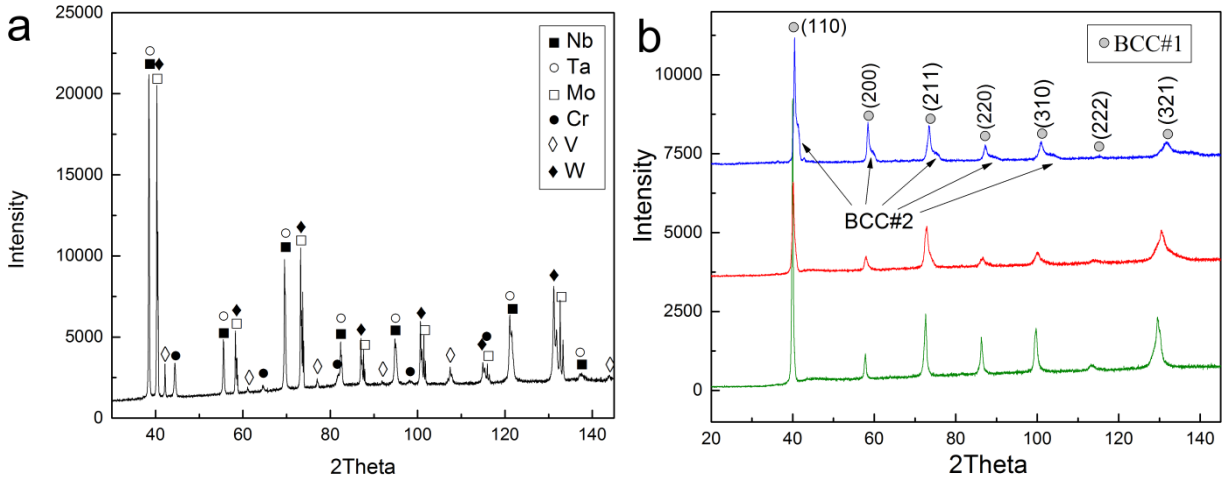

Figure 4.4 XRD patterns of (a) mixed metal powders and (b) as-solidified Cr_xMoNbTaVW alloys

4.4. Microstructures for CrxMoNbTaVW

SEM backscatter electron images were taken separately on the finely polished surfaces of $Cr_xMoNbTaVW$ (x = 0.5, 1, 2) HEA alloys. Typical solidification microstructures were observed in all samples. Figure 4.5 shows the transition from a cellular structure to a dendritic structure as the Cr content increases. It is well known that the constitutional undercooling leads to the formation of dendritic structures [49]. The increase of the Cr concentration will lead to the increase of the undercooling effects. So as shown in Figure 4.5 (a), when x=0.5, the undercooling is relatively weak, thus the cellular structure forms. With the x increases to 1.0, Figure 4.5 (b), the stronger undercooling facilitates the growth of the primary dendrite arms to around 10 μm. As x goes even larger in Figure 4.5 (c), the dendrite arms grow to around 30 μm long and the branch arms start to form.

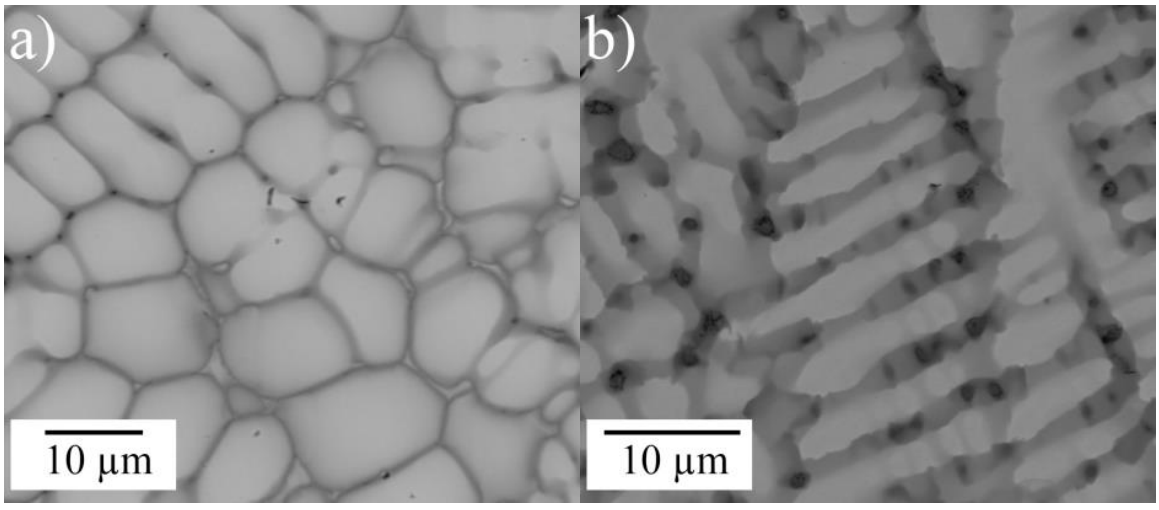

Figure 4.5 SEM backscatter electron image of the HEA $Cr_xMoNbTaVW$: (a) x=0.5, (b) x=1.0, (c) x=2.0

(Figure 4.5 cont'd)

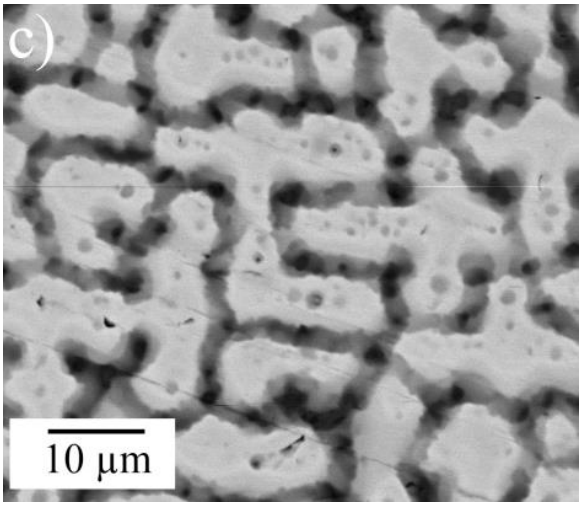

In dendritic growth, mass of low melting temperature solute is ejected between the dendrite arms and causes micro-segregation. In backscatter images (Figure 4.5), the heavier metal elements (higher atomic number Z) have a brighter color. In this case, the order of brightness is W and Ta first, followed by Mo and Nb, and Cr and V last. The micro-segregation was measured by EDS mapping, as shown in Figure 4.6, Figure 4.7 and Figure 4.8. The Mo, Ta and W elements are clearly seen inside the dendritic structures, while most of other elements can be clearly seen with enrichments in the inter-dendritic regions.

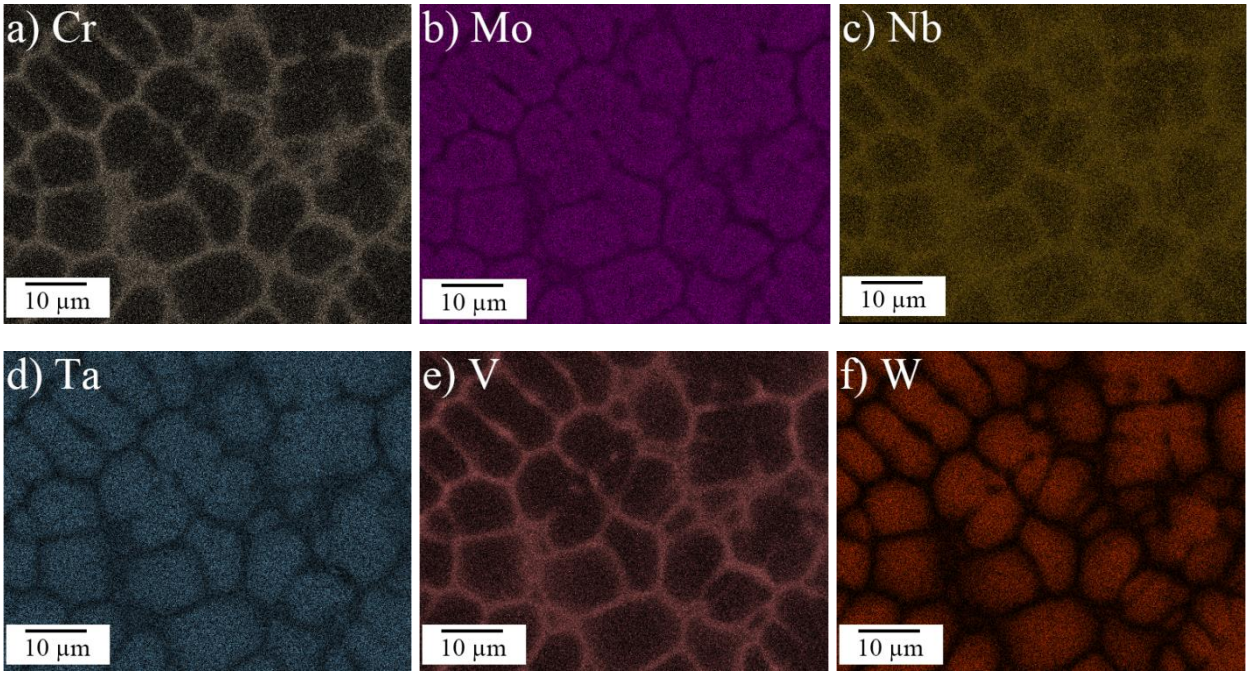

Figure 4.6 EDS mapping of the HEA $Cr_{0.5}MoNbTaVW$

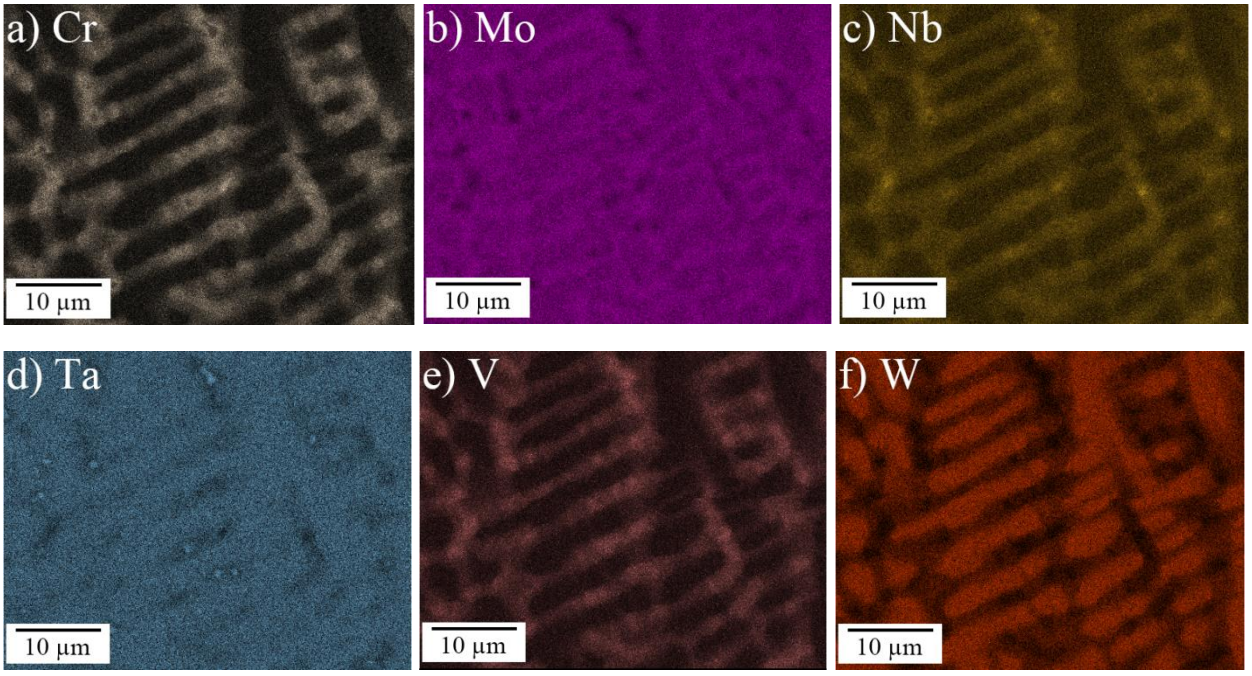

Figure 4.7 EDS mapping of the HEA $Cr_{1.0}MoNbTaVW$

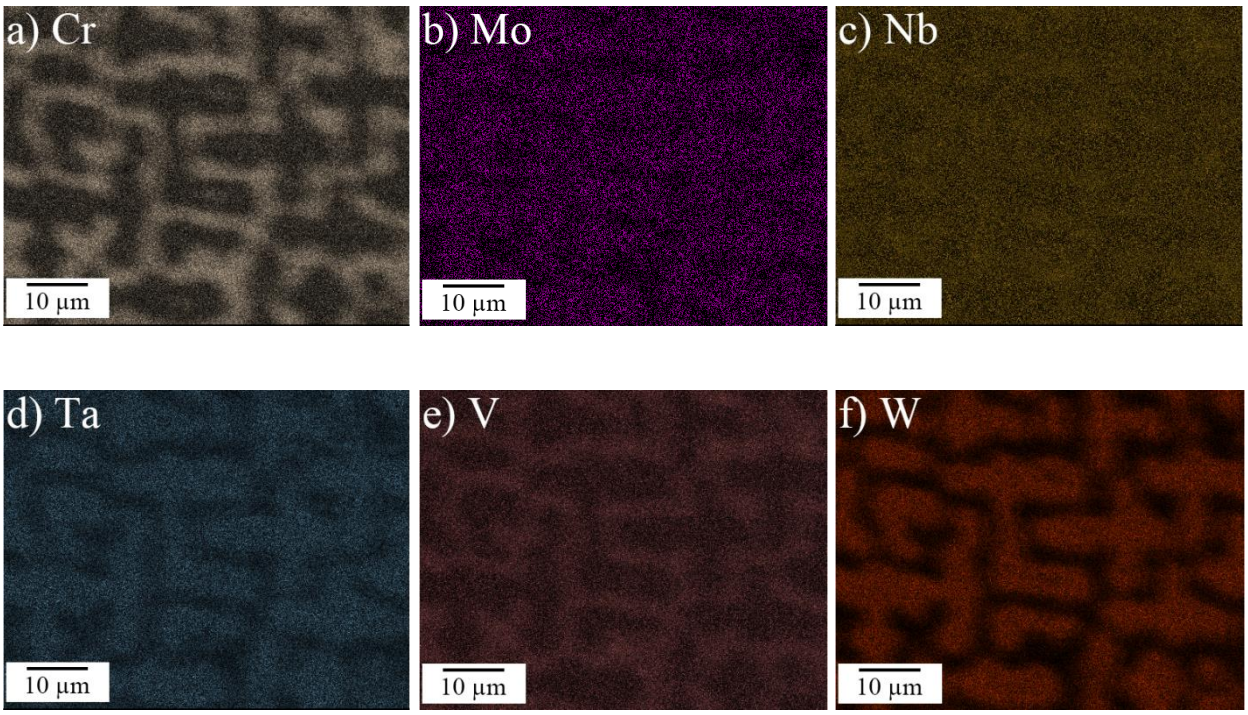

Figure 4.8 EDS mapping of the HEA $Cr_{2.0}$MoNbTaVW

The micro-segregation between the dendrite and inter-dendrite regions can be quantitatively identified through the EDS point scans. The elemental percentages of each element were taken on both dendrite areas (C_d) and inter-dendrite areas (C_{id}). Following Leo et al. [32], the partition coefficient $K = C_d/C_{id}$, was used to evaluated the micro-segregation quantitatively. It can be shown that in dendrite region of all three samples, the enriched elements are W first, followed by Mo, and then Ta, while the inter-dendrite region was enriched in Cr followed by V and then Nb. The sequence of the segregated elements qualitatively agrees with the prediction from Scheil model as shown in Figure 4.2 (c and d). For Cr_xMoNbTaVW (x≈0.5,1,2) partition coefficients, the lower end is Cr at x ≈ 0.5, with a value near 1:9, and the higher end is W at x ≈ 2.0, with a value close to 12:1, Table 4.4.

Table 4.4 Partition cofficient K of $Cr_xMoNbTaVW$ HEA

	Cr	Mo	Nb	Ta	V	W
x≈0.5	0.11(1:9)	1.60	0.50	1.14	0.17	5.50
x≈1.0	0.17	1.40	0.55	1.28	0.28	3.61
x≈2.0	0.34	4.18	0.83	1.46	0.55	11.66 (12:1)

The EDS line scan was used to quantify the level of element segregation between the dendrite arms and inter-dendritic regions. As shown in Figure 4.9, the elemental compositions were collected at points along a straight line across the dendrites and inter-dendrites with an interval separation of 0.1 μm.

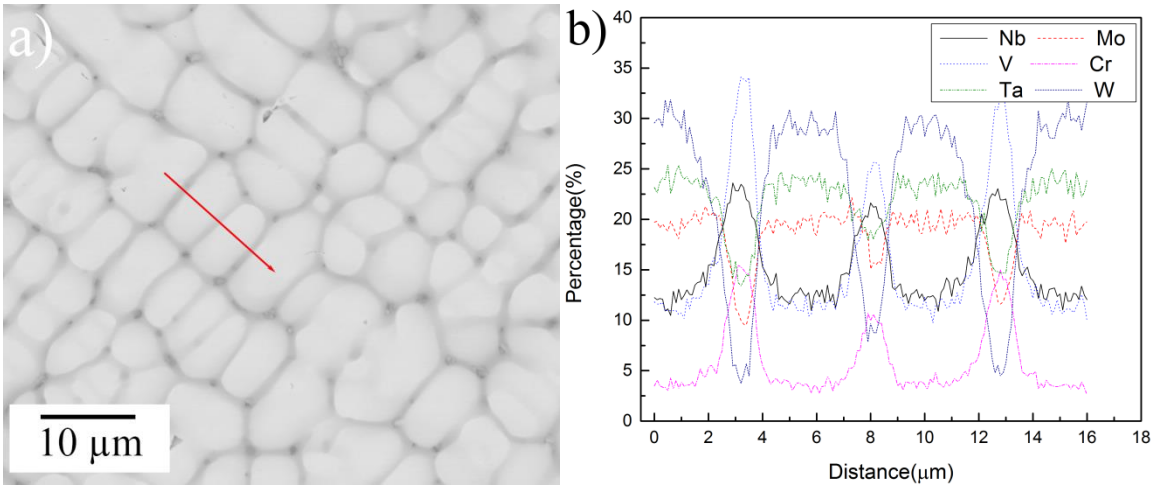

Figure 4.9 SEM image with EDS line measurement locations marked of (a) x=0.5, (c) x=1.0, (e) x=2.0, and atom percentages of (b) x=0.5, (d) x=1, (f) x=2

(Figure 4.9 cont'd)

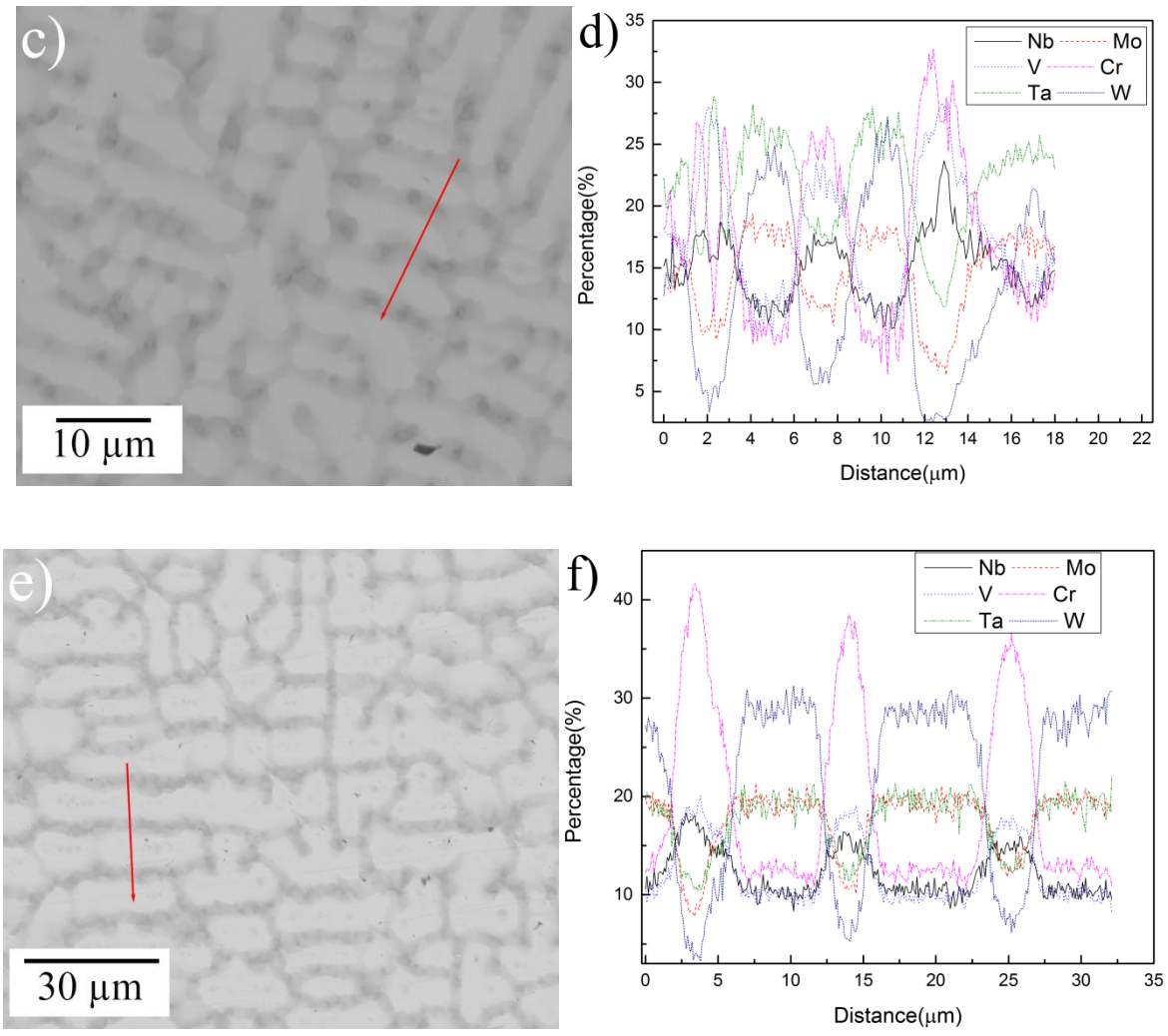

4.5. Density and hardness for CrxMoNbTaVW

The density, hardness, and lattice constant of quinary MoNbTaVW alloy, senary HEAs $Cr_xMoNbTaVW$, and TiMoNbTaVW were listed in Table 4.3 to demonstrate the effect of introducing Cr or Ti into the base alloy MoNbTaVW. The densities of the $Cr_xMoNbTaVW$ alloys were determined to be 11.5 g/cm^3 for x=0.5, 11.4 g/cm^3 for x=1.0, and 11.2 g/cm^3 for x=2.0 (see Table 4.3). To compare with the experimental results, the density of a disordered solid solution can be estimated from the rule of mixture:

$$\rho_{est} = \frac{\sum c_i A_i}{\sum \frac{c_i A_i}{\rho_i}} \quad (4\text{-}1)$$

where c_i is the atomic percentage of an element; A_i is the atomic weight; and ρ_i is the density of the pure element. The calculated theoretical densities are also listed in Table 4.3. The measured densities of the HEAs are very close to the corresponding calculated ones.

Table 4.5 The atomic radius *r* of the metal feedstock [50].

Metal	Ti	Cr	Mo	Nb	Ta	V	W
r, Å	1.46	1.28	1.40	1.47	1.47	1.35	1.41

The values of Vickers micro-hardness were measured across the polished surface of HEA samples. Five random sites were tested on each sample and the averaged values were summarized in Table 4.3. The hardness of $Cr_xMoNbTaVW$ were calculated to be 675.5 ± 27.5, 704.6 ± 17.4, and 754.9 ± 43.1 for x = 0.5, x = 1.0 and x = 2.0, respectively. The experimental micro-hardness values are dramatically higher than the hardest component W in the system. Since the Cr is the smallest element in the $Cr_xMoNbTaV$ system, Table 4.5, adding more Cr into the system is expected to increase the atomic size misfit influence which will increase the hardness. Clearly, solid solution hardening mechanism plays an important role in this HEA system. Moreover, early study on the Ti addition into base alloy MoNbTaVW shows no hardening effect [40], since the radius of Ti is similar to rest of elements in the system. The small hardness difference between TiMoNbTaVW and MoNbTaVW is due to the grain size differences.

4.6. Further discussions on CALPHAD thermodynamic analysis

It is known that the Laves phases form in Cr-Nb [22] , Cr-Ta [22], Nb-V [51], and Ta-V [22] binary systems, but the solubility of the Laves phases into the ternary systems of refractory

metals is not huge [22]. Because both CALPHAD modeling (section 2) and experimental testing (section 3) state that disordered BCC solid solutions form in the CrMoNbTaVW alloys, more thermodynamic calculations were carried out on the BCC and C15 phases as a function of temperature and compositions. Figure 4.9 compares the entropy, enthalpy and Gibbs energy of BCC and Laves phases in the senary CrMoNbTaVW alloy as a function of temperature using the default reference states (namely the stable structure at 25.15 °C and 1 atm). The BCC phase has significantly larger entropy than the C15 phase while the enthalpy is lower for the BCC phase by a small amount. The temperature dependence of entropy is presumed due to the lattice phonon vibration that strongly depends upon temperature. For quantitative evaluation of entropy sources of high-entropy alloys, please refer to recent publications [51, 52]. Note that direct comparison in the Gibbs energy between phases such as in Figure 4.10 (c), Figure 4.11(c) and Figure 4.12 (c) is most meaningful for single-phase region; for regions of co-existing phases, the tie-line is out of plane and thus the plots cannot be used for global phase equilibrium determination. Nonetheless, these plots show the trend of the Gibbs energy of each phase with respect to temperature and composition.

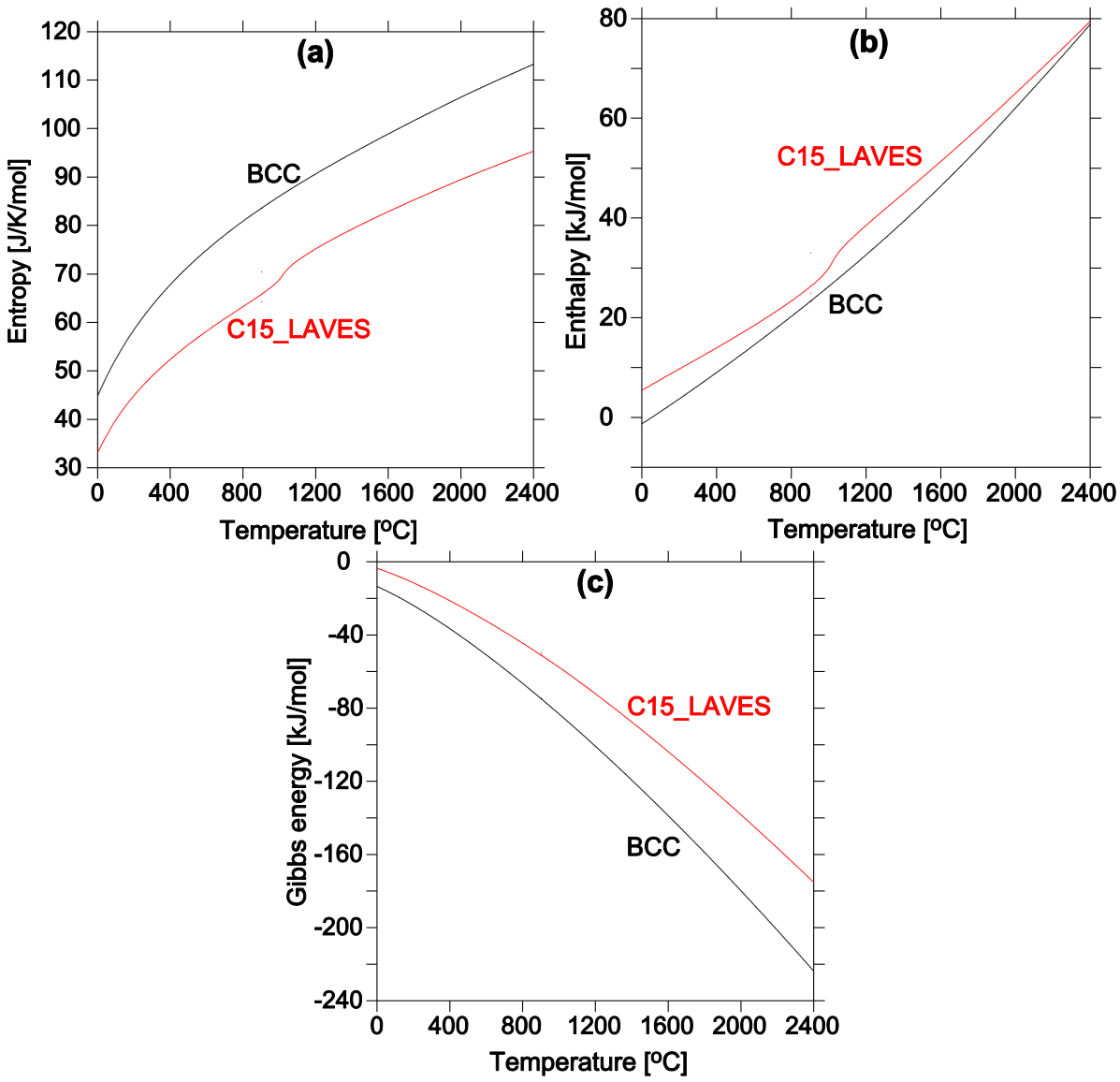

Figure 4.10 calculated (a) entropy, (b) enthalpy and (c) Gibbs energy of the BCC and C15 Laves phases in CrMoNbTaVW as a function of temperature using the default reference states (namely the stable structure at 25.15 °C and 1 atm)

The entropy of mixing (ΔS_{mix}^{bcc}) and enthalpy of mixing (ΔH_{mix}^{bcc}) for the BCC phase in CrMoNbTaVW can be calculated using the BCC phase as the reference. Below 2400 °C, they are a constant of 14.7 J/K/mol and -662.5 J/mol, respectively. That the short-range order is not considered in the BCC phase in the database is partly responsible for the constant values [52].

Future thermochemical measurements on entropy, enthalpy, and Gibbs energy for the senary CrMoNbTaVW alloy are desirable to compare with the predicted results.

Comparison in the thermodynamic mixing properties between the BCC and Laves phases in $Cr_xMoNbTaVW$ at 1000 °C is shown in Figure 4.11, which is obtained by excluding the mechanical mixing from the pure components. It is predicted that ΔS_{mix}^{bcc} reaches its maximum of +15.3 J/K/mol at 31.3 at. % Cr, which deviates substantially from the equi-molar composition. ΔS_{mix}^{C15} evolves from negative to positive values with increasing Cr contents but the absolute value is very small compared to ΔS_{mix}^{bcc}. ΔH_{mix}^{bcc} reaches its maximum of +7.3 kJ/mol at 62.3 at. % Cr while ΔH_{mix}^{C15} reaches its minimum of -8.9 kJ/mol at 42.3 at. % Cr.

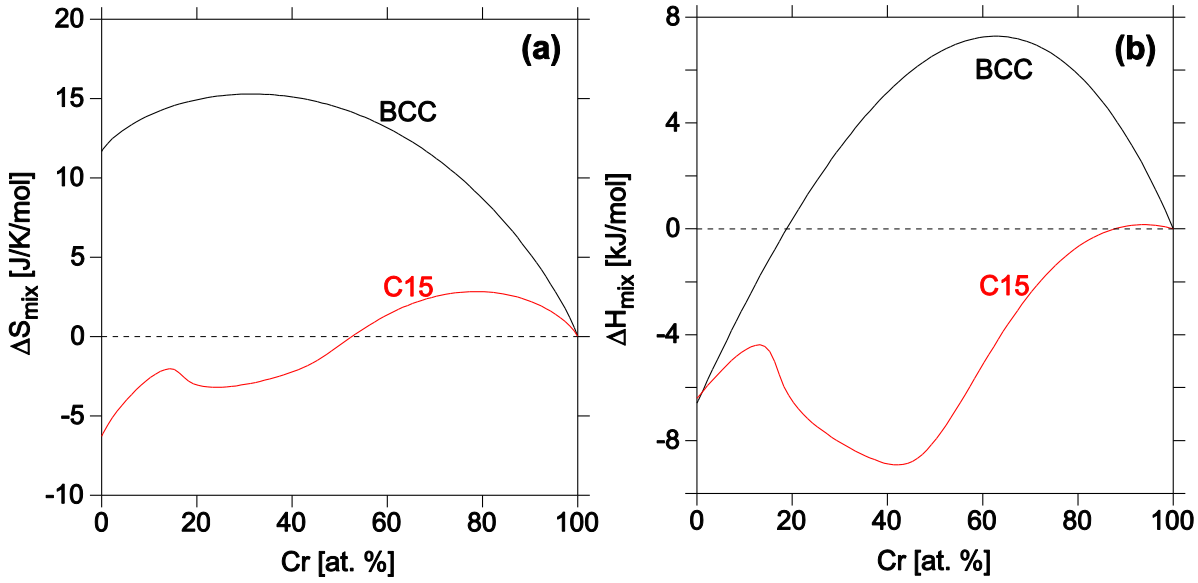

Figure 4.11 calculated (a) entropy of mixing, (b) enthalpy of mixing and (c) Gibbs energy of mixing of the BCC and C15 Laves phases in $Cr_xMoNbTaVW$ at 1000 °C as a function of Cr contents. The reference states for all components are the BCC phase at 1000 °C and 1 atm.

(Figure 4.11 cont'd)

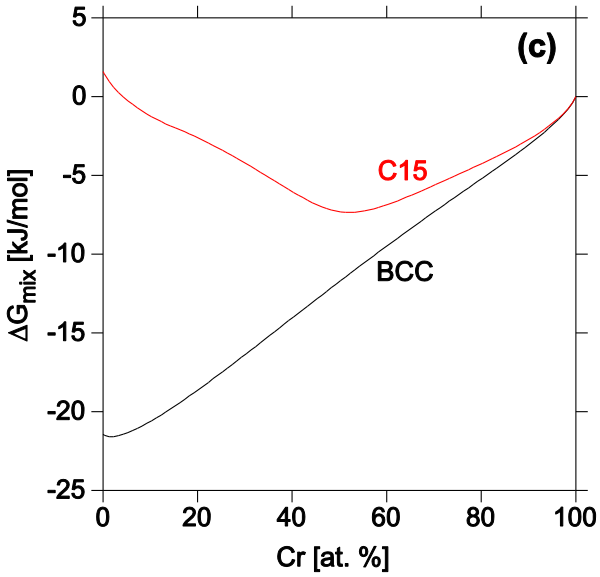

The chemical dependence of the thermodynamic mixing properties of the BCC phase is shown in Figure 4.12 for six pseudo-binaries at 1000 °C. It can be seen that variation of Cr has greater impact to the thermodynamic properties than any other elements in the Cr-Mo-Nb-Ta-V-W senary alloy system. For ΔS_{mix}^{bcc}, $CrMoNb_xTaVW$ behaves the closest to the ideal mixing followed by $CrMo_xNbTaVW$ while $Cr_xMoNbTaVW$ deviates from it the most. In terms of ΔH_{mix}^{bcc}, increasing Cr contents in $Cr_xMoNbTaVW$ increases it as reflected in a steep concave shape while for the rest systems it shows a shallow convex trend. The Cr-absent alloy (namely MoNbTaVW) has the lowest and dominating ΔH_{mix}^{bcc} and thus the lowest ΔG_{mix}^{bcc}. As a result, it is expected that addition of Cr to MoNbTaVW will result in narrower phase field in composition and temperature for the BCC phase, despite the senary CrMoNbTaVW has higher configurational entropy than the quinary MoNbTaVW, agreeing with a prior study [52].

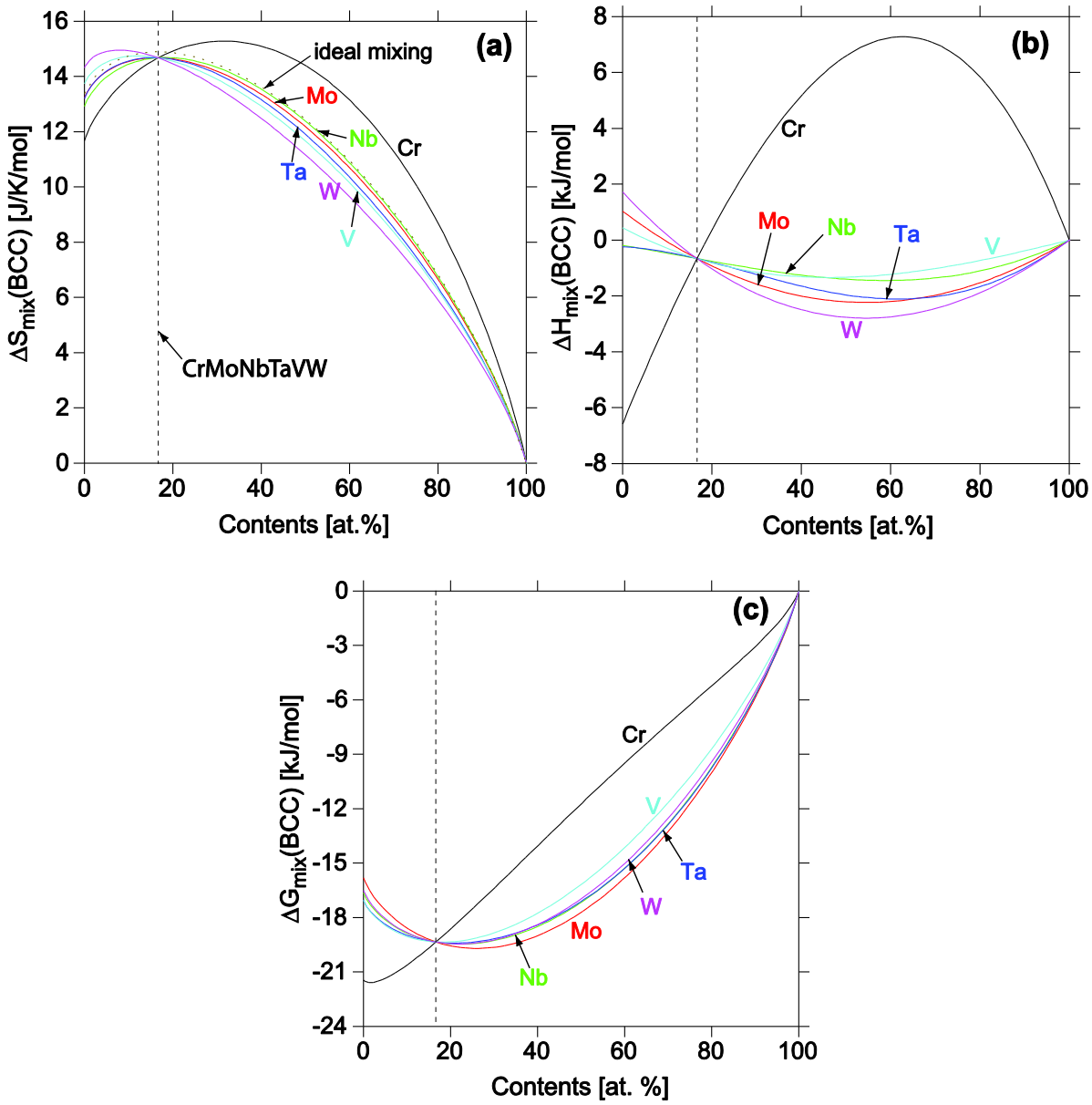

Figure 4.12 calculated (a) entropy of mixing, (b) enthalpy of mixing and (c) Gibbs energy of mixing of the BCC phase at 1000 °C in CrxMoNbTaVW, CrMoxNbTaVW, CrMoNbxTaVW, CrMoNbTaxVW, CrMoNbTaVxW, and CrMoNbTaVWx, which is labeled as Cr, Mo, Nb, Ta, V and W respectively in the plots. The reference states for all components are the BCC phase at 1000 °C and 1 atm.

4.7. Conclusions

To demonstrate the design envelope of BCC phase HEAs, a senary refractory high-entropy alloy system, $Cr_xMoNbTaVW$ (x=0.5, 1.0, 2.0), was examined using CALPHAD simulations and validated experimentally using XRD and SEM. The lattice constant, density, and Vickers' micro-hardness of this HEA alloy in the as-cast state were also measured accordingly.

For three Cr contents (x=0.5, 1.0, 2.0) in the $Cr_xMoNbTaVW$ system, all the EDS results show that the dendrite was enriched most in W and weakly by Mo and Ta while the inter-dendritic region was enriched most by Cr and V and weakly by Nb. With the increase of the Cr content, the microstructure is gradually changed from the cellular to dendritic structure. In addition, the lattice constant decreases and the Vickers' hardness increases with the Cr content grows. CALPHAD modeling predicts phase decomposition of the BCC phase for all three alloys studied at lower temperatures, and the tendency of phase decomposition increases with the increase of Cr contents. This has been confirmed by the experimental testing results, where a secondary BCC phase became detectable by XRD for $Cr_{2.0}MoNbTaVW$.

The thermodynamic analysis on the elemental dependence of the mixing thermodynamic properties (entropy, enthalpy and Gibbs energy) in BCC phase in this senary system shows that $Cr_xMoNbTaVW$ deviates from the ideal mixing the most compared to $CrMo_xNbTaVW$, $CrMoNb_xTaVW$, $CrMoNbTa_xVW$, $CrMoNbTaV_xW$ and $CrMoNbTaVW_x$. Increasing Cr contents sharply increases the enthalpy of mixing and accordingly the Gibbs energy of mixing of the BCC phase, and as a result, destabilizes the BCC phase significantly. The calculated entropy of mixing and enthalpy of mixing for CrMoNbTaVW are 14.7 J/K/mol and -662.5 J/mol respectively. The CALPHAD calculation is a valuable tool for predicting phase stability in the $Cr_xMoNbTaVW$ system and provided instructive insights to the three studied HEAs. However, due to the general

lacking of coverage for ternary and higher-order systems in the database TCNi7, experimental work should be performed to validate CALPHAD predictions on other HEA systems.

CHAPTER 5. SINGLE-PHASE STATUS AND SEGREGATION OF AS-SOLIDIFIED SEPTENARY REFRACTORY HIGH ENTROPY ALLOY

5.1. Introduction

High entropy alloys (HEAs) were originally suggested as possessing a single phase structure [53]. The high configurational entropy due to the presence of multiple elements is believed to facilitate stability of such single phase [54, 55] via an entropic reduction of the Gibbs free energy. Single phase HEAs, including CoCrFeNi [56], CoCrFeMnNi [57], NbMoTaVW [22, 58], and HfNbTaTiZr [59], are of current interest for improved mechanical properties and new functionalities [60]. Refractory HEA systems are potential candidate materials for high temperature applications [22, 58, 59].

The claim of "single-phase" status is often based on bulk X-ray diffraction (XRD) results. Alloys that appear to be single phase in standard XRD may be revealed by high-energy XRD to consist of multiple phases [61]. Phase structure is usually sensitive to the processing procedures. For example, decomposition of single phase HEAs due to heat treatment has been reported in several recent studies [62-66]. The existence of elemental segregation is common in the as-solidified refractory HEA systems. In this chapter, the details on how a complex septenary refractory HEA alloy, CrMoNbReTaVW, appear to possess a single-phase structure according to standard XRD are examined.

To understand the development of "single-phase-like" microstructure, a CALculation of PHAse Diagrams (CALPHAD) approach [67] is employed on a new septenary HEA system-CrMoNbReTaVW. Accompanying experimental materials characterization was performed through XRD, scanning electron microscopy (SEM), energy dispersive spectroscopy (EDS), electron backscatter diffraction (EBSD), and transmission electron microscopy (TEM). Rather

than a continuous variation in composition across the entire specimen, compositional segregation in as-solidified CrMoNbReTaVW HEA occurs mainly through a preferential partitioning of refractory elements W, Ta, Re and Mo into the bright regions which form during the early stage of the solidification process, and of the lower melting temperature elements Cr, Nb, and V into the dark regions which form near the end of the solidificaiton process. It is interesting that, despite the significant differences in composition in the W-Ta-Re-Mo-rich grains and the Cr-Nb-V-rich grains, as-solidified septenary CrMoNbReTaVW shows a "single-phase-like" structure according to standard XRD, such that all observed crystalline diffraction peaks can be indexed to arise from one crystal system only.

5.2. Computational calculation and prediction

CALPHAD calculations were carried out to simulate the solidification process of equi-molar CrMoNbReTaVW using the ThermoCalc software package with the TCNI8 database, which incorporates known information for all the binary phases and most ternary phases in the Cr-Mo-Nb-Re-Ta-V-W combinations. Calculations utilizing the TCNI8 database have shown good agreements with experimental observations for various refractory body-center-cubic (BCC) HEAs, such as MoNbTaTiVW [68], HfNbTaTiVZr [69], and CrMoNbTaW [70]. In this study, calculations were performed following both the equilibrium solidification scheme and the Scheil-Gulliver solidification scheme [71], modeling respectively two extreme cooling conditions—annealing-like slow solidification and quenching-like rapid solidification.

In the equilibrium simulation, solidification proceeds sufficiently slowly such that ample diffusion is allowed to take place in both the liquid and solid states. As shown in Figure 5.1(a), equilibrium solidification initiates at ~2643°C when a single BCC phase (BCC#1) starts to form. The fraction of the BCC#1 phase increases with decreasing temperature and reaches 100% at

~2333°C, when the solidification process ends. As shown in the inset of Figure 5.1(a), the BCC#1 phase starts with enrichment in refractory elements, i.e., the compositions of W, Mo, Ta, and Re are about 15-20 at.% at ~2625°C, exceeding the equi-molar composition of ~14%, with a concomitant depression of the non-refractory elements Cr and V. In the TCNI8 database, the BCC phase is treated with a two sub-lattice model, which assumes that sub-lattice one consists of corners of the cubic lattice and sub-lattice two consists of centers of the cubic lattice. When the fractions of an element in these two sub-lattices are identical, this BCC phase is determined to be a fully disordered one. By checking the elemental site fraction of both sub-lattices in the ThermoCalc simulation for the present case, the BCC#1 phase is found to be a fully disordered solid solution phase. As the temperature decreases, the compositions of the refractory elements within BCC#1 decrease continuously, and converge to the equi-molar compositions at the end of equilibrium solidification, at ~2333°C. From ~2333°C to ~1250°C, the equilibrium simulation shows the presence of one single phase, BCC#1. At ~1250°C, indications of phase separation are seen through the appearance of a second BCC phase (BCC#2), which is dominated by Cr and V (over 75 at.%). The existence of a single disordered solid solution phase of BCC#1, excluding any possible intermetallic compounds over a wide temperature range of 2333-1250°C, is indicative of the tendency for the equi-molar CrMoNbReTaVW system toward single BCC phase formation.

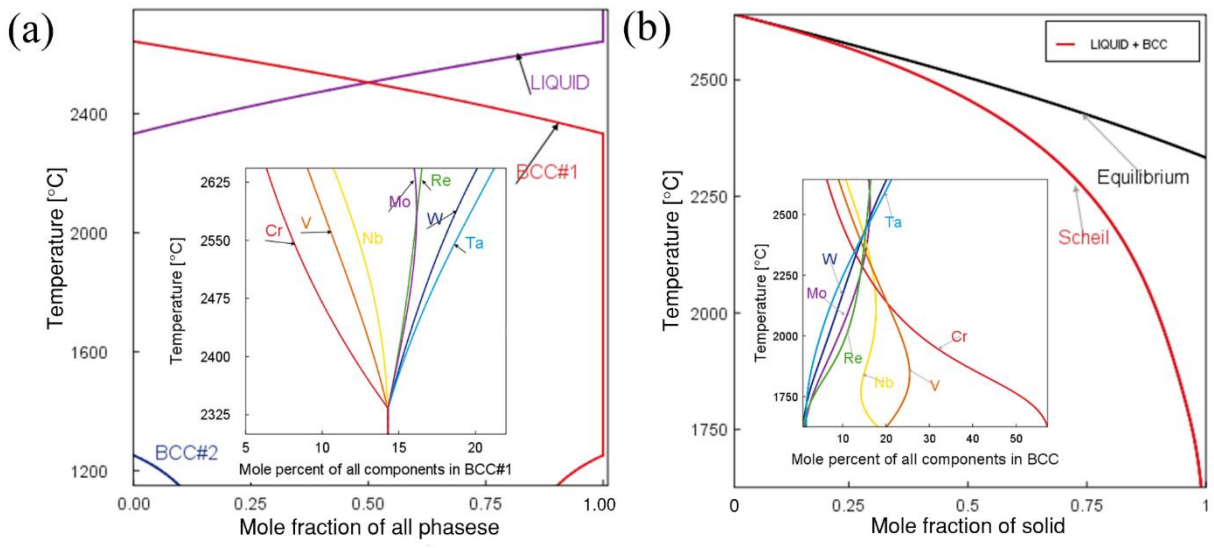

Figure 5.1 CALPHAD simulations of solidification in the CrMoNbReTaVW HEA system: (a) equilibrium solidification, (b) Scheil-Gulliver solidification.

Conditions for equilibrium are, however, often not reached in actual solidification processes, especially for systems rich in refractory elements. Therefore, the Sheil-Gulliver solidification scheme was also followed to probe the influence of extremely large cooling rate, which is closer to the experimental cooling process. Assumptions made in the Sheil-Gulliver model [71] are: (1) zero diffusion in the solid phase, and (2) an infinite diffusion rate in the liquid phase. As shown in Figure 5.1 (b), the effect of turning off solid state diffusion is significant, even though the solidification process still involves the liquid phase together with a single BCC phase. First, the solidification range is broadened: calculated liquidus and solidus temperatures are now at ~2643°C and ~1625°C respectively. Second, as shown in the inset of Figure 5.1(b) which shows compositions of the portion of the BCC phase formed at the corresponding temperature, compositional segregation in the solid phase is accentuated. Similar solid phase enrichment of Ta, W, Mo and Re occurs in the beginning of solidification, ~2643°C. At the end of solidification, ~1625°C, the solid phase shows significant depression of refractory elements, with the compositions of W, Mo, Ta, and Re approaching zero while the V and Cr compositions are

significantly enhanced, 20-60 at.%. The continuous decrease in refractory element compositions as temperature decreases, coupled with the assumption of zero solid state diffusion, suggests the possible existence of significant compositional variations in the solid BCC phase as the growth front evolves.

5.3. Results and discussions

5.3.1. Phase structure

The structure of the CrMoNbReTaVW specimen was first examined by XRD. A typical symmetrical θ-2θ diffraction pattern obtained from the polished surface of the as-solidified CrMoNbReTaVW specimen is shown in Figure 5.2. Corresponding to all observed diffraction peaks, all observed d-spacings can be indexed to a single BCC structure. Through a Nelson-Riley extrapolation of the data shown in Figure 5.2, the lattice constant *a* of this BCC structure was determined to be 0.3151nm [29]. This "single-phase-like" BCC diffraction pattern appears consistent with the CALPHAD simulations shown in Figure 5.1(a) and (b), which suggest that the equi-molar CrMoNbReTaVW HEA should be predominately single-phase BCC after solidification.

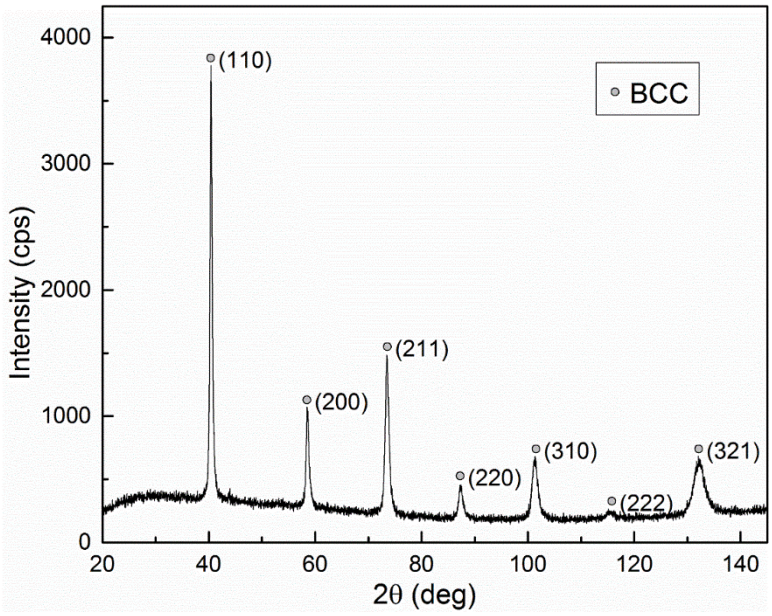

Figure 5.2 A typical θ-2θ XRD pattern obtained from the as-solidified CrMoNbReTaVW HEA specimen.

5.3.2. Microstructure and microsegregation

The actual microstructure of as-solidified CrMoNbReTaVW HEA specimen is better illustrated by the BSE image shown in Figure 5.3(a), typical of BSE images obtained from the polished specimen surface. The as-solidified microstructure resembles that associated with dendritic solidification, consisting of bright regions with branches (10-40μm in size) together with dark regions. In the BSE image, the bright and dark regions exhibit significant differences in contrast, suggesting compositional segregation. The higher brightness of the bright regions suggests enrichment of higher Z elements. To be more quantitative, EDS line scans were performed across the bright and dark regions (marked in Figure 5.3(a)), and the observed elemental compositions are plotted in Figure 5.3(b). The bright regions are enriched in refractory elements W, Ta, Re and Mo, with Cr, Nb, and V compositions below 10 at.%. The elements Cr, Nb, and V are proferentially segregated into the dark regions, where Cr compositions may exceed 20 at.%.

One notes that the bright regions are expected to form at the beginning of the solidification process at higher temperatures, whereas the dark regions are formed toward the end of the solidification process at lower temperatures. Thus, the observed enrichment of refractory elements within the bright regions and their depletion within the dark regions is consistent with the CALPHAD calculations shown in Figure 5.1(b), in accordance with the Sheil-Gulliver model prediction. Elements Cr, V and Nb are enriched in the solid toward the end of the solidification process at lower temperatures, thus are forced into the dark regions. It is also worth noting that, 1) compositional segregations appear to be reasonably abrupt, e.g., sharp rises in Cr and V compositions are observed at the boundaries between the bright regions and the neighboring dark regions; 2) variations in composition exist in individual bright regions and dark regions, e.g., the Cr compositions differ between the five dark regions shown in Figure 5.3. Additional SE imaging and EBSD inverse pole figure mapping, shown in Figure 5.3(c) and (d), indicate that both the W/Ta/Re/Mo rich bright regions and the Cr/Nb/V rich dark regions have the BCC structure. Furthermore, according to the EBSD orientation map, adjacent bright regions and dark regions are close to each other in crystal orientation.

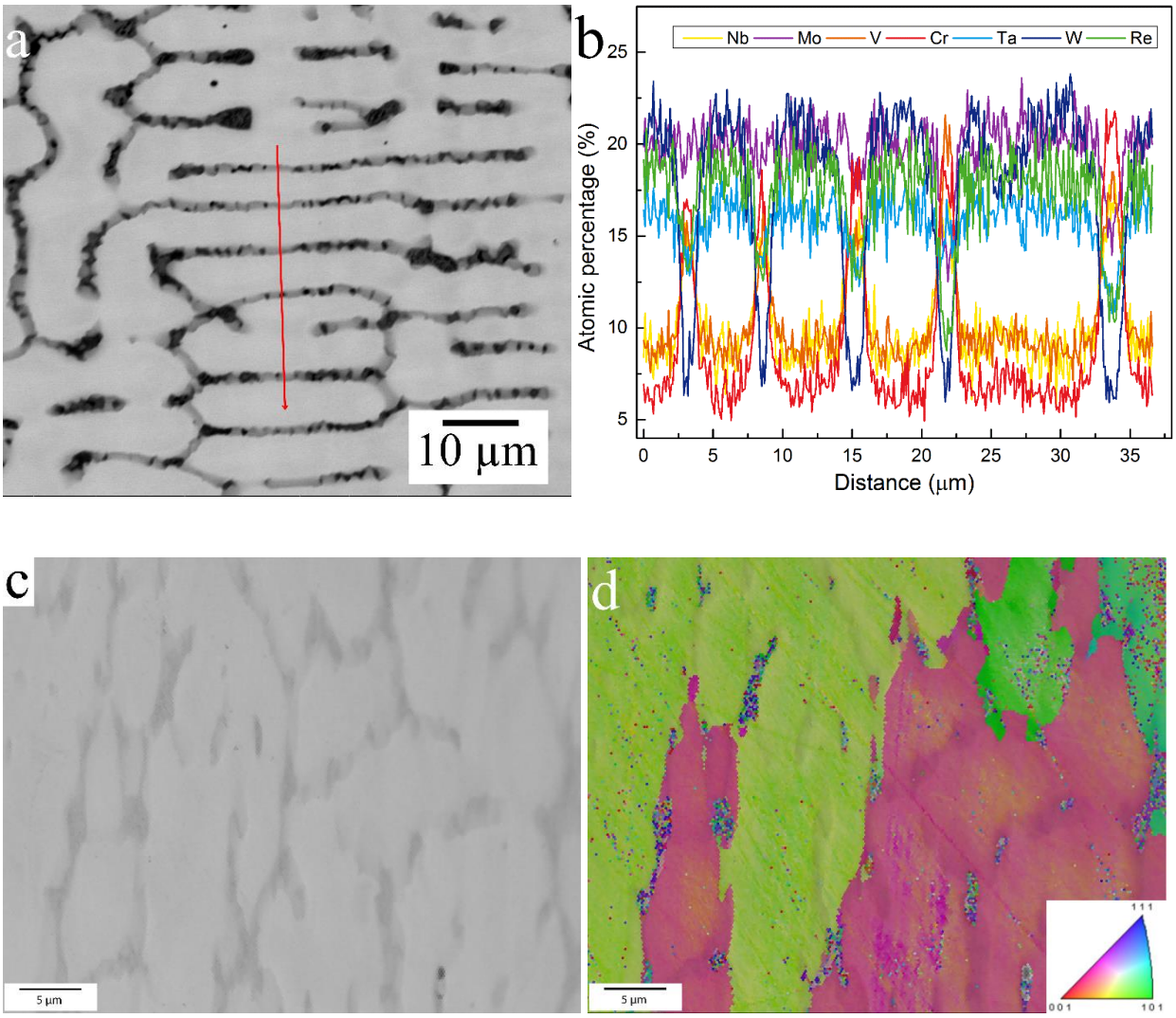

Figure 5.3 (a) BSE image of a polished cross-section of the as-solidified CrMoNbReTaVW HEA specimen, the red line marks the location of the EDS line scan measurement; (b) atomic percentages across the dendritic arms (c) SE image of the as-solidified CrMoNbReTaVW HEA at the 70° tilt needed for EBSD imaging, (d) corresponding EBSD inverse pole figure mapping on the specimen region shown in (c).

Further structural characterization was carried out with TEM. Site-selective TEM specimens were prepared via FIB to contain both the bright regions and the dark regions. In one such lifted-out lamella, as shown in Figure 5.4(a), one marked region (region 1) is a refractory-element-enriched bright region and the adjacent region (region 2) is the Cr, Nb, V enriched dark

region. Figure 5.4(b) shows a BF image taken around the interface between regions 1 and 2. The sharp boundary between regions 1 and 2 is indicative that these are two crystallographically distinct grains. Phase contrast images taken from the two grains are shown in Figure 5.4(c) and (d), which clearly demonstrate the single crystal nature of each grain. The corresponding SAD patterns are shown respectively in the insets of Figure 5.4(c) and (d), and are indexed respectively to BCC [113] and $[\bar{1}11]$ zone axis patterns. The absence of any extra diffraction spots in the diffraction patterns shown indicate the absence of any second phase precipitates with a distinct crystal structure. A definitive determination of the exact atomic arrangements responsible for the observed contrast in Figure 5.4(b) awaits additional studies in the future.

The lattice constants determined from these two SADs, by referencing a Si <110> zone axis pattern taken at nominally identical microscope settings, are 0.316nm and 0.318nm respectively. The TEM data shown in Figure 5.4 indicate that, despite the significant compositional segregation existing between bright and dark regions, the crystal structures of these two regions are both BCC. Furthermore, their lattice constants are close in value, to within 1%. Therefore, the TEM results are consistent with the XRD data shown in Figure 5.2. From the width of the BCC (110) X-ray peak shown in Figure 5.2 (FWHM = 0.353° at 40.399° 2θ), the maximum lattice constant difference within the entire specimen region sampled in the XRD measurement is ~0.0027nm, or ~1%. Moreover, based on the atomic radii of all participating elements and their corresponding atomic percentages, Figure 5.3, the averaged lattice constants are also found to have a variation of 0.0025nm, or ~1% between the bright and dark region. The results above show that, as the system attempts to minimize its overall free energy during solidification, including strain energy contributions, it arrives at a microstructure in which bright regions and dark regions with

distinctly different compositions possess the same BCC structure with very similar lattice parameters.

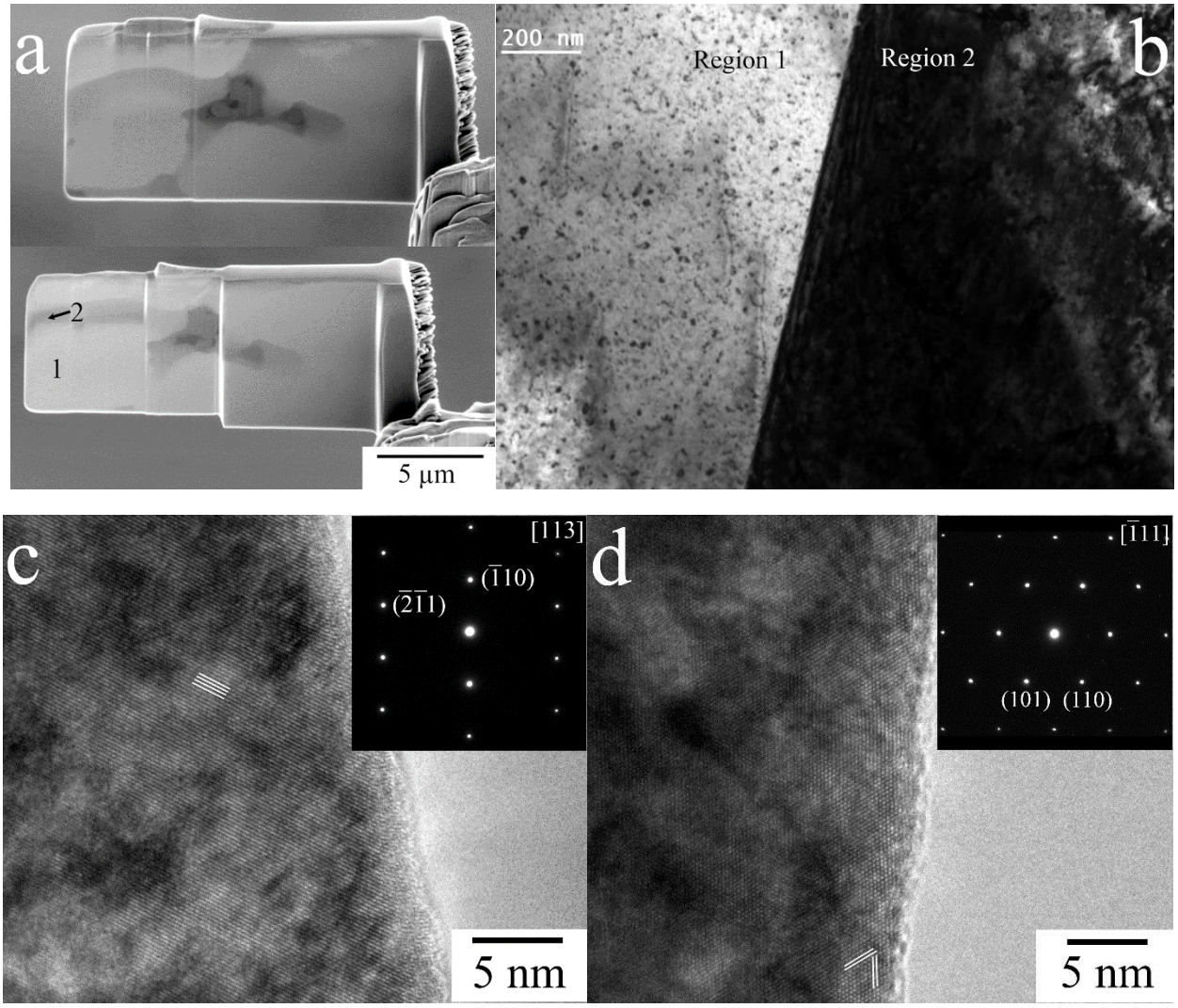

Figure 5.4 TEM characterization of the as-solidified CrMoNbReTaVW HEA: (a) SE images of the FIB lift-out before (top) and during (bottom) Ga^+ thinning; (b) a BF image of the interface between regions 1 and 2 identified in (a); (c) phase contrast image of region 1 with the associated SAD pattern shown in the inset; (d) phase contrast image of region 2 with the associated SAD pattern shown in the inset.

5.3.3. Site-selective indentation

Figure 5.5 shows the site-delective nano-indentation on both dendritic arm regions and inter-dendritic regions. As shown in Table 5.1, the W-rich dendritic arm regions show higher elastic modulus compared with the Cr-rich inter-dendritic regions, as expected, since the elements W, Ta, Re and Mo have a larger average elastic modulus than Cr, Nb and V. However, the Cr-rich inter-dendritic regions, in fact, show a larger hardness than the W-rich dendritic regions, though the average hardness of the W, Ta, Re and Mo is much higher, as shown in Table 5.2. That demonstrates the existence of lattice distortion strengthening or solid solution strengthening: the Cr has the smallest elemental radius which will cause a relative larger lattice distortion.

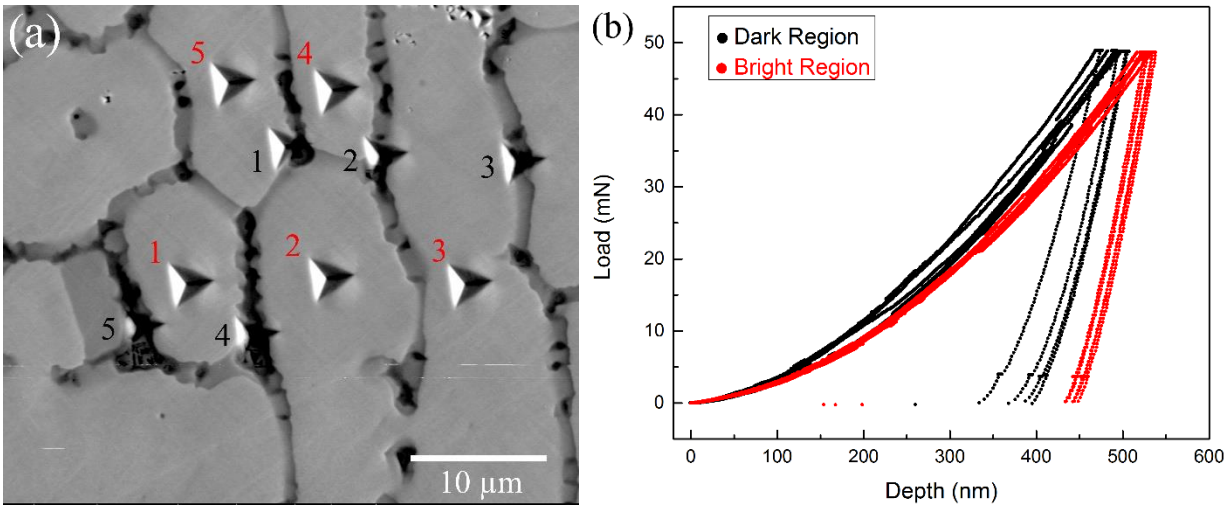

Figure 5.5 Site-selective indentation on both dendritic region and inter-dendritic region: (a) SEM images with all indentation marks and (b) the corresponding indentation curve

Table 5.1 Elastic modulus on both inter-dendritic (ID) region and dendritic (D) region.

Modulus/ GPa	1	2	3	4	5	Average
ID	320.3	318.5	323.9	304.5	300.7	314 ± 10
D	347.4	354.7	342.7	349.9	350.7	349 ± 4

Table 5.2 Hardness on both inter-dendritic (ID) region and dendritic (D) region.

Modulus/ GPa	1	2	3	4	5	Average
ID	10.6	10.6	11.5	11.0	12.9	11.3 ± 1.0
D	9.0	9.4	9.4	9.2	9.2	9.2 ± 0.2

5.3.4. Micro-compression test

The micro pillar compression test was conducted on this specimen. One cylindrical micro pillar, as shown in Figure 5.6(a) and (b) consisted almost entirely of the dendritic arm region with bright contrast, and the pillar #2 (Figure 5.6(b) and (d)) with a similar size consisted with a mixture of both dendritic arm region and inter-dendritic region with dark contrast. Compression load displacement curves obtained from the two pillars show markedly different flow stresses. That further proves that the existence of compositional segregation brings mechanical property differences within the as-cast HEA specimen.

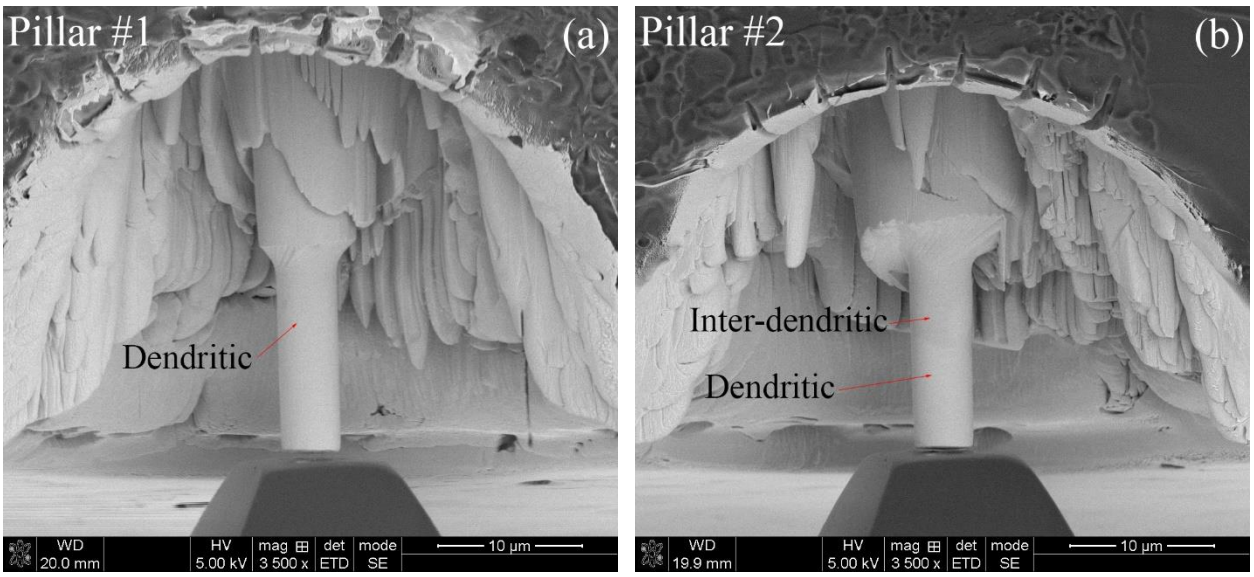

Figure 5.6 (a) The SEM image of micro pillar #1 before compression test, (b) the pillar #2 before compress test, (c) the pillar #1 after compression test, (d) the pillar #2 after compression test and (e) the compression curve of both pillars.

(Figure 5.6 cont'd)

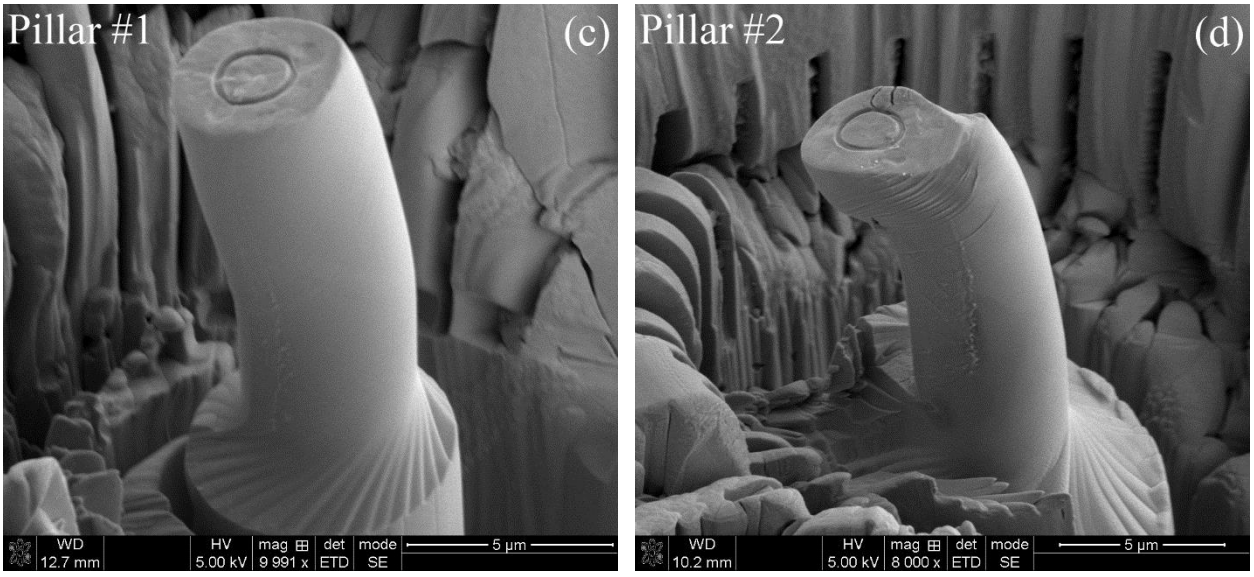
Pillar #1
(c)
WD
12.7 mm
HV
5.00 kV
mag
9 991 x
det
ETD
mode
SE
5 µm
Pillar #2
(d)
WD
10.2 mm
HV
5.00 kV
mag
8 000 x
det
ETD
mode
SE
5 µm

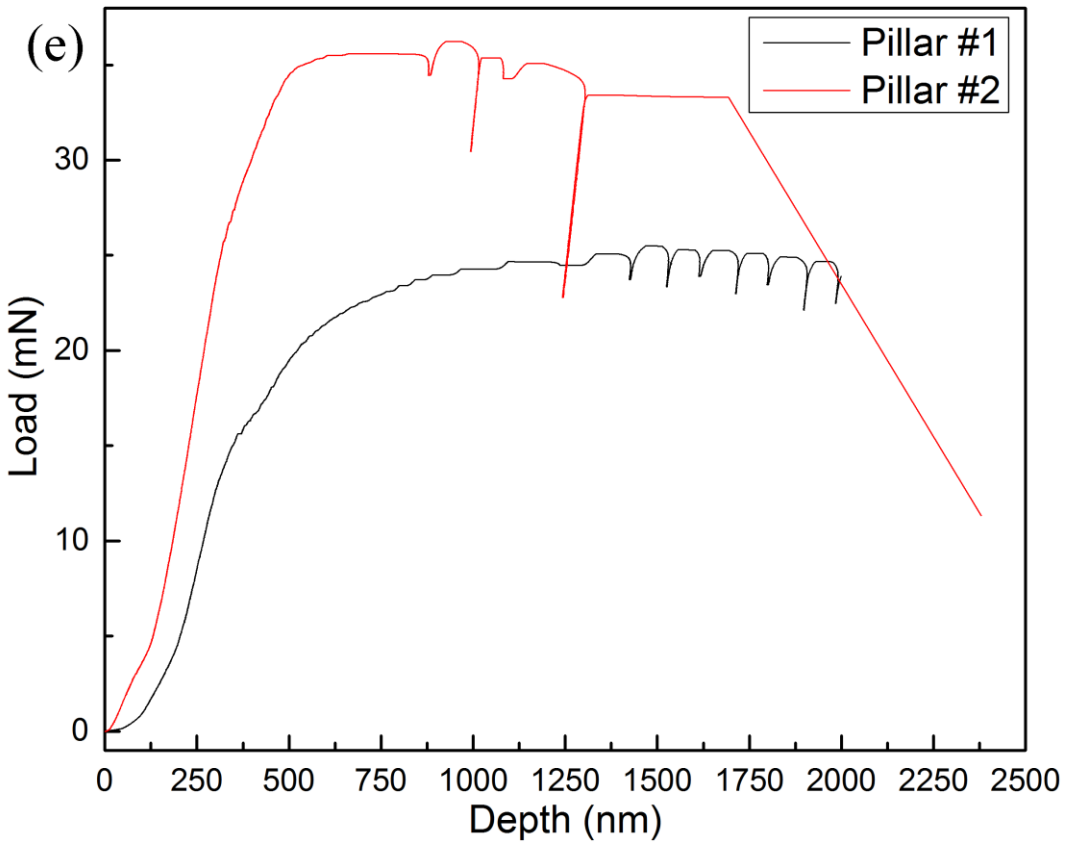
(e)
Pillar #1
Pillar #2
Load (mN)
0
10
20
30
0
250
500
750
1000
1250
1500
1750
2000
2250
2500
Depth (nm)

5.4. Conclusions

In summary, CALPHAD calculations suggest the tendency of BCC phase formation during solidification of equi-molar CrMoNbReTaVW HEA, which is confirmed by structural characterizations with XRD and TEM. The observations of significant compositional segregation between bright and dark regions, together with compositional variations from one dark region to another, suggest that the quenching-like rapid solidification, as described by the Sheil-Gulliver model, more closely describes the actual solidification process. Although XRD measurements showed "single-phase-like" diffraction patterns, clear evidence of significant compositional segregation within as-solidified CrMoNbReTaVW HEAs is obtained from BSE imaging and EDS line scans. TEM examinations show distinct grains crystallize in the same BCC structure with close lattice parameters, despite the significant compositional segregation, thus corroborating the observed "single-phase-like" XRD patterns. It is suggested that the existence of multiple grains with significant compositional segregation yet identical crystal structure and similar lattice constants may be a common feature in other elemental segregated HEA systems.

CHAPTER 6. THERMODYNAMIC STUDY OF HIGH ENTROPY ALLOY CORROSION BEHAVIOR

6.1. Introduction

In this chapter, the CALculation of PHAse Diagrams (CALPHAD) method is used to examine the corrosion behavior of CoCrFeNi based high entropy alloys. Pourbaix diagram, a thermodynamic approach, has been prevalently used to provide a basic guidance for the study of alloy's corrosion behavior by mapping out all possible stable phases of an aqueous electrochemical system [24, 25]. However, the available Pourbaix diagrams in the handbooks are predominately about pure elements. In the application of Pourbaix diagram for an alloy system, a simple superposition method is usually adopted [26]. This approach will inevitably neglect those nonlinear interactions, such as the interactions between the metallic elements in the matrix and the evolving oxide films. For a HEA system, which has multi-principle elements with similar content, the nonlinear interactions between e.g. the hydrated oxide phases and spinel phases are expected to be strong. Furthermore, the standard Pourbaix diagram is usually given under the conditions of standard temperature and pressure. For complex alloys and the applications under an elevated temperature, the simple superposition method using standard Pourbaix diagrams will not be adequate. Thermodynamic investigation of an alloy's corrosion behavior under various environments is an efficient tool for alloy design and optimization. The simulation results on the impacts of additional alloying of Cu and Al to the corrosion behavior of CoCrFeNi based HEAs demonstrated that CALPHAD method is a viable tool for the prediction of complex alloy's corrosion behaviors.

6.2. The simulation approach

Before conducting aqueous corrosion simulations, the phase stability of the high entropy alloy matrix was modeled using CALPHAD method to evaluate the potential corrosion resistant. A single-phase system without notable additional phases and compositional segregations is believed to have a good corrosion performance due to the reduction of localized galvanic corrosion. The phase stability calculations for the CoCrFeNi based high entropy alloys were carried out using the ThermoCalc software package with the TCNI8 database, which incorporates known information for all the binary phases and most ternary phases in the Co-Cr-Fe-Ni-Cu-Al combinations. Calculations utilizing the TCNI8 database have shown good agreements with experimental observations for various body-center-cubic (BCC) HEAs, such as MoNbTaTiVW [68], HfNbTaTiVZr [69], CrMoNbTaW [72] and CrMoNbReTaVW[73].

After knowing the alloys' matrix phases, the corrosion behavior was further modeled by introducing the aqueous phases and the oxides phases into the equilibrium calculations. The aqueous database AQS2 and the substances database SSUB5 were appended into the initialization process in order to model the interactions between different alloys and the NaCl solution. In AQS2 database, the comprehensive Johnson-Norton model is used to describe the H_2O phase and a completely revised HKF (Helgeson-Kirkham-Flowers [74]) model is used to describe the aqueous solution phase. The SSUB5 database contains most of the common compounds and gaseous species. In this study, both the oxides phases and the gas phases were included in the simulations, in order to model the passive oxides film and the production of hydrogen and oxygen phases during the hydrolysis reaction.

By considering the aqueous phases, together with alloy matrix phases, compound phases, secondary solid phases (oxide film) and gas phases, a Pourbaix diagram can be set up by performing equilibrium calculations under different electric potentials and hydrogen ion concentrations (pH value). For a known pH solution, such as the neutral aqueous solution, the amount of oxides could be calculated for different potential values. Although the actual potential of a metal in an electrolyte might be slightly different from its thermodynamic equilibrium value due to the kinetic processes [75] and local environmental inhomogeneity [76], thermodynamics calculations of aqueous corrosion behaviors still provide the fundamental information needed to evaluate the course and the rate of a corrosion process[77], especially for those thermodynamically controlled processes such as passivity and the breakdown of passivity.

In this chapter, calculations were first performed to predict the phase structures of the HEAs following both the equilibrium solidification scheme and the Scheil-Gulliver solidification scheme [71]. Then, the interactions between the alloy matrix structures and the aqueous solution were examined to generate the Pourbaix diagrams. Because of the available experimental data, CoCrFeNiCu and $CoCrFeNiAl_{0.5}$ were chosen to show the effect of additional alloying to the corrosion behavior of CoCrFeNi based HEAs.

6.3. Calculation and discussion

6.3.1. CoCrFeNi

It has been approved experimentally that the base CoCrFeNi HEA is a single-phase alloy with a stable FCC crystal structure [78-82]. And it has also been found that this FCC structure is thermally stable during annealing at different temperatures [66, 78, 83]. In the equilibrium simulation, the solidification process is sufficiently slow that ample diffusion is allowed to take place in both the liquid and solid states. As shown in Figure 1(a), equilibrium solidification initiates at ~1431°C when a single FCC phase starts to form. The fraction of the FCC phase increases sharply with decreasing temperature and reaches 100% at ~1426°C, where the solidification process ends. During the cooling down process, single FCC phase exists over quite a large region (1426°C-655°C) and then only at low temperatures, small amount of σ and BCC phases start to separate out. However, the cooling rate of the real casting process with a water cooling hearth is considerably large and the equilibrium state at low temperature usually can't be reached. Thus, in the as-cast lab samples, only single FCC phase exists in the CoCrFeNi HEA. Under the condition of a rapid cooling process, the quenching like solidification process can be simulated by neglecting the diffusion effect in the solid phases, described by the Scheil-Guiiliver model[71]. As shown in Figure 1(b), it confirms that only FCC phase is formed during the diffusion-free solidification, i.e. as-cast CoCrFeNi.

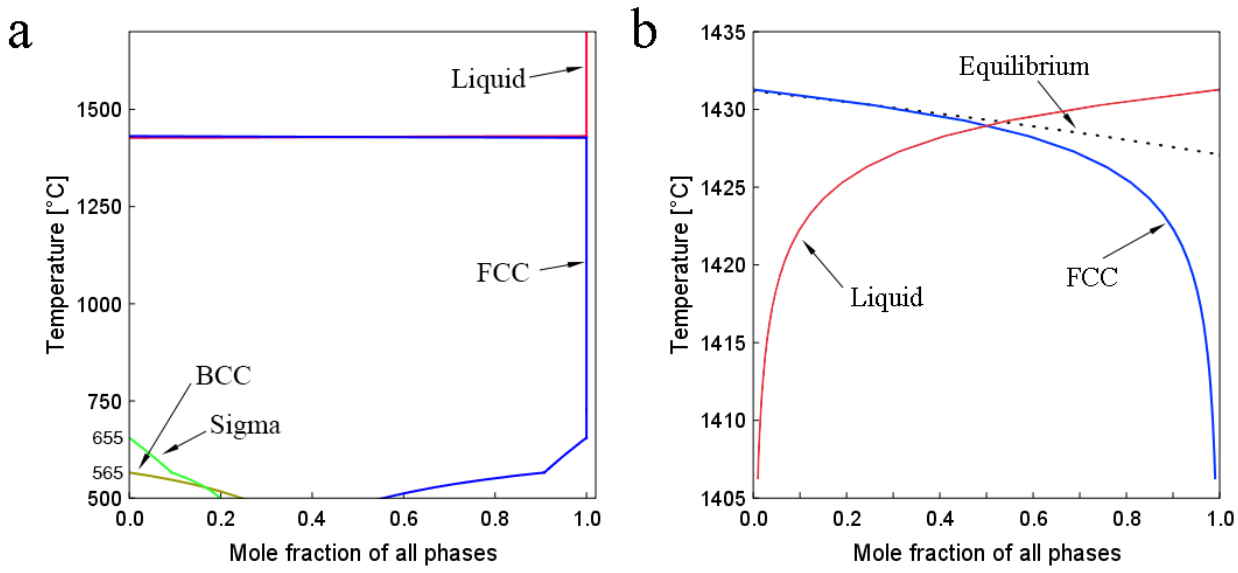

Figure 6.1 Solidification process simulations in CoCrFeNi HEA system: Equilibrium solidfication (a), Scheil-Gulliver solidfication (b)

Being an exemplary high entropy alloy, quaternay CoCrFeNi has a good corrosion resistant and has been studied extensively for many other physical and chemical properties [79, 80, 83, 84]. In order to further reveal the corrosion behavior and predict/explain the passive/corrosion working conditions, the Pourbaix diagram was calculated based on a 3.5 wt.% NaCl aqueous solution. The effective interaction ratio between the initial alloy and the aqueous is assuming to be 10^{-6}, which makes the alloy amount approaches the detectable solubility limit for cathodic corrosion protection by immunity. Figure 2 (a) shows the calculated Pourbaix diagram (pH-Eh) of CoCrFeNi. The alloy was more likely to be corroded (corrosion region) with low values of pH and potential. The AQUEOUS phase consists of all the ions in the system which implying the corrosion process. Under a higher pH value and a higher Eh, protective oxidation layers Hematite, Cr_2O_3, Co_3O_4, as well as spinel oxides $CoFe_2O_4$ and $CoCr_2O_4$ can be formed and this region is called the passivation region. In the passivation region, alloys form a relatively stable coating of oxides or some other protective solids on the surfaces. Below the corrosion region and the passivation region, the alloy

is thermodynamically stable and the metal does not corrode. The GAS phase comes from the global thermodynamic equilibrium of the solvent water that has to be considered to decide the H_2O-stability limiting lines for the Pourbaix diagram, with O_2 at the high potential, and H_2 at the low potential.

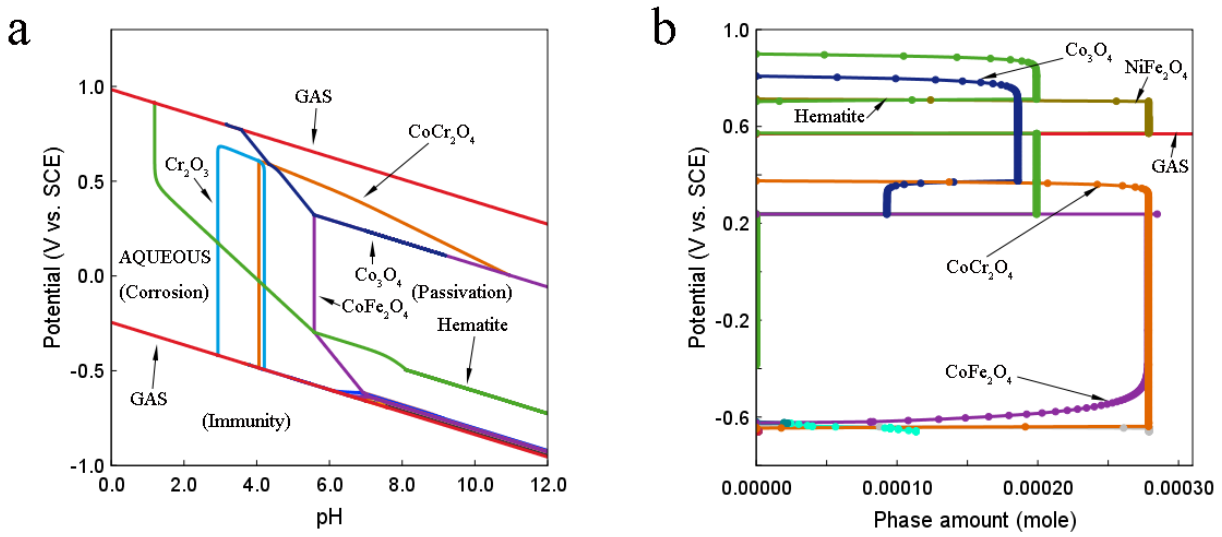

Figure 6.2 Pourbaix diagram (a) and phase property diagram under a constant pH=7.0 (b) for the heterogeneous interaction between 0.001 mole of CoCrFeNi and 1kg water (and with 3.5 wt.% NaCl), at 25 °C and 1bar.

To validate the simulations, the corrosion performance data, based on published potentiodynamic polarization experiments [85-87], are listed in Table 1. The typical three-electrode cell setup was used in those experiments with the specimen as a working electrode, together with a saturated calomel reference electrode (SCE), and a platinum counter electrode. The potentiodynamic scan was conducted from as low as -1.5V to as high as 1.5V. The results obtained from a slow scan rate ($1mVs^{-1}$) were used in this paper to approach the thermodynamic equilibrium

state in every scan step. The corrosion potentials (E_{corr}) and the pitting potentials (E_{pit}) were directly given in references [85-87], while the passive film forming potential (E_{form}) was estimated based on the published polarization curves in those references. With an increase of potential from the lowest value of -1.5V in cathodic region, the current drops rapidly because of the potential increasing. Once the oxidation film starts to form, the current start to keep stable because of the passive film setting up. The potential where the current reaches a stable level is referred to as E_{form}.

Table 6.1 Measured electrochemical potentials (Volts vs.SCE) of FeCoNiCr based high entropy alloy in 3.5% NaCl

	E_{corr}	E_{form}	E_{pit}
CoCrFeNi **[85]**	-0.26	-0.57	0.31
$CoCrFeNiCu_{0.5}$ **[85]**	-0.29	-0.57	0.09
CoCrFeNiCu **[85]**	-0.33	-0.57	0.08
$CoCrFeNiAl_{0.5}$ (HIP) **[86]**	-0.225	NA	0.385
$CoCrFeNiAl_{0.5}$ (Annealed) **[87]**	0.04	NA	0.71

A corresponding pH value of 7.0 was chosen to simulate the phase changes along with the potential increases in aerated 3.5% NaCl solution. As shown in Figure 2 (b), the oxides $CoCr_2O_4$ and $CoFe_2O_4$ start to emerge at the potential of -0.64 to -0.62 V_{SCE}, respectively. It can be seen from the experimental measurements in Table 1 that after the oxidation films were established at -0.57 V_{SCE}, the corrosion rate was suppressed. The passivation region can be persistent until reaching the pitting potential. Within the passivation region, the corrosion current density remains a relatively low level. The pitting happened at a potential of 0.31 V_{SCE}, E_{pit}, as listed in Table 1,

where the stable pits start to form. In the phase property diagram, the stable phase of $CoCr_2O_4$ starts to decrease suddenly at 0.31 to 0.34 V_{SCE} , which is very close to E_{pit}. It is known that the $CoCr_2O_4$ phase is a well-adherent single spinel layered scale resulting in an effective inhibition of corrosion [88, 89]. The p-Type semiconductivity of $CoCr_2O_4$ phase could also prevent the diffusion of oxygen[90]. Thus, the breakdown of the passivated film $CoCr_2O_4$ is believed to be the main reason of pitting initiation for the CoCrFeNi high entropy alloy system.

6.3.2. $CoCrFeNiCu_x$

To demonstrate the impact of additional alloying to the corrosion behaviors of the CoCrFeNi base alloy, the pseudo-binary CoCrFeNi-Cu_x phase diagram was calculated with the variation of Cu ratio to show the influence of Cu on the phase stability of CoCrFeNi HEA. As shown in Figure 3(a), along with the Cu increase, the single FCC phase in CoCrFeNi starts to separate into two FCC phases. At higher Cu ratio (x>1.28), a miscibility gap in the liquid state can even be found (L#1+L#2 region). Considering the real casting process has a much larger cooling rate and the equilibrium cannot be fully reached, this liquid state miscibility gap[91] is likely to show up even at low Cu composition ratios. Experimentally, Wu et.al. observed this liquid phase miscibility gap of CoCrFeNiCu equimolar HEA system in a previous study[92], which confirms the accuracy of this calculated phase diagram. After cooling down, as shown in Figure 3(b), two FCC phases are kept in the system, FCC#1 and FCC#2. More detailed compositional analysis of this system is showed in Figure 3(c). The minority FCC phase FCC#1 is a Cu rich phase and the majority FCC phase FCC#2 is the Cu depleted phase. These results agree with the XRD analysis[85] and the SEM/TEM study[92].

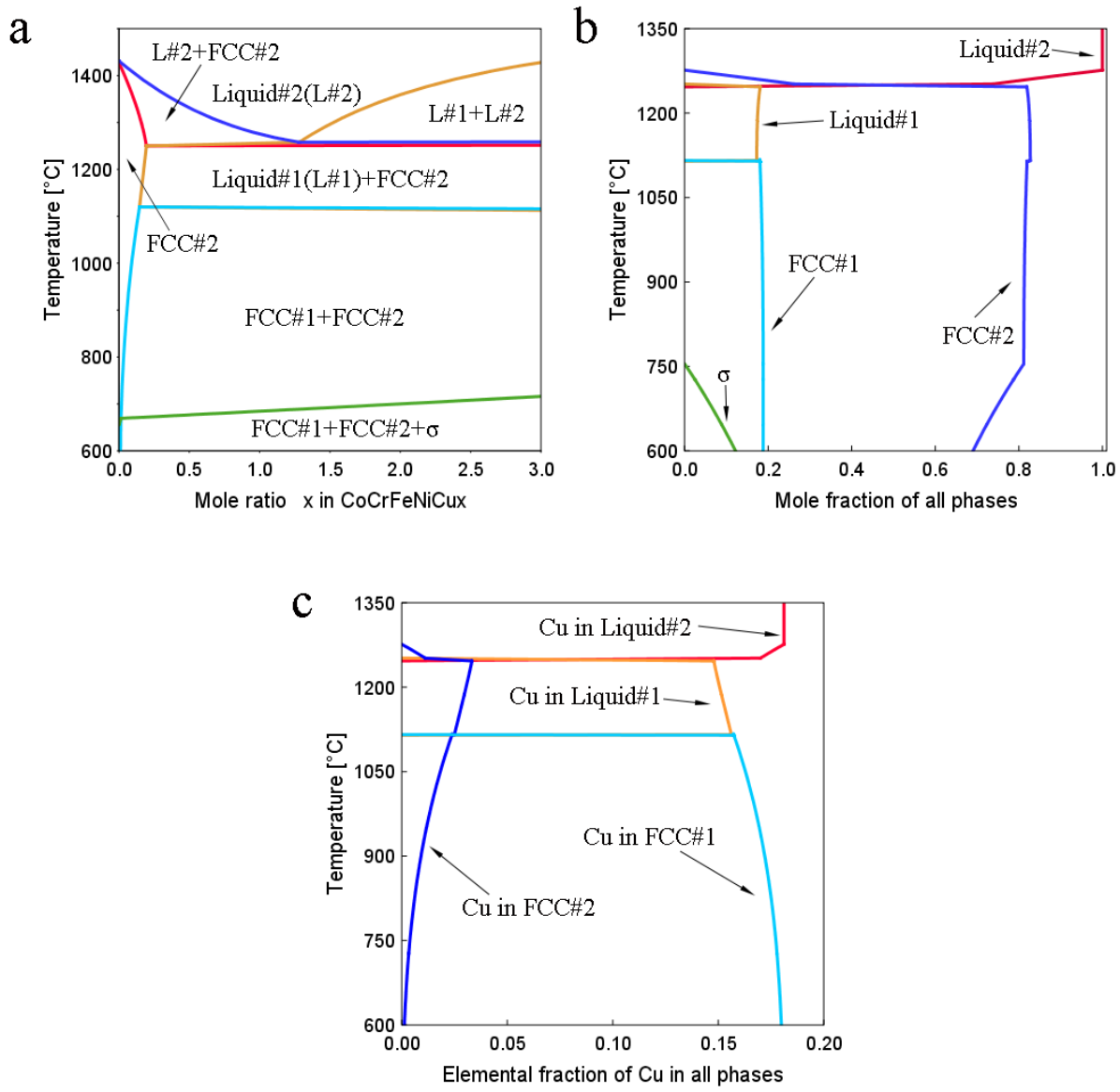

Figure 6.3 Pseudo-binary phase diagram of CrCoFeNi-Cu_x (a) , phase struacture (b) and the Cu content in all phases (c) during equilibrium soldification of CrCoFeNiCu

Comparing with the base HEA CrCoFeNi, the quinary equimolar HEA CrCoFeNiCu with Cu introduced as an additional principle element shows both new matrix alloy phases and passive oxide phases in the Pourbaix diagram. As shown in Figure 4 (a), the same phases previously shown in Figure 2(a) are plotted in dash lines and corresponding colors. It can be seen in the corrosion

region Cu can exist stably while other alloy components, i.e. Cr, Co, Fe and Ni are corroded. This indicates the existence of a galvanic action , while the Cu-rich FCC#1 phase is corroded more severely because of a stronger galvanic effect. . This galvanic corrosion has been experimentally confirmed in [85] between interdendrite and dendrite segregated phases and will lead to an accelerated corrosion damage in $CrCoFeNiCu_x$ HEA system with the increase of Cu content. Furthermore, new passive phases like $Cu_2Fe_2O_4$ are found to form on the surface of the alloy during corrosion. The thermodynamic behavior of those new passive phases would also affect the corrosion resistance of the CrCoFeNiCu HEA.

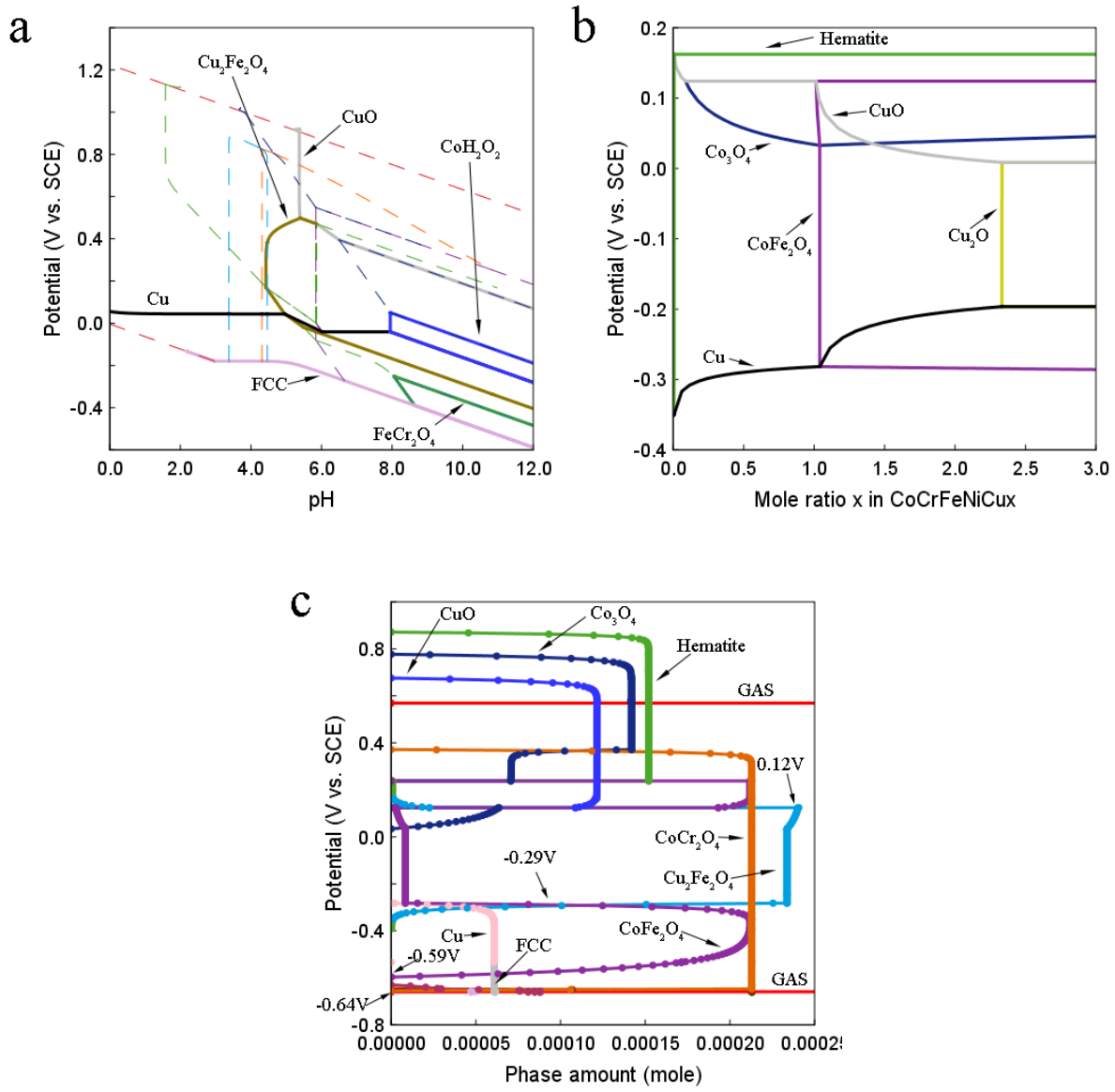

Figure 6.4 Pourbaix diagram of CrCoFeNiCu HEA system (a), under a constant pH=7.0: phase changes with Cu introducing (b) and phase properties for CrCoFeNiCu (c) for the heterogeneous interaction between 0.001 mole of CoCrFeNiCu and 1kg water (and with 3.5 wt.% NaCl), at 25 °C and 1bar.

Figure 6.4(b) Figure 4(b) shows the effect of Cu content variation under a constant pH value of 7 in the Pourbaix diagram. For $0<x<1.0$ in $CrCoFeNiCu_x$ system, no significantly influence was observed. The potentials of relevant phases are almost constant and no new phases are generated within this region. This implies the increase of Cu content has no influence on the

passive region of the alloy system for 0<x<1.0. The experimental results in Table 1 show the E_{form} as well as the E_{pit} for both $FeCoNiCrCu_{0.5}$ and FeCoNiCrCu are almost identical, indicating the same passive region. The phase properties during corrosion are shown in Figure 4(c), showing the specific passive film evolutions during the potentiodynamic process. Same as the base HEA system CoCrFeNi, along with the potential increasing, oxide films $CoCr_2O_4$ and $CoFe_2O_4$ start to show up at the potentials from -0.64 to -0.59 V_{SCE}. The experimental results reveal an identical E_{form} potential of -0.57 V_{SCE} in Table 1. The formation of $CoCr_2O_4$ and $CoFe_2O_4$ once again dramatically suppressed the corrosion progress in the quinary system. As shown in Figure 4(c), the preferentially attacking of FCC#1 matrix leaves the Cu-depleted FCC#2 phase protected until -0.29 V_{SCE}, where the initially produced $CoFe_2O_4$ is dissolved to generate the new passive film $Cu_2Fe_2O_4$. At this point, the corrosion potential is achieved, close to the measured E_{corr} -0.33 V_{SCE}. Along with the potential increasing, unlike the pitting mechanism of the CoCrFeNi system which is the breaking down of $CoCr_2O_4$ film, the pitting occurs at a lower potential of 0.12 V_{SCE}, where the secondary passive film $Cu_2Fe_2O_4$ starts dissolving. E_{pitt} measured experimentally shown in Table 1 is 0.08 for FeCoNiCrCu, which is close to the $Cu_2Fe_2O_4$ breaking down potential. Thus, the building up of passivated films $CoCr_2O_4$ and $CoFe_2O_4$ and the breakdown of the passivated film $Cu_2Fe_2O_4$ are believed to be the main mechanism of existence of the passive region. And under this corrosion potential, $CoFe_2O_4$ is replaced by the new $Cu_2Fe_2O_4$ film.

6.3.3. $CoCrFeNiAl_x$

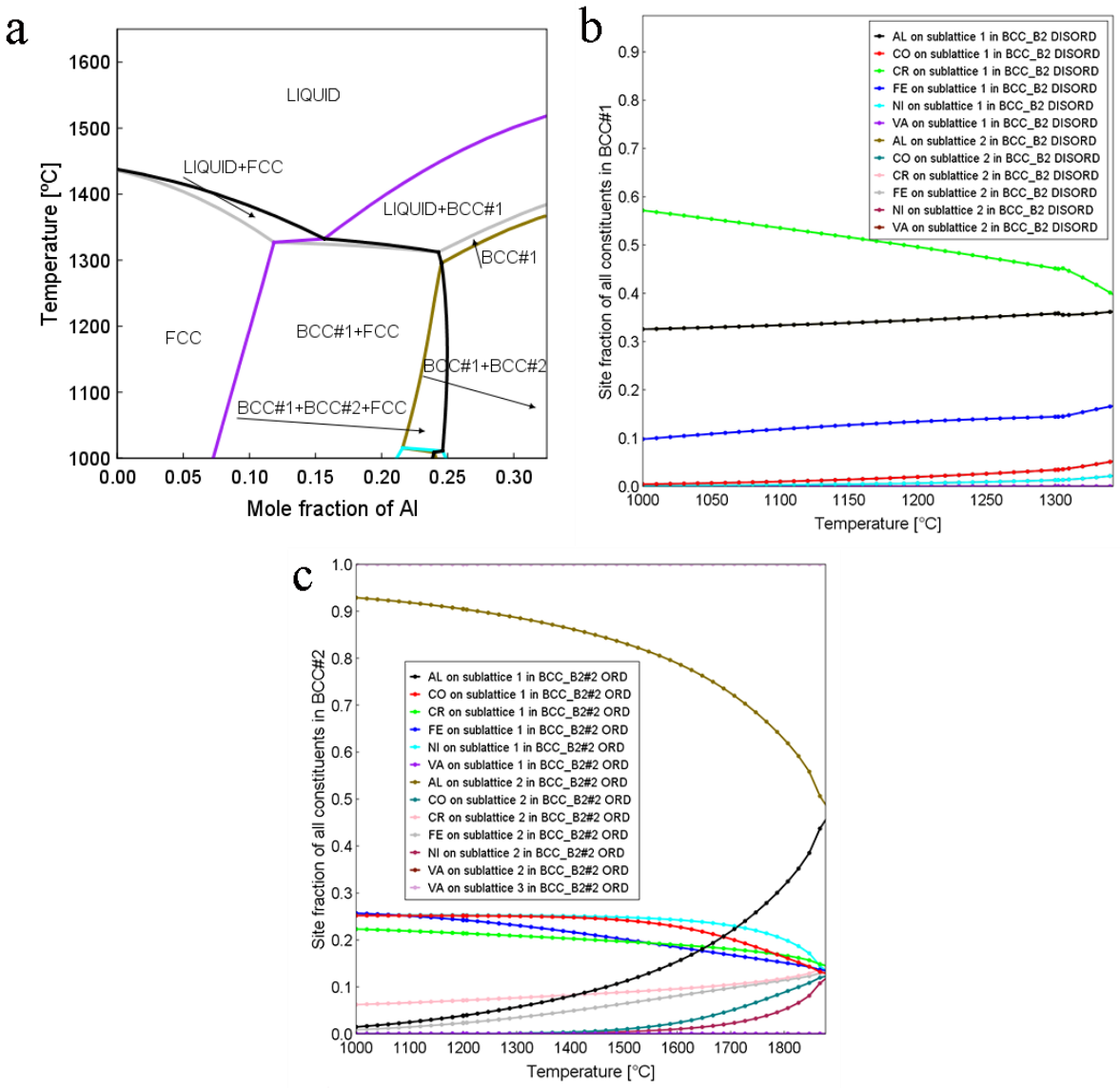

Figure 6.5 Pseudo-binary phase diagram of CrCoFeNi-Al_x (a) , sub-lattices 1 and 2 compositions of BCC#1(b), and BCC#2 (c) when x=~1.7

Introducing Al into the CoCrFeNi base is in the original HEA designs[53, 93]. As shown in Figure 6.5(a), at low Al content, including Al-free system, only FCC phase was observed at given temperature range. While, along with the Al increasing, BCC phase start to show up, then spinodal decomposition happens and the BCC decomposed into BCC#1 and BCC#2 phase. At a high Al content, the FCC phase disappeared. Taking Al mole fraction of 0.3 (x=~1.7), where the

BCC miscibility gap exists, to further analysis the structure of BCC phases. The sub-lattice model for both BCC#1 and BCC#2 were used to calculate the order properties of these two phases. Sub-lattice model assumed two interpenetrating simple cubic sub-lattices, one consistsing atoms at BCC unit's corners and the other one consisting the atoms at the centers. The site fractions of all five elements for both two sub-lattices are calculated. Like what Figure 6.5(b) shows, the compositions of each component in sub-lattice#1 and sub-lattice#2 are overlapped together, indicating the BCC#1 is disordered BCC phase. That's because in disordered state, every site can be occupied by an atom of any type, thus the probability for a given site containing an atom of a given type is equal to the probabilities for the other sites. In contrast, Figure 6.5(c) shows all five components in BCC#2 have different site fractions in sub-lattice#1 and sub-lattice#2, implying the ordered BCC structure. This is due to the ordered state has certain atoms at certain spatial positions, thus the hypothetically divided sub-lattices #1 and sub-lattice#2 will be occupied by two different combinations of elements.

It has been experimentally observed FCC phase Al counterintuitively served as BCC stabilizer: increasing Al content makes the phase structure varying from single FCC phase into FCC+BCC phase and to BCC phase. Yeh et. al. intensively studied the phase structure of $CoCrFeNiAl_x$ HEA using XRD, SEM, TEM and corresponding selected area diffraction analysis. The alloy shows single FCC structure when $0<x<0.5$, and a BCC structure appeared in addition to FCC as x exceeded 0.8. After $x>1.3$, the BCC structure decomposed of ordered and disordered BCC phases and FCC phases faded away[53]. Therefore, the experiment agrees with calculation results of the phase structure prediction of the $Al_xCoCrFeNi$ HEA system.

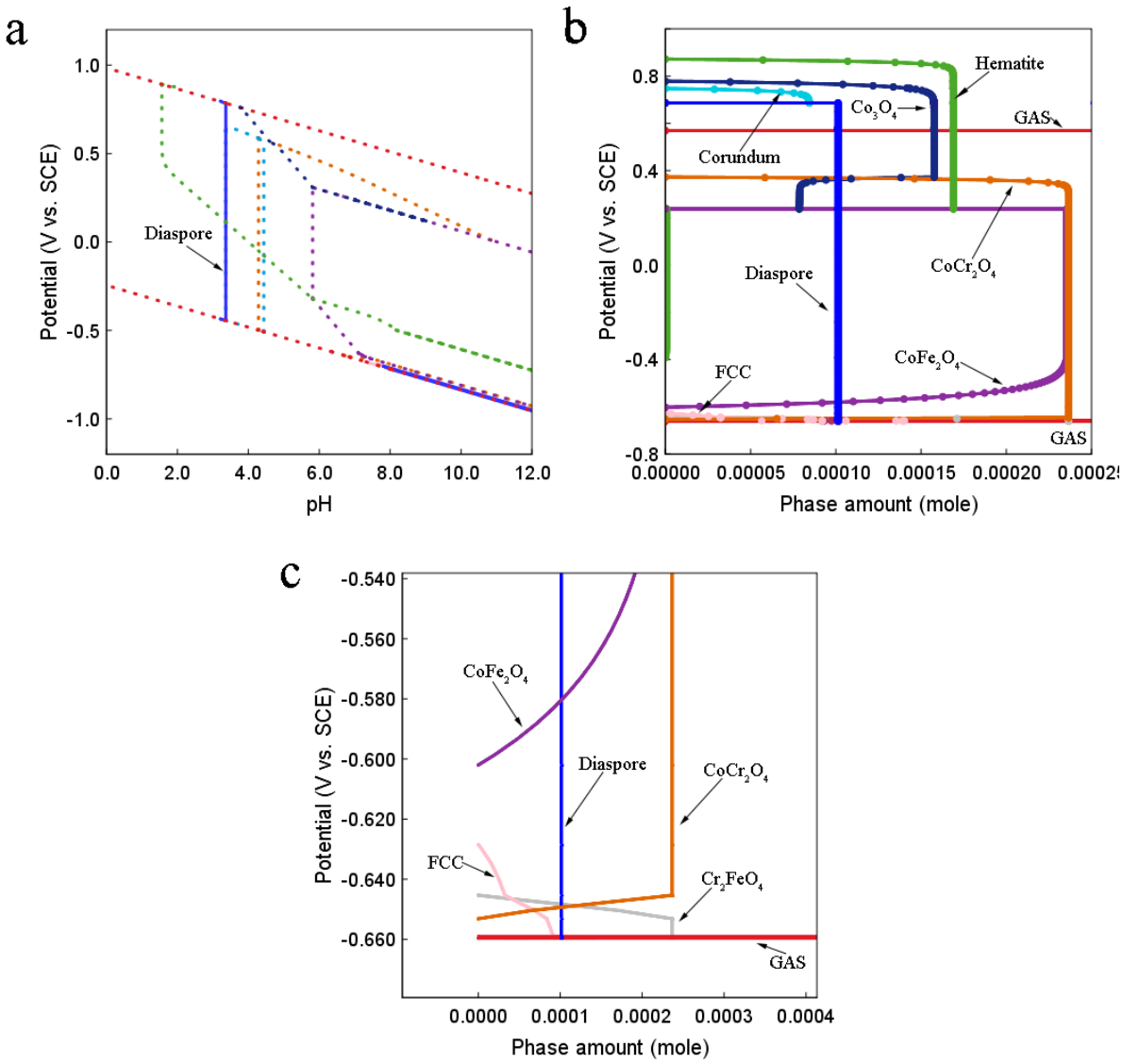

Figure 6.6 Pourbaix diagram of $CrCoFeNiAl_{0.5}$ HEA system (a) and phase properties for $CrCoFeNiAl_{0.5}$ under a constant pH=7.0 (b) with a zoom in view of the interested region (c) for the heterogeneous interaction between 0.001 mole of $CoCrFeNiAl_{0.5}$ and 1kg water (and with 3.5 wt.% NaCl), at 25 °C and 1bar.

In order to compare with the currently available experiment results [80, 86], x=0.5 was selected to furture simulated the corrosion behavior. The Pourbaix diagram of $CrCoFeNiAl_{0.5}$ is showed in Figure 6.6(a). During the corrosion process in entire pH and potentional range, the passive oxidation film phases are almost the same with the based CrCoFeNi HEA. Dash line shows

the same passive phases, labeled with same colors. Introduing Al only brings in one more phase: the diaspore phase, or α-AlO(OH). It can be seen that the diaspore phases appear from a low pH value and exist in the whole passivation region. Since the diaspore phase only contains octahedrally coordinated Al atoms, which are extremely stable and inert, this new passive film phase suggestes the improved passivity. Diaspore could also dehydrates directly to corundum (α-Al_2O_3) without destructtion of the external form of crystal and maintaining the same fundamental sturcture[94]. Whereas the oxide fim grown on pure Al is known to be γ-Al_2O_3 or boehmite (γ-AlO(OH)), which are defect version of a cubic spinel structure with close packed oxygen and alumin ions distributed in octahedral and tetrahedral positions[95, 96]. The Pourbaix diagram indicats the advantage of alloying Al into the HEA base CrCoFeNi.

Figure 6.6(b) and (c) shows the oxide phases amount evolvement during the potential increasing at a constant pH equals 7.0 at the whole calculation range and the enlarged region. The diaspore phase is formed spontaneously at the beginning of the corrosion, unlike the cases in CrCoFeNi and CrCuFeNiCu in which only Cr_2FeO_4 and $CoFe_2O_4$ graduatly grow in the active to passive transion region. Although Cr_2FeO_4 can be found for all three cases, the oxide layer of Cr_2FeO_4 usually formed as nano-scale particles which is porous and easily re-ordered than the thin diaspore passive film[97, 98]. It was confirmed experimently by the potentiodynamic polarization curves in [86] and [80] showing no active-to-passive transition region. Thus the curve reaches E_{corr} rapidly, without distinct E_{form}, as shown in Table 6.1. As the potential increasing, the Cr_2FeO_4 and $CoFe_2O_4$ failed first at 0.24-0.35 V_{SCE}, and then diaspore at 0.69 V_{SCE}. The experimental studies shows two different set of results, as shown in Table 1. [86] shows the pitting occurred in 0.385 V_{SCE} while [80] shows a pitting potential of 0.71 V_{SCE}, although the hot-isostatic-pressing specimence and the annealed specimence have similar phase structure in XRD and elementl

distribution in EDS. The reason why different pitting potentials were recorded is coming from the two type of pitting behavior in this HEA system: the failing of Cr_2FeO_4 and $CoFe_2O_4$ or the failing of diaspore and corundum. In experimental accelerated test, the scan rate, potential range, localized dissolution and surface morphology could cause metasable pittings[99]. If a continuous passive diaspore film failed to establish and cover the whole surface, the relativly inferior oxide Cr_2FeO_4 and $CoFe_2O_4$ which reach their stable pitting potential first will dominate the pitting. Therefore, in order to get a wider passive region, a slow scan rate especially in the beginning of the test is recommened according to the calculation results.

6.4. Conclusions

Using thermodynamically based CALPHAD simulations, the matrix phase structure and the aqueous corrosion behavior of the high entropy alloy system were predicted. First, during the casting, the annealing-like and quenching-like solidification can be modeled. In addition, the corrosion region, the passivation region, and the immunity region along with the Eh and pH variations for high entropy alloy during aqueous corrosion can be determined through the Pourbaix diagram. Further,the corrosion behavior under a specific environment at a nearly constant pH value has been calculated. By comparing CALPHAD simulations and previously published experimental results, the corrosion behavior of CoCrFeNi based high entropy alloys were analyzed:

1. The setting up and failing of the passive film Cr_2FeO_4 and $CoFe_2O_4$ is the main mechanism which cause the passivation and pitting in single FCC quaternary CoCrFeNi HEA.
2. In CoCrFeNiCu HEA system, the galvanic cell caused by the secondary Cu-rich FCC phase aggravated the corrosion process and the failure of $Cu_2Fe_2O_4$ also reduced the

passive region so alloying Cu is a drawback on the corrosion resistance of the CoCrFeNi HEA system.

3. Introducing Al eliminated the active to passive transition region and enlarged the passive region by bringing in α-AlO(OH)/ α-Al_2O_3 in whole corrosion process. However, if a continuous α-AlO(OH) film wasn't able to stablize and cover the whole surface, the passive region will be susceptible, but still better than Al free CoCrFeNi HEA.

In summary, the good agreements between CALPHAD simulations and experimental results on HEA system indicate that thermodynamic phase calculation is reliably to guide the design of specific alloy with superior corrosion resistant.

CHAPTER 7 OVERALL ACHIEVEMENTS AND SUGGESTIONS OF FUTURE WORK

The most significant outcome of this dissertation is the development of an efficient methodology for the high entropy alloy design, in particularly, for the design of new refractory high entropy alloys of single phase. Based on the CALPHAD method, the phase stability during equilibrium solidification as well as the Scheil-Gulliver solidification process could be modeled. The CALPHAD simulations accelerate the screening process of new single phase high entropy alloy compared with the traditional empirical prediction. After a large extensive screening, three new BCC phase and one HCP phase high entropy alloys in as-case state were identified and subsequently verified experimentally.

The single-phase status and segregation of the refractory high entropy alloys were then investigated. Although a new septenary refractory high entropy alloy was designed to be a "single-phase-like" BCC structure, the tendency of compositional segregation was identified. The site selective TEM assisted with Focused Ion Beam (FIB) was used to reveal the essence of the single-phase structure in refractory high entropy alloys: multiple grains with significantly different compositions yet the same crystal structure and the similar lattice parameters.

In order to utilize the newly designed high entropy alloys in practical industrial applications, the corrosion behaviors of HEAs were explored using CALPHAD simulations. Although a number of potentiodynamic polarization studies have been conducted experimentally, the mechanism of the passivation effect is still unclear. By using CALPHAD method, calculated Pourbaix diagrams and corrosion layer evolutions were set up. The oxidation layer pitting and forming potential were predicted and compared favorably with the test results found in the literatures. Using this approach, corrosion resistant alloy compositions could be evaluated easily.

As most of the HEAs are designed for high temperature applications, the suggestions of future work are to further explore the properties of HEAs at elevated temperatures, including the mechanical properties, corrosion resistance and oxidation resistance for those newly designed HEAs and to use the feedbacks to optimize the alloy design. The corrosion and oxidation behavior could be firstly studied by using the thermodynamic model and then tested experimentally. In addition to the casting process, 3D printing techniques have posed challenging problems related to modern alloy manufacturing. The nonequilibrium phase structure during the 3D printing process is unique. In light of this, the ultimate goal of my future research is two-fold. One is to further develop new alloy systems for high temperature applications. The other is to study the in-situ phase structure evolution during the cooling process of the molten alloys, so that the phase stability as well as the residual stress could be obtained. This information could be used in establish the unknown phase diagrams experimentally. In what follows, I will briefly elaborate my strategies to achieve this goal.

7.1. The development of oxidation and high temperature corrosion resistant alloys

High entropy alloys and refractory alloys are expected to be utilized under extreme operating conditions, thus are required to be able to resist oxidation or high temperature corrosion impact. Beside the corrosion model proposed in my previous research, the oxidation and the hot corrosion model will be also developed in order to predict the oxidation layer structure which is the decisive factor of the high temperature corrosion resistance. The designed alloys will be experimentally investigated to verify the CALPHAD model. The outcome will be robust and economic high temperature alloys.

7.2. In-situ phase structure characterization and calculation

In the last year of my PhD study, I worked on constructing of an in-situ synchrotron micro X-ray diffraction testing rig for laser melting/heating and cooling process by utilizing the synchrotron beamline of Center for Advanced Microstructures and Devices (CAMD) at LSU. The phase evolution during 3D printing and other heat/cooling conditions could be studied in real time. The collected data could be used to construct new phase diagrams as well as to assist the CALPHAD database development. More in-situ phase structure evaluations will be performed on HEAs.

REFERENCES

[1] B. Gludovatz, A. Hohenwarter, D. Catoor, E.H. Chang, E.P. George, R.O. Ritchie, A fracture-resistant high-entropy alloy for cryogenic applications, Science, 345 (2014) 1153-1158.

[2] Y.Y. Chen, T. Duval, U.D. Hung, J.W. Yeh, H.C. Shih, Microstructure and electrochemical properties of high entropy alloys—a comparison with type-304 stainless steel, Corrosion Science, 47 (2005) 2257-2279.

[3] Y.L. Chou, Y.C. Wang, J.W. Yeh, H.C. Shih, Pitting corrosion of the high-entropy alloy Co1.5CrFeNi1.5Ti0.5Mo0.1 in chloride-containing sulphate solutions, Corrosion Science, 52 (2010) 3481-3491.

[4] M.G. Shizhong Yang, Shengmin Guo, Oxidation behavior of TaNbHfZrTi alloy: A first principles simulation study, in: TMS 2013 Annual Meeting, San Antonio, Texas, 2013.

[5] M.H.H. Shizhong Yang, Li Wang, Shengmin Guo, Zhi Tang, Peter Liaw, Liuxi Tan, Cheng Guo, Michael Jackson, The hot corrosion resistance properties of AlxFeCoCrNi, in: TMS Annual Meeting & Exhibition, San Diego Convention Center, 2014.

[6] O.N. Starovoytov, M. Gao, S. Guo, E. Khosravi, J. Lei, L. Tan, S. Yang, Comparative studies of the ground state properties for $Nb_{25}Mo_{25}Ta_{25}W_{25}$ and $V_{20}Nb_{20}Mo_{20}Ta_{20}W_{20}$, in: TMS2013 Supplemental Proceedings, John Wiley & Sons, Inc., 2013, pp. 1137-1145.

[7] K.Y. Tsai, M.H. Tsai, J.W. Yeh, Sluggish diffusion in Co–Cr–Fe–Mn–Ni high-entropy alloys, Acta Materialia, 61 (2013) 4887-4897.

[8] B. Cantor, I.T.H. Chang, P. Knight, A.J.B. Vincent, Microstructural development in equiatomic multicomponent alloys, Mat. Sci. Eng. A, 375–377 (2004) 213-218.

[9] J.W. Yeh, S.K. Chen, S.J. Lin, J.Y. Gan, T.S. Chin, T.T. Shun, C.H. Tsau, S.Y. Chang, Nanostructured High-Entropy Alloys with Multiple Principal Elements: Novel Alloy Design Concepts and Outcomes, Adv. Eng. Mat., 6 (2004) 299-303.

[10] M.C. Gao, D.E. Alman, Searching for Next Single-Phase High-Entropy Alloy Compositions, Entropy, 15 (2013) 4504-4519.

[11] B. Zhang, M.C. Gao, Y. Zhang, S. Yang, S.M. Guo, Senary Refractory High-Entropy Alloy MoNbTaTiVW, Mat. Sci. Tech., in press (2015).

[12] D.B. Miracle, J.D. Miller, O.N. Senkov, C. Woodward, M.D. Uchic, J. Tiley, Exploration and Development of High Entropy Alloys for Structural Applications, Entropy, 16 (2014) 494-525.

[13] G.B. Olson, C.J. Kuehmann, Materials genomics: From CALPHAD to flight, Scripta Materialia, 70 (2014) 25-30.

[14] J. Montgomery, G. Olson, G. Olson, M. Azrin, E. Wright, Innovations in ultrahigh strength steel technology, in: Proc. 34th Sagamore Army Materials Research Conf., GB Olson, M. Azrin, and ES Wright, eds., US Army Materials Technology Laboratory, Watertown, MA, 1990, pp. 147-178.

[15] G.B. Olson, Computational design of hierarchically structured materials, Science, 277 (1997) 1237-1242.

[16] G.B. Olson, Designing a new material world, Science, 288 (2000) 993-998.

[17] C.J. Kuehmann, G.B. Olson, H.-J. Jou, Nanocarbide precipitation strengthened ultrahigh-strength, corrosion resistant, structural steels, (2011).

[18] C. J. Kuehmann and G. B. Olson, Databases, and simulation tools needed for the realization of integrated computational materials engineering, ASM, (2010).

[19] N. Saunders, A.P. Miodownik, Calphad (calculation of phase diagrams): A comprehensive guide: A comprehensive guide, in, Elsevier, 1998.

[20] H. Okamoto, Desk Handbook: Phase Diagrams for Binary Alloys, ASM International, Materials Park, OH 44073, 2000.

[21] O.N. Senkov, J.M. Scott, S.V. Senkova, D.B. Miracle, C.F. Woodward, Microstructure and room temperature properties of a high-entropy TaNbHfZrTi alloy, J. Alloys Comp., 509 (2011) 6043-6048.

[22] O.N. Senkov, G.B. Wilks, D.B. Miracle, C.P. Chuang, P.K. Liaw, Refractory high-entropy alloys, Intermetallics, 18 (2010) 1758-1765.

[23] G.H. Gulliver, The quantitative effect of rapid cooling upon the constitution of binary alloys, Journal of the Institute of Metals, 9 (1913) 120-157.

[24] M. Pourbaix, Atlas of electrochemical equilibria in aqueous solutions, (1974).

[25] M. Pourbaix, Lectures on electrochemical corrosion, Springer Science & Business Media, 2012.

[26] E. McCafferty, Introduction to corrosion science, Springer Science & Business Media, 2010.

[27] W. Sargent, Table of periodic properties of the elements, in: Sargent-Welch Scientific, Skokie, IL, 1980.

[28] W. Benenson, H. Stöcker, Handbook of physics, in, Springer, 2002.

[29] B. Cullity Deceased, S. Stock, Elements of X-ray Diffraction, in, New Jersey: Prentice Hall, 2001.

[30] WebElements, the periodic table on the web. Available online: http://www.webelements.com/.

[31] E. Schafler, G. Steiner, E. Korznikova, M. Kerber, M.J. Zehetbauer, Lattice defect investigation of ECAP-Cu by means of X-ray line profile analysis, calorimetry and electrical resistometry, Materials Science and Engineering: A, 410–411 (2005) 169-173.

[32] A. Leo, C. Hansch, D. Elkins, Partition coefficients and their uses, Chemical reviews, 71 (1971) 525-616.

[33] Y. Zhang, Y.J. Zhou, J.P. Lin, G.L. Chen, P.K. Liaw, Solid-solution phase formation rules for multi-component alloys, Advanced Engineering Materials, 10 (2008) 534-538.

[34] W.D. Klopp, A review of chromium, molybdenum, and tungsten alloys, Journal of the Less Common Metals, 42 (1975) 261-278.

[35] P.K. Huang, J.W. Yeh, T.T. Shun, S.K. Chen, Multi‐Principal‐Element Alloys with Improved Oxidation and Wear Resistance for Thermal Spray Coating, Advanced Engineering Materials, 6 (2004) 74-78.

[36] C.-Y. Hsu, J.-W. Yeh, S.-K. Chen, T.-T. Shun, Wear resistance and high-temperature compression strength of Fcc CuCoNiCrAl0. 5Fe alloy with boron addition, Metallurgical and Materials Transactions A, 35 (2004) 1465-1469.

[37] Y.J. Zhou, Y. Zhang, Y.L. Wang, G.L. Chen, Solid solution alloys of AlCoCrFeNiTi x with excellent room-temperature mechanical properties, Applied physics letters, 90 (2007) 181904-181904.

[38] O.N. Senkov, J.M. Scott, S.V. Senkova, F. Meisenkothen, D.B. Miracle, C.F. Woodward, Microstructure and elevated temperature properties of a refractory TaNbHfZrTi alloy, Journal of Materials Science, 47 (2012) 4062-4074.

[39] O.N. Senkov, J.M. Scott, S.V. Senkova, D.B. Miracle, C.F. Woodward, Microstructure and room temperature properties of a high-entropy TaNbHfZrTi alloy, Journal of Alloys and Compounds, 509 (2011) 6043-6048.

[40] B. Zhang, M. Gao, Y. Zhang, S. Yang, S. Guo, Senary refractory high entropy alloy MoNbTaTiVW, Materials Science and Technology, 31 (2015) 1207-1213.

[41] M.C. Gao, B. Zhang, S. Yang, S.M. Guo, Senary Refractory High-Entropy Alloy HfNbTaTiVZr, Metallurgical and Materials Transactions A, (2015) 1-13.

[42] C.-C. Juan, M.-H. Tsai, C.-W. Tsai, C.-M. Lin, W.-R. Wang, C.-C. Yang, S.-K. Chen, S.-J. Lin, J.-W. Yeh, Enhanced mechanical properties of HfMoTaTiZr and HfMoNbTaTiZr refractory high-entropy alloys, Intermetallics, 62 (2015) 76-83.

[43] M.C. Gao, Ö.N. Doğan, P. King, A.D. Rollett, M. Widom, The first-principles design of ductile refractory alloys, JOM, 60 (2008) 61-65.

[44] B. Zhang, M. C. Gao, Y. Zhang, S.M. Guo, Supporting Data for Senary Refractory High-Entropy Alloy CrxMoNbTaVW, Data in Brief, submitted.

[45] E. Scheil, Z. Metallkd, 34 (1942) 70-72.

[46] L.A. Girifalco, Statistical mechanics of solids, OUP USA, 2003.

[47] T. Si, V. Ti, Z. W Y, TCNI7-TCS Ni-based Superalloys Database, Version 7.1.

[48] W. Benenson, H. Stöcker, Handbook of physics, Springer Science & Business Media, 2002.

[49] W.C. Winegard, An introduction to the solidification of metals, Institute of Metals, 1964.

[50] W.B. Pearson, Crystal chemistry and physics of metals and alloys, (1972).

[51] M. Widom, Chapter 8: Prediction of structure and phase transformations, in: M.C. Gao, J.W. Yeh, P.K. Liaw, Y. Zhang (Eds.) High-Entropy Alloys: Fundamentals and Applications, Springer, Cham, 2015.

[52] Y. Zhang, S. Guo, C.T. Liu, X. Yang, Chapter 2: Phase Formation Rules, in: M.C. Gao, J.W. Yeh, P.K. Liaw, Y. Zhang (Eds.) High-Entropy Alloys: Fundamentals and Applications, Springer, Cham, Switzerland, 2015.

[53] J.W. Yeh, S.K. Chen, S.J. Lin, J.Y. Gan, T.S. Chin, T.T. Shun, C.H. Tsau, S.Y. Chang, Nanostructured high‐entropy alloys with multiple principal elements: novel alloy design concepts and outcomes, Advanced Engineering Materials, 6 (2004) 299-303.

[54] G. Sheng, C.T. LIU, Phase stability in high entropy alloys: formation of solid-solution phase or amorphous phase, Progress in Natural Science: Materials International, 21 (2011) 433-446.

[55] G. Anand, R. Goodall, C.L. Freeman, Role of configurational entropy in body-centred cubic or face-centred cubic phase formation in high entropy alloys, Scripta Materialia, 124 (2016) 90-94.

[56] M. Lucas, G. Wilks, L. Mauger, J.A. Munoz, O. Senkov, E. Michel, J. Horwath, S. Semiatin, M.B. Stone, D.L. Abernathy, Absence of long-range chemical ordering in equimolar FeCoCrNi, Applied Physics Letters, 100 (2012) 251907.

[57] B. Cantor, I. Chang, P. Knight, A. Vincent, Microstructural development in equiatomic multicomponent alloys, Materials Science and Engineering: A, 375 (2004) 213-218.

[58] O. Senkov, G. Wilks, J. Scott, D. Miracle, Mechanical properties of Nb 25 Mo 25 Ta 25 W 25 and V 20 Nb 20 Mo 20 Ta 20 W 20 refractory high entropy alloys, Intermetallics, 19 (2011) 698-706.

[59] O. Senkov, J. Scott, S. Senkova, D. Miracle, C. Woodward, Microstructure and room temperature properties of a high-entropy TaNbHfZrTi alloy, Journal of alloys and compounds, 509 (2011) 6043-6048.

[60] R. Kozak, A. Sologubenko, W. Steurer, Single-phase high-entropy alloys–an overview, Zeitschrift für Kristallographie-Crystalline Materials, 230 (2015) 55-68.

[61] U. Dahlborg, J. Cornide, M. Calvo-Dahlborg, T.C. Hansen, A. Fitch, Z. Leong, S. Chambreland, R. Goodall, Structure of some CoCrFeNi and CoCrFeNiPd multicomponent HEA alloys by diffraction techniques, Journal of Alloys and Compounds, 681 (2016) 330-341.

[62] F. Otto, A. Dlouhý, K.G. Pradeep, M. Kuběnová, D. Raabe, G. Eggeler, E.P. George, Decomposition of the single-phase high-entropy alloy CrMnFeCoNi after prolonged anneals at intermediate temperatures, Acta Materialia, 112 (2016) 40-52.

[63] M.G. Poletti, S. Branz, G. Fiore, B.A. Szost, W.A. Crichton, L. Battezzati, Equilibrium high entropy phases in X-NbTaTiZr (X = Al,V,Cr and Sn) multiprincipal component alloys, Journal of Alloys and Compounds, 655 (2016) 138-146.

[64] C.-M. Lin, H.-L. Tsai, Equilibrium phase of high-entropy FeCoNiCrCu0.5 alloy at elevated temperature, Journal of Alloys and Compounds, 489 (2010) 30-35.

[65] E.J. Pickering, R. Muñoz-Moreno, H.J. Stone, N.G. Jones, Precipitation in the equiatomic high-entropy alloy CrMnFeCoNi, Scripta Materialia, 113 (2016) 106-109.

[66] F. He, Z. Wang, Q. Wu, J. Li, J. Wang, C.T. Liu, Phase separation of metastable CoCrFeNi high entropy alloy at intermediate temperatures, Scripta Materialia, 126 (2017) 15-19.

[67] N. Saunders, A.P. Miodownik, CALPHAD (calculation of phase diagrams): a comprehensive guide, Elsevier, 1998.

[68] B. Zhang, M. Gao, Y. Zhang, S. Yang, S. Guo, Senary refractory high entropy alloy MoNbTaTiVW, Materials Science and Technology, (2015) 1743284715Y. 0000000031.

[69] M. Gao, B. Zhang, S. Yang, S. Guo, Senary Refractory High-Entropy Alloy HfNbTaTiVZr, Metallurgical and Materials Transactions A, (2015) 1-13.

[70] Y. Zhang, Z. Wang, B. Zhang, C. Zhou, G.-L. Zhao, J. Jiang, S. Guo, Morphology and electromagnetic interference shielding effects of SiC coated carbon short fibers, Journal of Materials Chemistry C, 3 (2015) 9684-9694.

[71] G. Gulliver, The quantitative effect of rapid cooling upon the constitution of binary alloys, J INST MET, 13 (1915) 263-291.

[72] B. Zhang, M. Gao, Y. Zhang, S. Guo, Senary refractory high-entropy alloy CrxMoNbTaVW, Calphad, 51 (2015) 193-201.

[73] B. Zhang, Y. Mu, M. Gao, W. Meng, S. Guo, On single-phase status and segregation of an as-solidified septenary refractory high entropy alloy, MRS Communications, 7 (2017) 78-83.

[74] A.V. Plyasunov, E.L. Shock, Correlation strategy for determining the parameters of the revised Helgeson-Kirkham-Flowers model for aqueous nonelectrolytes, Geochimica et Cosmochimica Acta, 65 (2001) 3879-3900.

[75] X. Zhang, Galvanic corrosion, Uhlig's Corrosion Handbook, 51 (2011) 123.

[76] P.R. Roberge, Corrosion engineering: principles and practice, McGraw-Hill New York, 2008.

[77] D.E. Talbot, J.D. Talbot, Corrosion science and technology, CRC Press, 2007.

[78] T.-T. Shun, L.-Y. Chang, M.-H. Shiu, Microstructure and mechanical properties of multiprincipal component CoCrFeNiMox alloys, Materials Characterization, 70 (2012) 63-67.

[79] W.-R. Wang, W.-L. Wang, S.-C. Wang, Y.-C. Tsai, C.-H. Lai, J.-W. Yeh, Effects of Al addition on the microstructure and mechanical property of Al x CoCrFeNi high-entropy alloys, Intermetallics, 26 (2012) 44-51.

[80] H.-P. Chou, Y.-S. Chang, S.-K. Chen, J.-W. Yeh, Microstructure, thermophysical and electrical properties in Al x CoCrFeNi ($0 \leqslant x \leqslant 2$) high-entropy alloys, Materials Science and Engineering: B, 163 (2009) 184-189.

[81] A.K. Singh, A. Subramaniam, On the formation of disordered solid solutions in multi-component alloys, Journal of Alloys and Compounds, 587 (2014) 113-119.

[82] Z. Wu, H. Bei, F. Otto, G.M. Pharr, E.P. George, Recovery, recrystallization, grain growth and phase stability of a family of FCC-structured multi-component equiatomic solid solution alloys, Intermetallics, 46 (2014) 131-140.

[83] Y.-F. Kao, T.-J. Chen, S.-K. Chen, J.-W. Yeh, Microstructure and mechanical property of as-cast,-homogenized, and-deformed Al x CoCrFeNi ($0 \leqslant x \leqslant 2$) high-entropy alloys, Journal of Alloys and Compounds, 488 (2009) 57-64.

[84] Y.-F. Kao, S.-K. Chen, T.-J. Chen, P.-C. Chu, J.-W. Yeh, S.-J. Lin, Electrical, magnetic, and Hall properties of Al x CoCrFeNi high-entropy alloys, Journal of alloys and compounds, 509 (2011) 1607-1614.

[85] Y.-J. Hsu, W.-C. Chiang, J.-K. Wu, Corrosion behavior of FeCoNiCrCux high-entropy alloys in 3.5% sodium chloride solution, Materials Chemistry and Physics, 92 (2005) 112-117.

[86] Y. Shi, B. Yang, X. Xie, J. Brechtl, K.A. Dahmen, P.K. Liaw, Corrosion of Al xCoCrFeNi high-entropy alloys: Al-content and potential scan-rate dependent pitting behavior, Corrosion Science, 119 (2017) 33-45.

[87] C.-M. Lin, H.-L. Tsai, Evolution of microstructure, hardness, and corrosion properties of high-entropy Al 0.5 CoCrFeNi alloy, Intermetallics, 19 (2011) 288-294.

[88] R. Castelli, Nuclear corrosion modeling: the nature of crud, Butterworth-Heinemann, 2009.

[89] B.D. Craig, Fundamental aspects of corrosion films in corrosion science, Springer Science & Business Media, 2013.

[90] A. Rahman, V. Chawla, R. Jayaganthan, R. Chandra, R. Ambardar, Hot corrosion of nanostructured Cr/Co–Al coatings, Surface Engineering, 28 (2012) 285-293.

[91] L. Ratke, S. Diefenbach, Liquid immiscible alloys, Materials Science and Engineering: R: Reports, 15 (1995) 263-347.

[92] P. Wu, N. Liu, P. Zhou, Z. Peng, W. Du, X. Wang, Y. Pan, Microstructures and liquid phase separation in multicomponent CoCrCuFeNi high entropy alloys, Materials Science and Technology, 32 (2016) 576-580.

[93] Y. Jien-Wei, Recent progress in high entropy alloys, Ann. Chim. Sci. Mat, 31 (2006) 633-648.

[94] G. Ervin, Structural interpretation of the diaspore–corundum and boehmite–γ-Al2O3 transitions, Acta Crystallographica, 5 (1952) 103-108.

[95] R. Alwitt, J. Diggle, Oxides and oxide films, Marcel Dekker, NY, (1976).

[96] G. Davis, W. Moshier, G. Long, D. Black, Passive Film Structure of Supersaturated Al‐Mo Alloys, Journal of the Electrochemical Society, 138 (1991) 3194-3199.

[97] R.M.R. Junqueira, C.R.d.O. Loureiro, M.S. Andrade, V.T.L. Buono, Characterization of interference thin films grown on stainless steel surface by alternate pulse current in a sulphochromic solution, Materials Research, 11 (2008) 421-426.

[98] S. Fujimoto, Thick Porous Oxide Layer on Fe-Cr and Ni-Cr Alloys Formed by Square Wave Potential Pulse Polarization, in: Pits and Pores III: Formation, Properties, and Significance for Advanced Materials: Proceedings of the International Symposium, The Electrochemical Society, 2006, pp. 180.

[99] D.A. Shifler, D.M. Aylor, Factors Affecting Corrosion Performance and Testing of Materials and Components in Sea Water, in: CORROSION 2005, NACE International, 2005.

VITA

Boliang Zhang born in Xi'an, China. He finished his undergraduate study in Xi'an Jiaotong University in June 2011, majored in Energy power system and automation. After that, he started his graduate study in USA. He spent the first one and half year in Mechanical and aerospace engineering department of University of Florida, mainly focused on the heat and mess transfer. In Jan. 2013, driven by his interest in advance manufacturing and materials, he transferred to Dr. Shengmin Guo's group in Mechanical and Industrial Engineering department of Louisiana State University, and finished his master degree remotely in later that same year. Since then, he has been working as a Research Assistant in Dr. Guo's lab. He expects to receive his Ph. D the Spring 2018 with degree only registration since Jan. 2018.